5-2014

# Adaptive and Robust Braking-Traction Control Systems

John Adcox
*Clemson University*, jadcox@g.clemson.edu

## Recommended Citation

Adcox, John, "Adaptive and Robust Braking-Traction Control Systems" (2014). *All Dissertations*. 1371.
https://tigerprints.clemson.edu/all_dissertations/1371

# ADAPTIVE AND ROBUST BRAKING-TRACTION CONTROL SYSTEMS

A Dissertation
Presented to
the Graduate School of
Clemson University

In Partial Fulfillment
of the Requirements for the Degree
Doctor of Philosophy
in Automotive Engineering

by
John Adcox
May 2014

Accepted by:
Dr. Beshah Ayalew, Committee Chair
Dr. Imtiaz Haque
Dr. Timothy Rhyne
Dr. Ardalan Vahidi

# ABSTRACT

The designs of commercial Anti-Lock Braking Systems often rely on assumptions of a torsionally rigid tire-wheel system and heavily rely on hub-mounted wheel speed sensors to manage tire-road slip conditions. However, advancements in high-bandwidth braking systems, in-wheel motors, variations in tire/wheel designs, and loss of inflation pressure, have produced scenarios where the tire's torsional dynamics could be easily excited by the braking system actuator. In these scenarios, the slip conditions for the tire-belt/ring will be dynamically different from what can be inferred from the wheel speed sensors.

This dissertation investigates the interaction of tire torsional dynamics with ABS & traction controllers and offers new control designs that incorporate schemes for identifying and accommodating these dynamics. To this end, suitable braking system and tire torsional dynamics simulation models as well as experimental test rigs were developed. It is found that, indeed, rigid-wheel based controllers give degraded performance when coupled with low torsional stiffness tires.

A closed-loop observer/nonlinear controller structure is proposed that adapts to unknown tire sidewall and tread parameters during braking events. It also provides estimates of difficult to measure state variables such as belt/ring speed. The controller includes a novel virtual damper emulation that can be used to tune the system response. An adaptive sliding-mode controller is also introduced that combines robust stability characteristics with tire/tread parameter and state estimation. The sliding mode controller is shown to be very effective at tracking its estimated target, at the expense of reducing the tire parameter adaptation performance. Finally, a modular robust state observer is developed that allows for robust estimation of the system states in the presence of uncertainties and external disturbances without the need for sidewall parameter adaptation.

# DEDICATION

I would like to dedicate this dissertation to my brilliant and beautiful wife who encouraged and supported me to the fullest through my graduate studies; even when it required spending countless late nights and weekends sitting with me in the lab. Without her I would not be half the person that I am today.

# ACKNOWLEDGEMENTS

First of all, I would like to acknowledge my advisor Dr. Beshah Ayalew for his guidance and support throughout my research. His technical knowledge and expertise has provided me with the tools that I needed to complete my research. He went above and beyond on several occasions in order to provide me with the tools that I needed in order to complete my research. In one such circumstance he went as far so to teach an elective graduate-level controls course for the primary purpose of developing his student's skill sets; and for this I am extremely thankful.

I am grateful to my committee members, Dr. Imtiaz Haque, Dr. Timothy Rhyne, and Dr. Ardalan Vahidi for their review and input on my research. Their classes were also very valuable and beneficial and were greatly appreciated.

Many thanks are required for Dr. John Ziegert, whose guidance in my first few years at ICAR were instrumental. Dr. Ziegert encouraged me to switch to the PhD program and gave me the motivation that I needed to take that first step; and for that I am very grateful. His immense care and consideration for his students' professional development is unmatched. He is admired by all of his students and is held in the upmost esteem.

I would also like to thank my family and friends for all the support that they have given to me throughout this journey. They were there for me during throughout the most stressful times and provided me with the encouragement that was needed to keep moving forward.

Special thanks are required for my peers: Shayne McConomy, Evan Lowe, Parikshit Mehta, Tamer Yanni, Justin Sill, and Jeffery Anderson who spent hours discussing and supporting me with my research through intellectual discussions and experimental support; without them my experience would not have been the same.

I would also like to thank both BMW and Michelin for providing me with the opportunity to work on several intellectually challenging projects. Their projects gave me the opportunity to grow and gain valuable experience.

And last but not least, I would like to thank everyone within the Clemson University Automotive Engineering Department. Their support throughout my time here has been invaluable and is greatly appreciated. Special acknowledgement is required for Gary Mathis and David Mann as they were instrumentally helpful in bringing my experimental tests to fruition. Both David and Gary always displayed an incredible willingness to support and help me through my entire time here at Clemson University – International Center of Automotive Research and their actions will always be appreciated and never forgotten.

# TABLE OF CONTENTS

# TABLE OF CONTENTS (Continued)

Page

# TABLE OF CONTENTS (Continued)

Page

# LIST OF FIGURES

Page

# LIST OF FIGURES (Continued)

# LIST OF FIGURES (Continued)

Page

# LIST OF FIGURES (Continued)

Page

# LIST OF FIGURES (Continued)

Page

# LIST OF FIGURES (Continued)

# LIST OF FIGURES (Continued)

Page

# LIST OF TABLES

# CHAPTER 1: INTRODUCTION

## 1.1 RESEARCH MOTIVATION & OBJECTIVES

The primary objective of this dissertation is to investigate the interaction of tire torsional dynamics with braking/traction controllers and outline robust and adaptive control schemes that identify and/or accommodate these dynamics in the overall control schemes.

In the automotive industry, legislation and competition continue to push for technical solutions that ensure that the subsystems of the vehicle work seamlessly together to maximize safety potential and customer expected performance. In this regard, there has been a significant effort in the past several decades to incorporate various active safety systems (ASS) and advanced driveline control systems that often utilize and integrate various objectives. The technical solutions offered often involve control systems that operate under some assumptions about the dominant system or subsystem dynamics deemed to significantly influence the objective under consideration.

Perhaps the most widely implemented of the active safety systems are Anti-lock Braking Systems (ABS) and Traction Control Systems (TCS) that manage slip conditions at the tire-road interface. However, the traditional design of ABS and TCS algorithms, as well as most of the active driveline control systems, are based on simplified rigid wheel assumptions of the tire, and primarily focus on maximizing transmittable braking/tractive forces on various tire/ground friction surfaces. While this may have been an adequate assumption for many applications, concurrent advancements in high-bandwidth Electromechanical Brake (EMB) systems [1-4], in-wheel motors [5], and tire/wheel technology (through development of lower torsional stiffness tires) have produced scenarios where some actuators have the ability to excite the tire's torsional modes. It has also been shown that there are drastic differences in a tire's torsional dynamic properties when it becomes deflated [6-8]. In all the above scenarios, there is a definite distinction between the behavior of the wheel/hub and tread-belt because of the torsional dynamics of the tire. Since most, if not all, ABS/TCS systems use wheel/hub speed sensors as the sole means of feedback (based on the rigid wheel assumption), one can expect sub-optimal performance of such controllers when used with torsionally flexible tires.

There have been several authors [5-8] who observed this issue and have subsequently modeled and simulated commercial ABS control structures that are combined with these various flexible tire models to see their effect on braking performance. These works all recognize an interaction between the ABS controller and the tire's torsional dynamics. However, to the author's knowledge there is no published work directed towards development of controllers that account for these dynamics.

In recent years, there has also been an increased interest in adaptive traction control systems that use dynamic friction models to estimate the flexible tread parameters and subsequently calculate a desired slip ratio [10-13]. One of the original papers to take this approach [10] utilized a dynamic tread-ground friction model, but assumed that all the tread parameters were known except for the friction curve magnitude. This work was further expanded in [12] to estimate the states and tread parameters and tracked an estimated slip ratio target. Even though in the past few years there has been an increase in the amount of research on traction/ABS controllers and dynamic friction models, there still appears to be no investigation that incorporates the tire's torsional dynamics into the controller design.

Initial investigation into the interactions of tire/wheel designs with the workings of a typical commercial ABS control system has also shown that a decrease in the tire torsional stiffness can have a drastic impact on the vehicle's stopping distance. In light of these results, the objective of this work is to evaluate commercial-based controllers for various torsional tire stiffnesses and subsequently develop a set of adaptation schemes, robust state observers, and controllers to account for the uncertainties associated with the tire's sidewall and tread-ground contact friction dynamics.

## 1.1 RESEARCH CONTRIBUTIONS

This dissertation's main objective is to study the interaction of tire torsional dynamics with currently available ABS and traction controllers and develop a set of new adaptive and robust controllers, observers, and parametric estimators that account for these dynamics. The framework for this objective will first be completed through the development of a comprehensive vehicle and tire model, and evaluation of rigid-wheel based controllers on a torsionally flexible tire. Following this a set of novel closed-loop traction systems will be developed.

The main contributions of this dissertation are as follows:

1. The development of a nonlinear controller that incorporates both the torsional sidewall dynamics and tread-ground contact friction dynamics
2. Development and implementation of a sliding-mode controller to account for the tire's dominant dynamics and tread-ground contact friction dynamics
3. Development of an adaptation scheme to allow for convergence of the system parameters and states to their true values
4. The development of a novel virtual damper that can be incorporated into the controller to produce a system response that acts similar to a well-damped system
5. A robust observer that allows for robust tracking of the system states in the presence of uncertainties and external disturbances

## 1.2 DISSERTATION ORGANIZATION

The remainder of the dissertation is organized as follows. First, in Chapter 2, a detailed literature review of various tire models, friction models, and controllers will be discussed.

In Chapter 3, the system modeling will be presented as well as discussions of an experimental test fixture that was designed and built for use on a chassis dynamometer. In addition to the customary hydraulic braking system, an electromechanical-brake (EMB) system is discussed that was designed and built in order to obtain an actuator with sufficient bandwidth for this research.

Chapter 4 will present the modeling and evaluation of the commercial-based ABS controller in both simulations and experiments.

In Chapter 5 a nonlinear controller with parameter adaptation is proposed, followed by an adaptive sliding mode controller in Chapter 6. Both of these controllers are designed to not only adapt to the tire sidewall parameters but also the longitudinal tread parameters, thus allowing for an adaptive search method for the desired target slip ratio.

Chapter 7 presents a robust observer that can be used in conjunction with both the nonlinear and sliding-mode controllers. And lastly, Chapter 8 summarizes the conclusions, reviews the contributions made in the dissertation, and discusses areas for future work.

# CHAPTER 2: BACKGROUND MATERIAL

In this chapter, a review of the existing work is presented to give a background to the research discussed in the subsequent chapters. The basic widely accepted rigid-ring tire model is introduced in Section 2.1. In Section 2.2, a group of steady-state and dynamic contact friction models are discussed. In Section 2.3, a set of traction and ABS controllers will be evaluated based on their merits and shortcomings.

## 2.1 RIGID-RING TIRE MODEL

The rigid-ring tire model consists of two rigid bodies, the wheel hub and the tread-band (known as the ring), connected by a set of springs and dampers that allow relative motion between them in the longitudinal, vertical, and torsional directions, as shown in Figure 1. An extension of the rigid-ring tire model is known as the flexible-ring tire model and includes flexibility of the ring. However, it has been shown that the vibrational modes that are associated with the flexible ring occur at much higher frequencies than the tire's rigid body modes [9]. As we are not interested in the high-frequency tire dynamics, it has been assumed that it can be modeled as a rigid ring. Also, for the purposes of analyzing the effect the tire's dynamics have on traction and ABS controllers, the effects of vertical weight transfer can often be ignored on slip-tracking controllers since the desired slip ratio is not a function of the normal force, as will be shown later. Thus, this model can further be simplified by ignoring the tire's vertical stiffness.

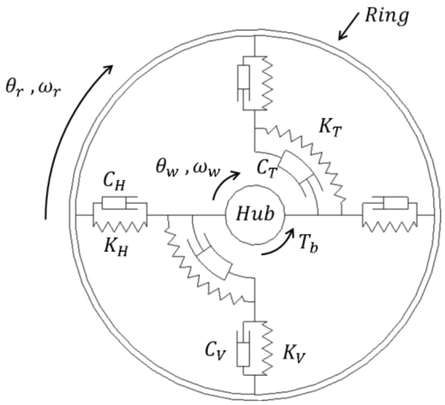

**FIGURE 1: RIGID-RING TIRE MODEL**

Under semi-constant acceleration/deceleration, such as a traction or braking event, it has been shown through multiple sources [9, 10] that the torsional dynamics of the tire dominate over the horizontal deflections. This observation has been confirmed through simulations. Figure 2 shows the relative displacement of the ring and hub in both the longitudinal and equivalent torsional directions. This figure highlights how the torsional deflections are significantly greater than those in the longitudinal direction. Figure 3, which shows the relative velocity between the two bodies, demonstrates this discrepancy even further by showing that the relative longitudinal velocity almost immediately goes to zero after the initial impulse at 1 second. Taking this knowledge into consideration, the longitudinal deflections of the rigid-ring model can also be ignored, leaving just the torsional dynamics of the tire. This final simplified rigid-ring model will be utilized throughout this dissertation, and is shown in Figure 4.

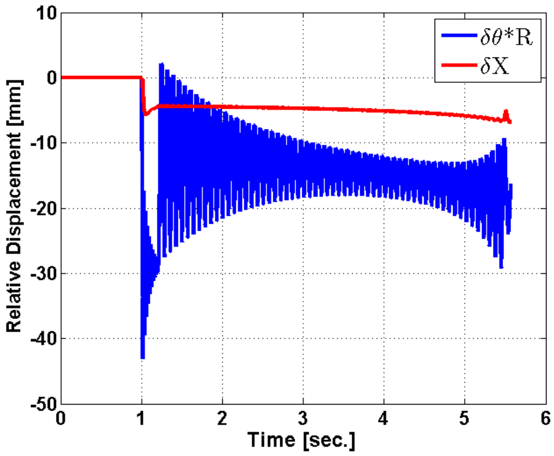

**FIGURE 2: RELATIVE LONGITUDINAL & TORSIONAL DISPLACEMENT**

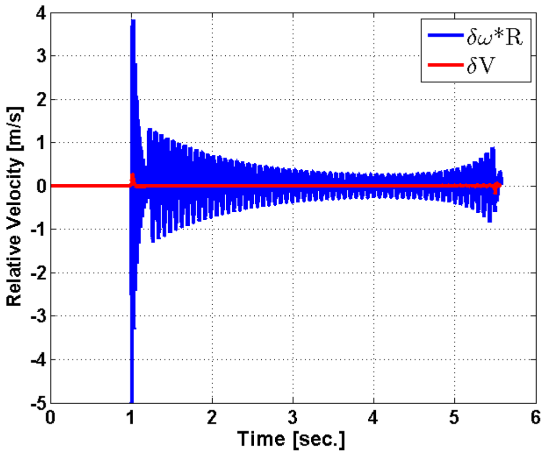

**FIGURE 3: RELATIVE LONGITUDINAL & TORSIONAL VELOCITY**

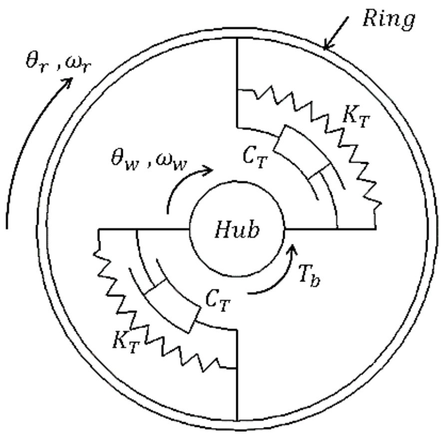

**FIGURE 4: SIMPLIFIED RIGID-RING MODEL**

## 2.2 FRICTION MODELS

### 2.2.1 STATIC FRICTION MODEL

The Magic Formula tire model was developed by Pacejka and co-workers in the mid-80's [11-13] and has become a standard for modeling tire friction curves since then.

The Magic Formula was developed by identifying a mathematical equation of the steady state tire/surface friction curve. The basic form of this model is as follows:

$$F_x = D * \sin\Big[C * arctan\Big\{B(\kappa + S_H) + E\Big(arctan\big(B(\kappa + S_H)\big) - B(\kappa + S_H)\Big)\Big\}\Big] + S_V \tag{(1)}$$

where, $F_x$ is the longitudinal tire force, the coefficients B,C, D, and E characterize the shape of the slip curve, $S_H$ and $S_v$ are the horizontal and vertical shifts of the slip curve, respectively, and $\kappa$ is the longitudinal slip ratio. For more detailed descriptions of each variable the reader is referred to [9]. While the Magic Formula provides a representation of the steady state friction characteristics, this model can produce numerical difficulties when the vehicle velocity is low and is very nonlinear for small changes in parameters.

Other static models that have been proposed include Burckhardt's model [14], which includes a dependency on velocity, a revised three-parameter Burckhardt's model [15], and a model introduced by Kiencke and Daiss [16]. These static friction models are generally used in full-vehicle analysis where only the tire's quasi-steady state response is considered relevant. However, if the dynamics of the tire are of interest or low-velocity numerical difficulties produce a challenge, then the static friction models are no longer a valid option.

### 2.2.2 DYNAMIC FRICTION MODELS

If the dynamics of a tire are of interest then a dynamic friction model should be used. Generally, the dynamic friction models can be cast into the same structure as the traditional brush model. One attempt to capture these dynamics has been to modify the magic formula model to include the relaxation length of the tire. This is done by introducing a single parameter brush model to represent the stiffness of the tread [17]. The structure of this model structure is shown in the following figure (Figure 5).

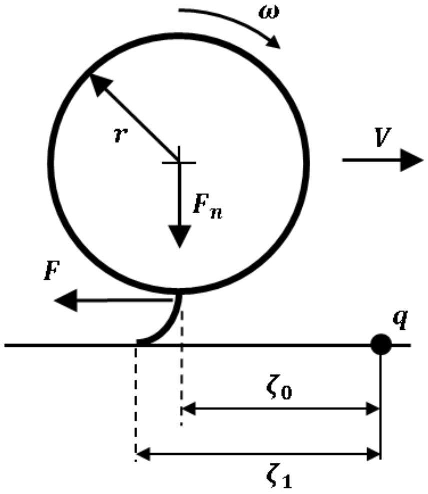

**FIGURE 5: SINGLE PARAMETER BRUSH MODEL**

Here, $\zeta_0$ is the distance from an undeformed point on the wheel to a reference forward point q. $\zeta_1$ represents the distance from the deformed tread bristle on the road to the forward point q. Note that both q and the undeformed point on the wheel move at the same velocity as the vehicle, thus the distance $\zeta_0$ is constant and is known as the longitudinal relaxation length. It is the distance traveled for the tire to reach 63% of the steady-state condition after a step input in brake/traction torque. The *normalized* relative displacement can then be defined through the following equation:

$$z = \frac{\zeta_1 - \zeta_0}{\zeta_0} \tag{2}$$

Differentiating this equation with respect to time results in:

$$\zeta_0 * \frac{dz}{dt} = v_r * sgn(v) - |v|z \tag{3}$$

where,

$$\dot{\zeta}_0 = |v|$$

$$\dot{\zeta}_1 = sgn(v) * r\omega$$

$$v_r = r\omega - v$$

The friction force then becomes a function of the longitudinal slip z, $F = h(z)$, which is commonly defined as $F = kz$, where $k$ represents a linear interpretation of the tire's tread stiffness [18]. However, this represents a linear increase in friction force with an increase in the relative displacement with no maximum friction coefficient, and thus does not truly represent the actual friction dynamics.

A more complete model of dynamic friction can be represented using a lumped or distributed brush-type model that is not dependent on the static friction curves. A lumped friction model assumes a single contact point with the ground, such as the relaxation-length model described above. This results in a set of ordinary differential equations in time. However, a distributed friction model represents a full contact patch and as such has a set of contact points with the ground. This model results in a set of partial differential equations in time and space.

The Dahl model is a lumped friction model developed in the mid 70's and models the friction force like a stress-strain curve which gradually increases in force until slippage between the deformed contact point and the ground begins to occur.

$$\frac{dF}{dx} = \sigma_0 \left( 1 - \frac{F}{F_c} sgn(v_r) \right) \tag{4}$$

Redefining $F = z\sigma_0$ and utilizing the chain rule, Equation (4) can be rewritten as

$$\frac{dz}{dt} = v_r - \frac{\sigma_0 |v_r|}{F_c} z \tag{5}$$

where, $z$ is now defined as the *actual* relative bristle deflection and $\sigma_0$ represents a bristle stiffness coefficient.

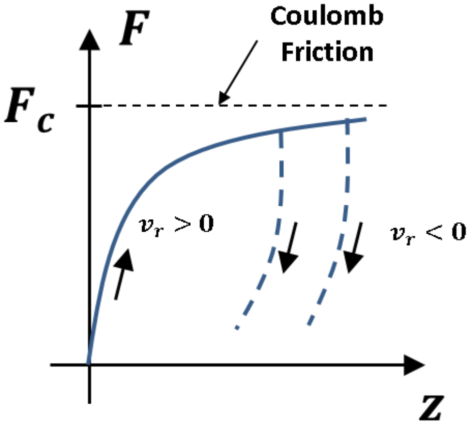

FIGURE 6: DAHL MODEL

One of the main improvements that is made with the Dahl model is its incorporation of a maximum friction coefficient $F_c$ and the relative velocity-based hysteretic loops, as shown in Figure 6. While the Dahl model captures many properties of the friction dynamics, it doesn't incorporate the Stribeck effect shown in Figure 7 [19].

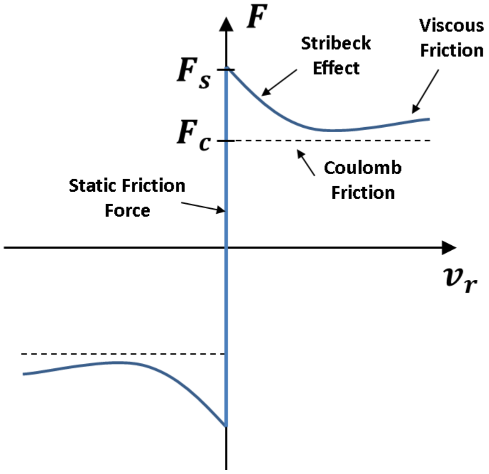

FIGURE 7: STATIC FRICTION CURVE

The Lumped LuGre friction model is an extension of the Dahl model that includes the Stribeck effect by replacing the static Coulomb friction force $F_c$ with a relative velocity dependent function $g(v_r)$ as shown in Equation (6).

$$\frac{dz}{dt} = v_r - \frac{\sigma_0 |v_r|}{g(v_r)} z \tag{6}$$

where,

$$g(v_r) = \mu_c + (\mu_s - \mu_c) e^{-\left|V_r/V_s\right|^{\alpha}} \tag{7}$$

In this equation, $\mu_s$ and $\mu_c$ represent the static and kinetic Coulomb friction coefficients, respectively, $v_s$ is the Stribeck sliding velocity, α is a shaping factor that is used to capture the shape of the friction-slip curve, and $\sigma_0$ has been redefined as the lumped longitudinal stiffness normalized by the nominal normal force. The LuGre model has also extended the force equation to include an additional micro-damping term $\sigma_1$and a viscous friction term $\sigma_2$, as shown in Equation (8). An equivalent model of this bristle friction used in the LuGre model can be represented as shown in Figure 8 [20].

$$F_t = (\sigma_0 z + \sigma_1 \dot{z} + \sigma_2 v_r) F_n \tag{8}$$

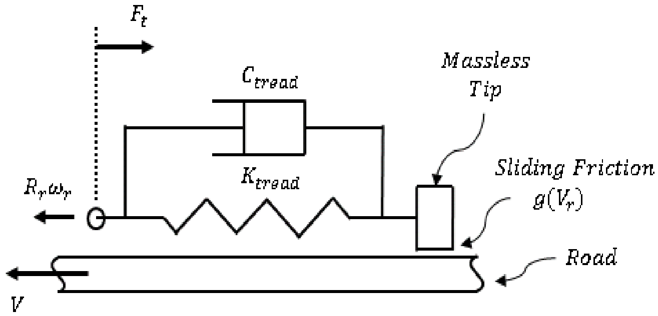

**FIGURE 8: EQUIVALENT SCHEMATIC FOR LUGRE FRICTION MODEL [20]**

The Lumped LuGre model can also be expanded into a distributed model by making the state variable $z$ a function of both time and the bristle element position $\zeta$. The equations for bristle deflection and the differential friction force are then represented as follows:

$$\frac{dz}{dt}(\zeta, t) = v_r - \frac{\sigma_0 |v_r|}{g(v_r)} z(\zeta, t) \tag{9}$$

$$dF(\zeta, t) = \left(\sigma_0 z(\zeta, t) + \sigma_1 \frac{\partial z}{\partial t}(\zeta, t) + \sigma_2 v_r\right) dF_n(\zeta, t) \tag{10}$$

Even though the Distributed LuGre model is a more accurate and detailed model than the single contact point Lumped LuGre model, the computational size of the distributed model is significantly higher due to the large number of states that must be solved. While this may be acceptable when only system modeling is of concern, it can be problematic when the model is used for control purposes [18]. A solution to this issue is to define an average friction state $\bar{z}$ in order to allow for the model to be solved as an ordinary differential equation, as shown in Equation (11).

$$\bar{z} = \frac{1}{F_n}\int_0^L z(\zeta, t) f_n(\zeta) d\zeta \tag{11}$$

where, the total normal force $F_n$ is given by:

$$F_n = \int_0^L f_n(\zeta) d\zeta \tag{12}$$

Using this approach allows us to develop the Average Distributed LuGre friction model. Solving this differential equation results in the following equation:

$$\dot{\bar{z}}(t) = v_r - \frac{\sigma_0 |v_r|}{g(v_r)} \bar{z}(t) - \kappa(t)|r\omega|\bar{z}(t) \tag{13}$$

where $\kappa(t)$ represents the normal force distribution along the contact patch and, when the boundary conditions are zero (i.e. $f_n(0) = f_n(L) = 0$) , it can be defined as follows:

$$\kappa(t) = -\frac{\int_0^L \left( z(\zeta, t) \frac{\partial f_n(\zeta)}{\partial \zeta} \right) d\zeta}{\int_0^L \left( z(\zeta, t) f_n(\zeta) \right) d\zeta} \tag{14}$$

At this point, the normal force distribution function $\kappa(t)$ can be described for various force distributions, such as uniform, parabolic, or exponentially decreasing distribution. For further explanation of these distributions, the reader is referred to [18].

In summary, the LuGre friction model is able to capture the pre-sliding displacement effects and the Stribeck effect as well as several other friction characteristics such as variable breakaway forces and the hysteretic friction loops caused by periodic changes in the relative velocity $v_r$. Due to its relatively simple form and its ability to capture the dominant dynamic friction effects, the LuGre model has been extensively used in controls [21-24]. However, it has been discovered that the LuGre model gets very stiff when the relative velocity is large, thus prompting the use of a modified LuGre model for experimental tests. A modification that has been proposed by Lu, et al. [25] recognizes that the dynamic friction effects are only evident when the relative velocity is small (i.e. in the region before peak mu). The authors develop a continuous function that makes a smooth transition from the LuGre model at low relative velocities to a static friction model at the larger relative velocities. Initial simulations seem to indicate that this solution solves computational aspects of the model without significant loss in accuracy. However, experimental results have not been performed to validate this modification.

## 2.3 TRACTION/ABS CONTROLLERS

### 2.3.1 ACCELERATION-BASED ABS CONTROLLERS

In this section, a wheel acceleration-based ABS controller that has been modeled after the ABS control algorithm outlined by the ABS system supplier Bosch [26], will be introduced. The ABS controller cycles through various control phases and is designed around a set of predetermined peripheral wheel acceleration thresholds that are highlighted in Figure 9 [26, 27].

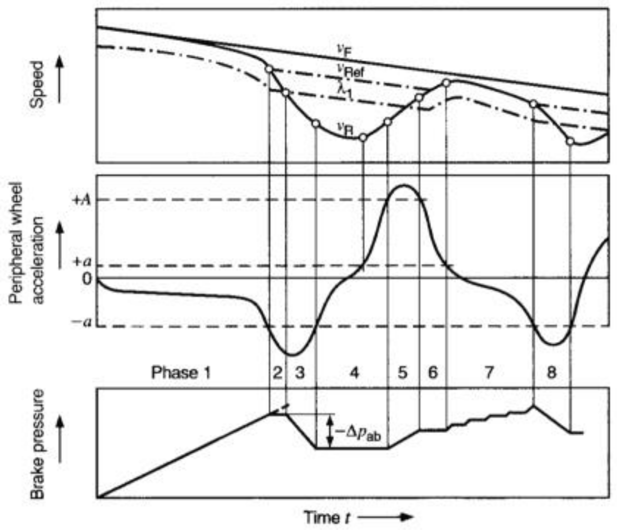

**FIGURE 9: BOSCH WHEEL-ACCELERATION BASED ABS ALGORITHM**

When the ABS is triggered, it enters the first phase where the brake pressure increases until the peripheral wheel acceleration crosses the threshold (-*a*). The controller then switches to holding the brake pressure (Phase 2), to ensure that the tire friction has become fully saturated. Once the slip switching threshold ($\lambda_1$) has been reached, the controller will reduce the brake pressure (Phase 3) until the wheel peripheral acceleration exceeds the threshold (-*a*). Phase 4 represents a pressure holding phase where the wheel begins to accelerate again as the ring slip enters the stable region of the μ-slip curve. Phases 5 through 7 then represent various stages of pressure holding and pressure increases in order to approach the maximum friction coefficient. Once the peripheral wheel acceleration again crosses the threshold (-*a*) then the ring slip is assumed to be in the unstable region.

The controller then immediately returns to Phase 3, where the brake pressure is decreased, and the cycle is repeated. Once the estimated vehicle velocity has fallen below a set minimum speed then the controller is deactivated and the brake pressure is allowed to increase, up to the master cylinder pressure, until the vehicle reaches a complete stop.

Rule-based wheel acceleration controllers have been the standard commercial ABS solutions since Bosch first introduced their controller in 1978. For the past 35 years, this style of controller has become by far the most common commercial ABS controller structure due its simplicity, acceptable performance over various surfaces, acceptable tunability, and apparent robustness. However, new technology and modern tires continue to evolve the stability[1] and performance of this type of ABS controller begins to come into question.

### 2.3.2 ADAPTIVE TRACTION CONTROLLERS

In recent years, there has been an increased interest in adaptive traction control systems that use the previously mentioned dynamic friction models [18, 21, 23-25, 28-30]. One of the original papers to take this approach was completed by Canudas-de-Wit et al

---

[1] In this thesis, a system is said to be stable if the ring slip ratio can be kept bounded and convergent within an arbitrary range of the maximum friction coefficient's corresponding ring slip ratio, $\lambda_m$ ,in the presence of a wheel torque input or external disturbance. In this research, the range will be taken as $0 \leq \lambda < (\lambda_m + 0.1)$

[18] in which they utilized the LuGre friction model and assumed that all of the tire tread parameters were known except for the friction curve. Variation of the friction curve with road surfaces was taken into account by introducing a gain $\theta$ on the friction function $g(v_r)$ that was interpreted as the coefficient of road adhesion. A gradient-type adaptation law was then introduced to estimate this term during the maneuver. The authors designed a controller to track a desired slip ratio based on an estimation of the maximum friction coefficient at the current vehicle velocity. Figure 10 shows how the gain $\theta$ changes the friction curves under steady-state conditions and has been shown in [18] to correlate well to the Magic Formula. This paper, along with [29], also implemented an observer to estimate velocity and the internal states using only the wheel angular velocity measurement.

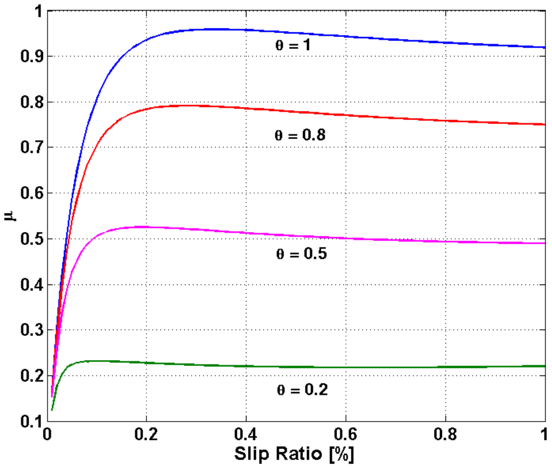

FIGURE 10: STATIC VIEW OF AVERAGE LUMPED LUGRE MODEL WITH VARYING GAIN

In [29], the work of Canudas-De-Wit et al was expanded to show that the state estimations guaranteed underestimation of the maximum friction coefficient when the correct initial conditions were chosen. Underestimation of the friction coefficient guarantees that the estimated maximum friction coefficient will be lower than the actual maximum friction coefficient. This is a very useful feature, from a safety perspective, if the estimated total stopping distance is desired. However, it should be noted that the author has not proven that underestimation of the corresponding slip ratio is also guaranteed, which would ensure that the desired slip reference is not unstable. Furthermore, the utilization of only wheel angular velocity resulted in an estimator that was slow to converge due to a lack of persistent excitation, a problem common with most adaptive controllers. In order to overcome this issue, Alvarez, et al [23] proposed an adaptive control law that used both wheel angular velocity and vehicle longitudinal acceleration to estimate the states while still guaranteeing underestimation of the maximum friction coefficient under suitable choices of adaptation gains and initial conditions. In addition to this improvement the authors also assume that the tread dynamics parameters $\sigma_0$, $\sigma_1$, and $\sigma_2$ are unknown. These parameters were then able to be estimated using a regressor-based gradient-type adaptation law. Their results show that due to these improvements the internal friction states converge to their true values within approximately 0.5 sec. While this improvement helped with the persistence of excitation condition, it wasn't eliminated. Additional improvements can be made in this area to further minimize the effect of an absence in persistence of excitation, such as a dead-zone and projection mapping. A dead-zone will stop the parametric estimation when the estimation error is less than some predetermined value, thus preventing parameter drift in the presence of small excitations. Projection mapping, on the other hand, forces the observer to recognize bounds on the estimated parameters and prevents the parameter estimations from diverging. Both of these modifications can add a level of robust stability to the closed-loop system; however, neither completely removes the persistence of excitation requirement for guaranteed parameter convergence.

In addition, the reviewed research in this area has still not taken into consideration the tire's rigid-ring torsional dynamics and the effects that it may have on the controller's performance. The present work seeks to address this deficiency in the field.

### 2.3.3 SLIDING MODE TRACTION CONTROLLERS

Another approach towards addressing the tire's parametric uncertainties is to use a robust controller such as a sliding mode controller. Sliding mode control is designed so that the desired state dynamics are constrained to a hyper-plane, known as the sliding surface. There have been many sliding mode Traction/ABS controllers developed over the past two decades. Some of these controllers assume a constant slip ratio that must be tracked [31-33], while others propose an extremum-search method to maintain the longitudinal force at its maximum [34, 35].

Many recent papers that have utilized the LuGre friction model in order to estimate the friction states and the desired slip ratio use sliding mode controllers [30, 36-41]. In

Patel, et al [30], the authors propose two distinct sliding mode controllers based on the equivalent output error injection and assume that only the wheel angular velocity is measurable. The first controller includes a second-order sliding mode observer that is independent of the tire/road friction model. The second controller introduces a third-order fixed-gain sliding mode observer, that is based on the LuGre friction model, in order to estimate the friction gain $\theta$ that was introduced in [18]. Simulations of the controllers were conducted when paired with multiple friction models (i.e. the LuGre model, a Pseudo-static LuGre model, and a basic static friction model) in order to diffuse controller-friction model sensitivity concerns. However, this controller assumes that all of the friction parameters are known *a priori*, a condition that is not realistic.

In Kayacan et al [40] a sliding mode controller is used in conjunction with a grey predictor in order to estimate the upcoming values of both the reference and wheel slip ratios. Both simulations and physical experimentation were conducted and showed that the introduction of the grey predictor reduced the effect of signal noise and unmodeled disturbances on the system response. However, this paper only used the steady-state estimation of the LuGre friction model to locate the desired slip ratio, and stopped short of utilizing the dynamic LuGre model or tire dynamics to improve the controller response. The research reported in Magallan, et al [39] uses a sliding mode observer to estimate the internal friction state for a full vehicle, instead of a quarter-mass vehicle as described in the previous papers. By including the full vehicle dynamics, the observer was designed to be robust to variations in tire normal force. The authors have also proposed a controller which regulates the maximum longitudinal force allowable instead of tracking a desired slip ratio. This maximum allowable force is calculated by estimating the maximum steady-state friction force, similar to the method originally proposed in [18]. However, in order to make this estimation, it is assumed that the LuGre frictional parameters and the friction shaping function are known.

Even though in the past few years there has been a dramatic increase in the amount of research being conducted on Traction/ABS controllers combined with sliding mode controllers and dynamic friction models, there still appears to be no investigation on including the tire's rigid-ring torsional dynamics into the controller design. And as will be shown later, in Section 3.4, the tire's torsional dynamics can cause significant oscillations in the angular wheel velocity, thus having the potential to affect the performance and even the stability of the controller.

### 2.3.4 ADAPTIVE ROBUST CONTROLLERS

There has been recent research using a robust controller that utilizes projection-based parameter adaptation techniques to provide estimates of the internal friction state $z$ from the LuGre friction model for position tracking [25, 42, 43]. In these papers, all of the friction parameters, except for the friction shape function $g(v_r)$, are unknown and must be estimated. This is accomplished by utilizing a dual-observer structure, for faster parameter convergence, combined with projection mapping (to ensure robustness to modeling errors) that was originally developed by Tan & Kanellakopoulos [28]. The friction model was then modified by transitioning from the LuGre model to a static friction model as the relative velocity increased, due to reasons stated in Section 2.2.2. The authors utilized a combination of nonlinear robust control with traditional adaptive control techniques to improve the system's steady-state error and transient performance[2].

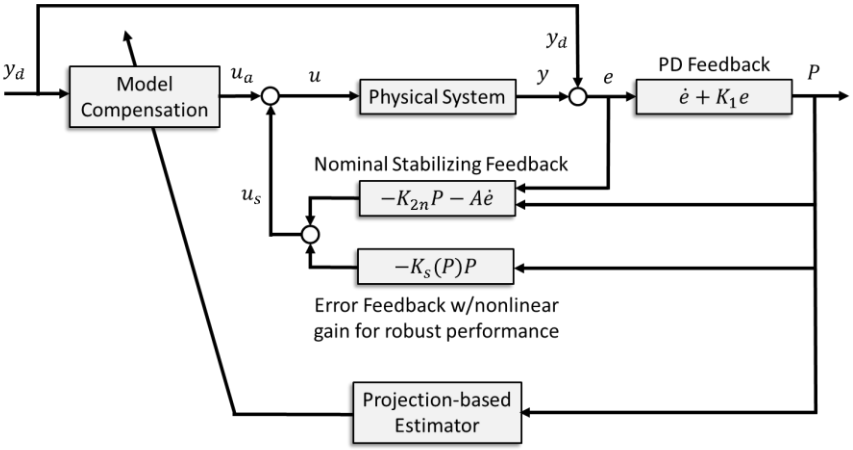

**FIGURE 11: A SIMPLIFIED ADAPTIVE ROBUST CONTROLLER [42]**

The basic structure of this controller can be seen in Figure 11 [42] and is briefly described as follows. In an attempt to achieve perfect tracking an inverted plant model is estimated and a control action is generated which is close to ideal. Since this model is just an estimate of the physical plant a projection-based observer is used to estimate the disturbances and/or parametric uncertainties. However, during this adaptation period, or

---

[2] In this manuscript, transient performance is defined in the time domain and refers to a combination of the system's

- rise time - the time it takes to reach 90% of the final value
- settling time - the time after which the output remains within 5% of its final value
- and overshoot - the quotient of the peak and final value (which should generally be <20%)

when unmodeled external disturbances are present, perfect tracking may not be achieved. So, a nominal stabilizing feedback law is introduced which drives the error to zero and provides some robust stability[3] in combination with the projection-based observer. However, there is no guarantee on the robust performance[4]. To address this, a nonlinear robust control law is introduced to achieve this robust performance. As detailed in [42], it can be shown that, if the model uncertainties have a known bound, then there will always be a nonlinear robust control law that will produce a continuous or sufficiently smooth control input and will guarantee any arbitrarily strict robust performance requirements (given no actuator saturations).

This controller was tested through simulations and experiments on a linear motor gantry crane and showed good tracking performance over a range of relative velocities [25]. In [44] and [45] a slightly modified version of the adaptive robust control structure was used to design the force-loop controller of an active hydraulic suspension system and showed a closed-loop bandwidth of 10 Hz, a significant improvement from the 4Hz in previously reported adaptive controllers. In Bu & Tan [46], the adaptive robust control structure was utilized for automated precision stopping of heavy vehicles with a nonlinear

---

[3] Robust stability is defined as a guarantee of the closed-loop system stability for all perturbed plants within a known bounded region from the nominal plant.

[4] Robust performance can be defined as a guarantee of the transient performance for all perturbed plants within a known bounded region from the nominal plant.

pneumatic braking system and showed good results over various vehicle loadings and road conditions.

The adaptive robust control scheme appears to have desirable characteristics for a Traction/ABS controller, such as robust stability and robust performance. This proposed work would adapt these general ideas and investigate similar schemes for braking/traction control applications.

# CHAPTER 3: SYSTEM MODELING

In this chapter, a detailed simulation model of the braking system dynamics of a small passenger vehicle is developed. It includes tire sidewall torsional deflection, dynamic tread-ground friction effects, and brake hydraulics. In addition, an experimental quarter-car test fixture is introduced which has the capability of using either traditional brake hydraulics or a custom-built electro-mechanical brake system to apply brake torque.

## 3.1 TIRE/WHEEL TORSIONAL MODEL INCLUDING DYNAMIC CONTACT FRICTION

As discussed in Chapter 2, the tire/wheel model that is used throughout this paper only includes the torsional deflection of the sidewall, as this is considered to be the dominant effect on the response of the tire/wheel system onto which the braking/driving inputs are applied. The two-inertia model used throughout the remainder of this research is shown in Figure 12. The sidewall's torsional stiffness and damping coefficient are denoted by $K_T$ and $C_T$, respectively. The Average Lumped Parameter LuGre friction model detailed in the previous chapter is also used throughout this research due primarily to its low computational cost and suitability for control oriented analysis and design. The schematic for this model is shown in Figure 13, where $K_{tread}$ and $C_{tread}$ are the tread stiffness and damping coefficient, respectively.

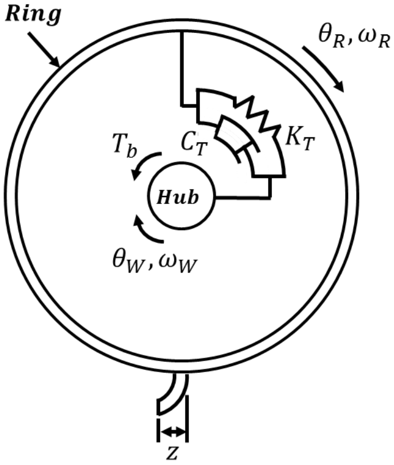

FIGURE 12: HUB/TIRE MODEL

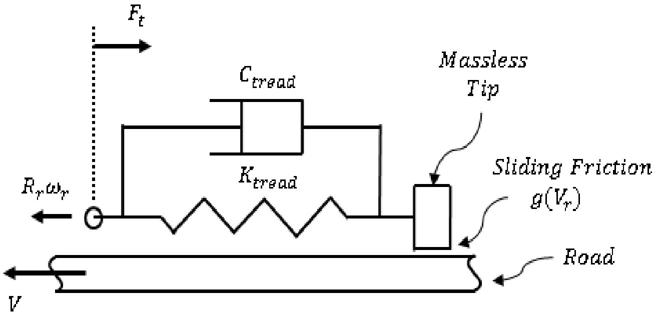

FIGURE 13: SCHEMATIC FOR THE LUGRE FRICTION MODEL

Considering a quarter vehicle model along with the above tire/wheel and tread/ground friction model, the equations describing the system reduce to the following:

$$J_w * \frac{d\omega_w}{dt} = K_t(\theta_r - \theta_w) + C_t(\omega_r - \omega_w) - T_b \tag{15}$$

$$J_r * \frac{d\omega_r}{dt} = F_t R_r - K_t(\theta_r - \theta_w) - C_t(\omega_r - \omega_w) \tag{16}$$

$$\frac{m_v}{4} * \frac{dV}{dt} = -F_t \tag{17}$$

$$F_t = F_z(K_{tread} z + C_{tread}\dot{z}) \tag{18}$$

$$V_r = V - R_r * \omega_r \tag{19}$$

$$\dot{z} = V_r - \frac{K_{tread}|V_r|}{g(V_r)} z - k|\omega_r|R_r z \tag{20}$$

$$g(V_r) = \mu_c + (\mu_s - \mu_c)e^{-\left|{V_r}/{V_s}\right|^{\alpha}} \tag{21}$$

where, $J_w$ and $J_r$ designate the hub/wheel and ring inertias, $T_b$ designates the braking torque, and $F_t$ designates the ground force. Equation 3 gives the longitudinal braking dynamics of the quarter vehicle, where aerodynamic and rolling resistance contributions have been neglected. In this work, the vehicle parameters for a small passenger vehicle (1991 Mazda Miata) are considered. In addition, the 'Stribeck' friction curve has been extrapolated from experimental data for a wet surface where the static ($\mu_s$) and kinetic ($\mu_C$) coefficients of friction are 0.75 and 0.4, respectively, and the shaping factor (α) has been determined as 0.75. This fitted Stribeck friction curve is shown in Figure 14, which also shows the comparison to the experimentally determined friction curve measured on an asphalt surface.

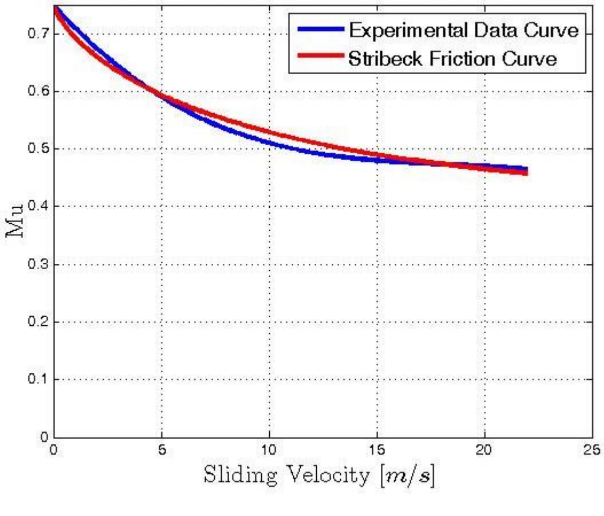

FIGURE 14: ROAD FRICTION COEFFICIENT CURVE FOR A WET SURFACE

## 3.2 LINEARIZED RESPONSES OF TIRE/WHEEL TORSIONAL MODEL

It is useful to quantify certain linearized characteristics, such as the natural frequency and damping ratio of the tire/wheel system in a free-free state, where the nonlinear friction forces and the tread dynamics are ignored. This quantification allows for a useful relative comparison between the two tires, but it should be recognized that the natural frequency of the system, when loaded on the ground, is actually somewhere between the free-wheel fixed-ring frequency and the fixed-wheel free-ring frequency, depending on the tire's slip ratio. The results for the free-free natural frequency are [47]:

$$\omega_n = \sqrt{\frac{K_T(J_r + J_w)}{J_r * J_w}} \tag{22}$$

$$\zeta = \frac{C_T}{2} * \sqrt{\frac{J_r + J_w}{K_T(J_r * J_w)}} \tag{23}$$

Table 1 below shows computed values of these parameters for two tire designs that were used in the simulation studies. The torsional stiffness values for the two designs are experimentally determined, and the torsional damping coefficient was merely selected to keep the damping ratio at the typical value of 0.05. Tire 1 is a low torsional stiffness tire (lower torsional natural frequency), and Tire 2 is a tire with the torsional stiffness of a standard pneumatic tire.

TABLE 1: VARIOUS TIRE PARAMETERS

| | $K_T$ $\left[\frac{N * m}{rad.}\right]$ | $C_T$ $\left[\frac{N * m * sec.}{rad.}\right]$ | $J_r$ $[kg * m^2]$ | $J_w$ $[kg * m^2]$ | $\boldsymbol{\omega_n}$ $[\boldsymbol{Hz}]$ | $\boldsymbol{\zeta}$ |
|---|---|---|---|---|---|---|

| | | | | | | |
|---|---|---|---|---|---|---|
| **Tire 1** | 7616 | 2.5 | 1 | 0.093 | **47.6** | **0.05** |
| **Tire 2** | 19438 | 4 | 1 | 0.093 | **76.1** | **0.05** |

## 3.3 BRAKE SYSTEM DYNAMICS

Figure 15 shows the main components of such a hydraulic braking system configured for ABS [48]. In the model adopted, the hydraulic dynamics before the inlet and outlet valves have been ignored; assuming that, the subsequent valve responses and pressure (compressibility effects) dynamics dominate the hydraulic dynamics. This is equivalent to assuming that the build-up phase for the master cylinder pressure is neglected. Equations (24)-(28) list the equations derived for describing the dynamics of the brake system under these assumptions.

$$\frac{dP_c}{dt} = \frac{\beta}{V} * (q_i - q_o) \tag{24}$$

$$q_i = C_d * A_{vi} * \sqrt{\frac{2}{\rho}(P_m - P_c)} \tag{25}$$

$$q_o = C_d * A_{vo} * \sqrt{\frac{2}{\rho}(P_c - P_{atm})} \tag{26}$$

$$A_v = u_v \frac{K_v e^{-s\tau}}{1 + s\tau} \tag{27}$$

$$T_b = P_c(2A_b R_b \mu_{cal}) \tag{28}$$

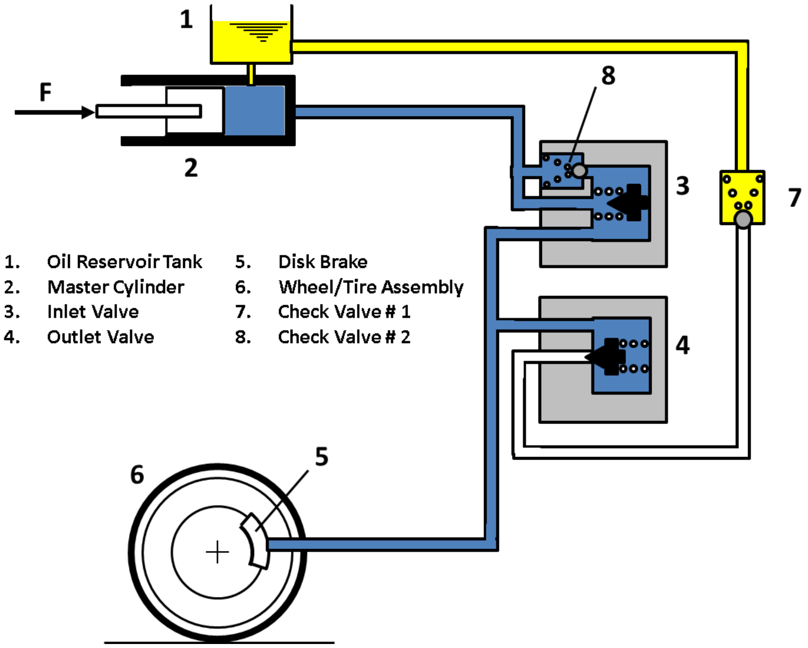

FIGURE 15: SCHEMATIC OF BRAKE HYDRAULICS

Equation (24) represents the caliper cylinder pressure dynamics as a function of the bulk modulus and volume of the fluid and the flow rate through the brake lines. Equation (25) and Equation (26) give the flow rates through the inlet and outlet valves, respectively. Equation (27) models how the effective valve area changes with the valve input, the gain of the valve, delays and its time constant. And lastly, Equation (28) converts the pressure from the brake lines into the torque that is applied by the caliper on the wheel hub given two brake pads at a given radius from the wheel center at a given pad friction coefficient. A more detailed model of the brake system is given in [48].

The brake system parameters have been determined from both physical measurements and reference [49] to represent typical characteristics of a hydraulic braking system for a small passenger car (the 1991 Mazda Miata). The following values were used throughout the simulations:

β=1 GPa; ρ=0.85 kg⁄L; P_m=5 MPa ; A_max=0.5 mm^2 ; C_d=0.6 ; V=50 cm^3

The time constant for the caliper pressure dynamics is found to be of the order of 15 ms. When cascaded with the valve dynamics, which has a time constant of 10 ms, this produces an overall brake caliper pressure response (to valve input) on the order of 20ms.

## 3.4 OPEN-LOOP RESPONSE OF COMBINED TIRE/BRAKE SYSTEM

The tire and brake system models presented above are connected together and the responses of the combined system to step changes in valve voltage (input, and output valves) are analyzed. Figure 16 shows this transient response in terms of the longitudinal force coefficient (μ) vs. the wheel and ring slip ratios ($\lambda_w$ , $\lambda_r$) at each instant during this simulated hard braking event. These quantities are defined as:

$$\mu = \frac{F_t}{F_z} \qquad \lambda_w = 1 - \frac{\omega_w R}{V} \quad and \;\; \lambda_r = 1 - \frac{\omega_r R}{V}$$

It can be seen in the left side of Figure 16 that for the low torsional stiffness tire (Tire 1), the force coefficient builds up to the Stribeck curve, at approximately 10% ring slip ratio, and then smoothly follows just under the Stribeck friction curve until it reaches full lockup. It also shows that for a given value of the force coefficient, the wheel slip ratio lags the ring slip ratio during the force build up phase and once it reaches the peak force coefficient, the wheel slip ratio exhibits oscillations around the ring slip ratio. We can make parallel observations on the effect of sidewall flexibility by referring to the right side of Figure 16, which shows the torsional angle between the wheel and the ring during the same hard braking event. During initial force build up, there is an increase in the relative torsional angle until a peak value of μ is achieved. Then the wheel and ring oscillate relative to each other with an average twist of around 0.029 radians until the wheel locks-up and the ring continues to oscillate about the wheel.

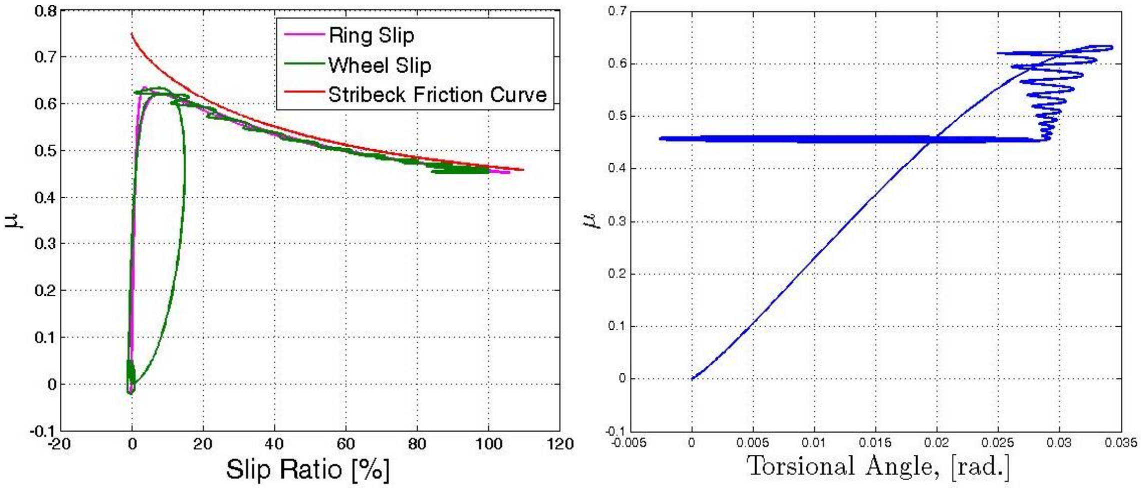

**FIGURE 16: OPEN-LOOP RESPONSE WITH TORSIONAL DYNAMICS**

These results confirm that, in the presence of tire torsional flexibility, there is a distinction between the behavior of the ring and wheel slip ratios during a hard braking event. Since most, if not all, Traction/ABS controllers are based on the wheel slip ratio, one can expect there to be some interaction with the controller.

## 3.5 EXPERIMENTAL ABS FIXTURE

### 3.5.1 HYDRAULIC-BRAKE BASED TEST FIXTURE

Figure 17 through Figure 20 show the test rig developed for experimental validation of the proposed work. A McPherson strut suspension assembly has been installed on the test fixture and comes from the front right corner (quarter) of a 2010 Toyota Yaris. The suspension strut from the Toyota Yaris has been replaced by a turnbuckle to allow for adjustment of the wheel height (and load) in the vertical direction. The range of the suspension travel has been designed to accommodate various tires and tire sizes that may be tested. The suspension is then connected to a 6-DOF load cell and subsequently mounted to the chassis dynamometer floor.

A complete hydraulic braking system has also been constructed using components from a 2010 Toyota Yaris which includes a brake booster, master cylinder, ABS modulator, brake lines, brake disc, and brake caliper. The brake booster is connected to a vacuum

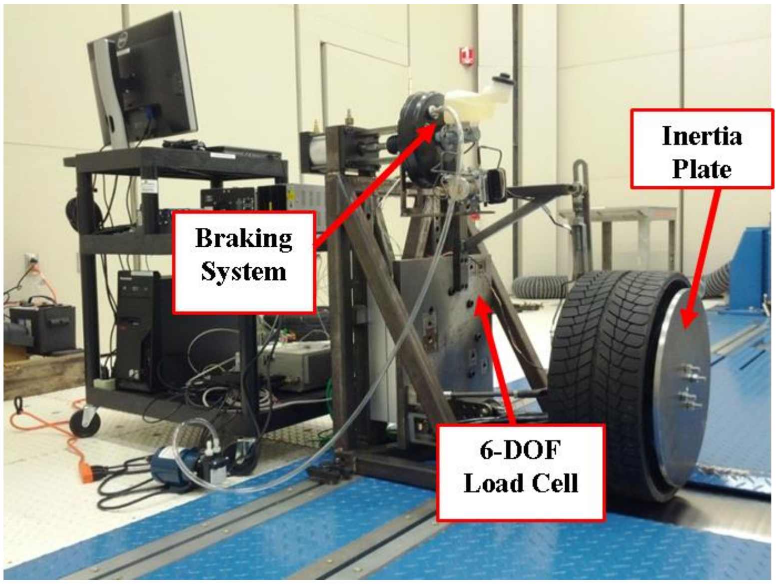

FIGURE 17: EXPERIMENTAL TEST RIG - OVERVIEW

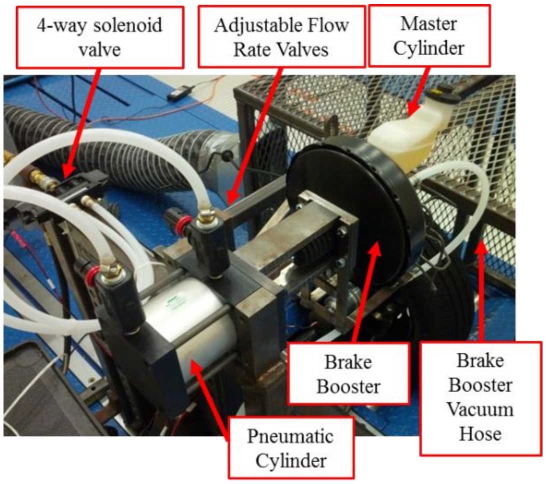

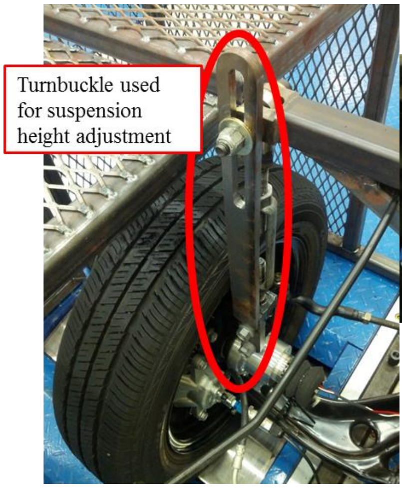

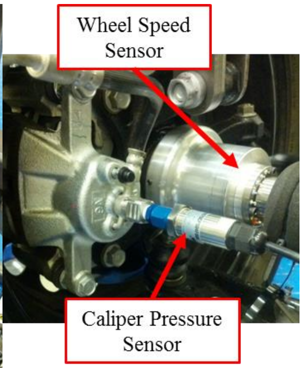

FIGURE 18: EXPERIMENTAL TEST RIG – HYDRAULICS

FIGURE 19: EXPERIMENTAL TEST RIG - SUSPENSION

FIGURE 20: EXPERIMENTAL TEST RIG - SENSORS

pump. For repeatability of tests, the “brake pedal” application force to the brake booster is emulated by a 2-way pneumatic cylinder that is actuated by a 4-way solenoid valve, and has adjustable flow rates and steady-state operating pressures. Multiple inertia masses can also be added onto the test specimen to represent variations in the inertia of the wheel (i.e. due to changes in driveline inertia, wheel inertia, etc…).

The test rig is controlled through the combination of a dSPACE MicroAutoBox Control hardware, which implements the braking/traction control strategy, and the chassis dynamometer controller, which simulates the vehicle under braking. The sensors that are available for use with the dSPACE controller include wheel rotational velocity, brake caliper pressure, and the chassis dynamometer velocity. The dSPACE controller outputs include the pneumatic cylinder solenoid voltage, the ABS modulator input and output valve voltages, and the ABS modulator return pump voltage.

Initial open-loop tests were performed in order to characterize the dynamic response of the experimental braking system. These tests were completed by applying and releasing brake caliper pressure through various valve actuation, while the wheel was at a standstill, and measuring the pressure delay and lag times. Through the use of various valve actuation combinations, the brake hydraulic system can be broken up into three distinct sections, as shown in Figure 21. Section 1 represents the hydraulic section between the master cylinder and the input valve. Section 2 consists of the fluid between the input valve and the caliper. Section 3 is from the output valve to check valve #1.

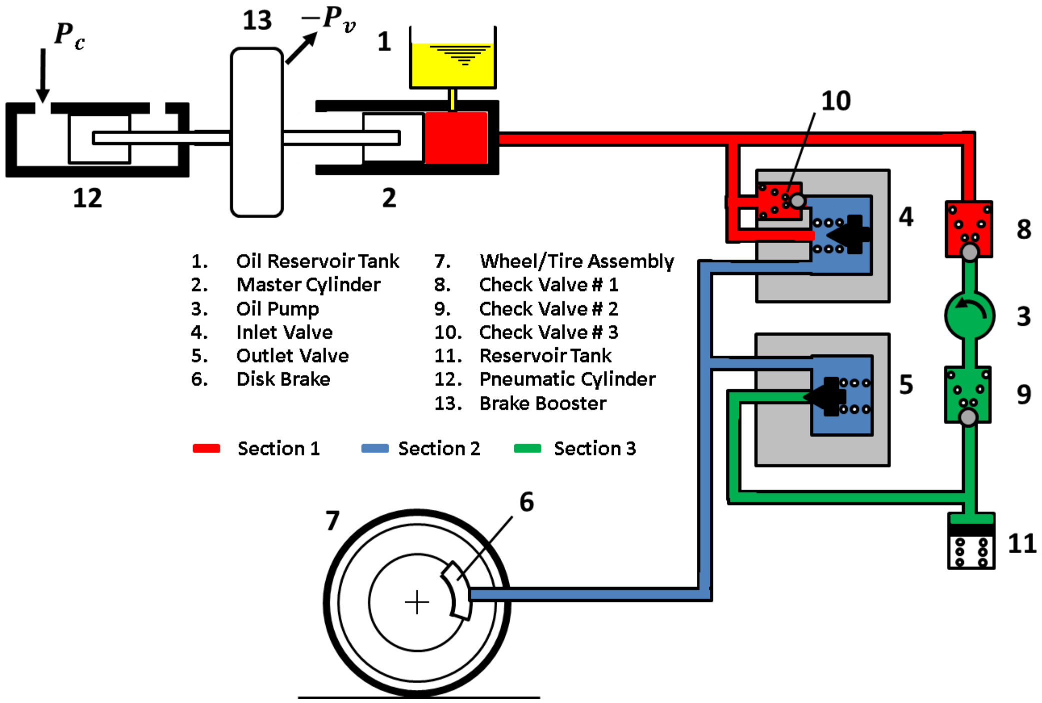

FIGURE 21: SCHEMATIC OF BRAKE HYDRAULICS

Before discussing the results of these experiments, it should be noted that this hydraulic system is slightly different from the system used in the simulations, due to the differing routing of section 3 and the addition of the hydraulic reservoir tank and return pump. This change in the hydraulic routing can affect the pressure release dynamics. Therefore, steps have been taken to make the simulation hydraulic response match as closely as possible to the experimental dynamics through variations in the inlet and outlet valve cross-sectional areas.

The results of these open-loop tests and comparisons with the simulation-based model can be seen in Table 2. For Section 1 & 2, the pneumatic cylinder pressure is applied fully and released with no interaction with the ABS modulator valves. The pressure apply dynamics have a 0.1s delay and a 0.12s time constant, while the pressure release dynamics are significantly faster with a 0.04s delay and a 0.038s time constant. This trend continues in the individual tests of Section 2 & Section 3, where the master cylinder pressure is applied, but the brake caliper pressure is controlled through the ABS modulator valves.

TABLE 2: OPEN-LOOP RESPONSE OF EXPERIMENTAL TEST RIG

| | **Apply Time Delay** | **Apply Time Constant (Bandwidth)** | **Simulation-model Apply Time Constant (Bandwidth)** | **Release Time Delay** | **Release Time Constant (Bandwidth)** | **Simulation-model Release Time Constant (Bandwidth)** |
|---|---|---|---|---|---|---|
| **Section 1 & 2** | 0.1 sec. | 0.12 sec.<br>(1.3 Hz) | N/A | 0.04 sec. | 0.038 sec.<br>(4.2 Hz) | N/A |
| **Section 2** | 0.01 sec. | 0.08 sec.<br>(2.0 Hz) | 0.08 sec.<br>(2.0 Hz) | N/A | N/A | N/A |
| **Section 3** | N/A | N/A | N/A | 0.01 sec. | 0.03 sec.<br>(5.1 Hz) | 0.031 sec.<br>(5.3 Hz) |

Also, as mentioned previously, the test rig has the ability to adjust the inertia of the wheel hub by adding various inertia plates. These inertia plates can be used to simulate changes in wheel inertia due to changes in the transmission gears on a driven wheel and also provide the ability to make a direct correlation of the controller performance due to variations in inertia. The initial inertia plates that has been machined range from 0.1-0.613 $kg * m^2$ increase in inertia, which is representative of a small passenger vehicle in a various transmission gears. As can be seen in Table 3, this added inertia can have a significant effect on the torsional free-free natural frequency of the wheel/tire system; in this case, it reduces the overall free-free frequency by almost 55%.

**TABLE 3: TIRE RESPONSE WITH VARYING INERTIA**

| | $K_T\left[\frac{N*m}{rad.}\right]$ | $J_r\ [kg*m^2]$ | $J_w\ [kg*m^2]$ | $\boldsymbol{\omega_n}\ [\boldsymbol{Hz}]$ |
|---|---|---|---|---|
| **Tire 1: w/o Inertia** | 7616 | 1 | 0.093 | **47.6** |
| **Tire 1: w/ Inertia Option 1** | 7616 | 1 | 0.093 + 0.1 | **34.5** |
| **Tire 1: w/ Inertia Option 2** | 7616 | 1 | 0.093 + 0.25 | **27.5** |
| **Tire 1: w/ Inertia Option 3** | 7616 | 1 | 0.093 + 0.35 | **25.1** |
| **Tire 1: w/ Inertia Option 4** | 7616 | 1 | 0.093 + 0.54 | **22.3** |
| **Tire 1: w/ Inertia Option 5** | 7616 | 1 | 0.093 + 0.64 | **21.4** |
| **Tire 1: w/ Inertia Option 6** | 7616 | 1 | 0.093 + 0.79 | **20.3** |
| **Tire 1: w/ Inertia Option 7** | 7616 | 1 | 0.093 + 0.89 | **19.7** |

### 3.5.2 ELECTROMECHANICAL-BRAKE BASED TEST FIXTURE

The experimental fixture has also been designed to allow for the hydraulic system to be exchanged for an electromechanical brake system. The reason for this modification is to allow easier and more precise control of the brake torque as well as to improve the bandwidth of the braking system.

The electromechanical brake utilizes a planetary gearset and a ballscrew to multiply the motor torque and transfer the rotational motion to linear motion at the brake caliper, as shown in Figure 22. It should be noted that the only reason for the ballscrew, planetary gearbox, and the 90° gearbox transformation is due to space constraints. By adding the gearbox an additional dynamic system is introduced which can reduce the stiffness and thus the bandwidth of the completed braking apparatus as well as add

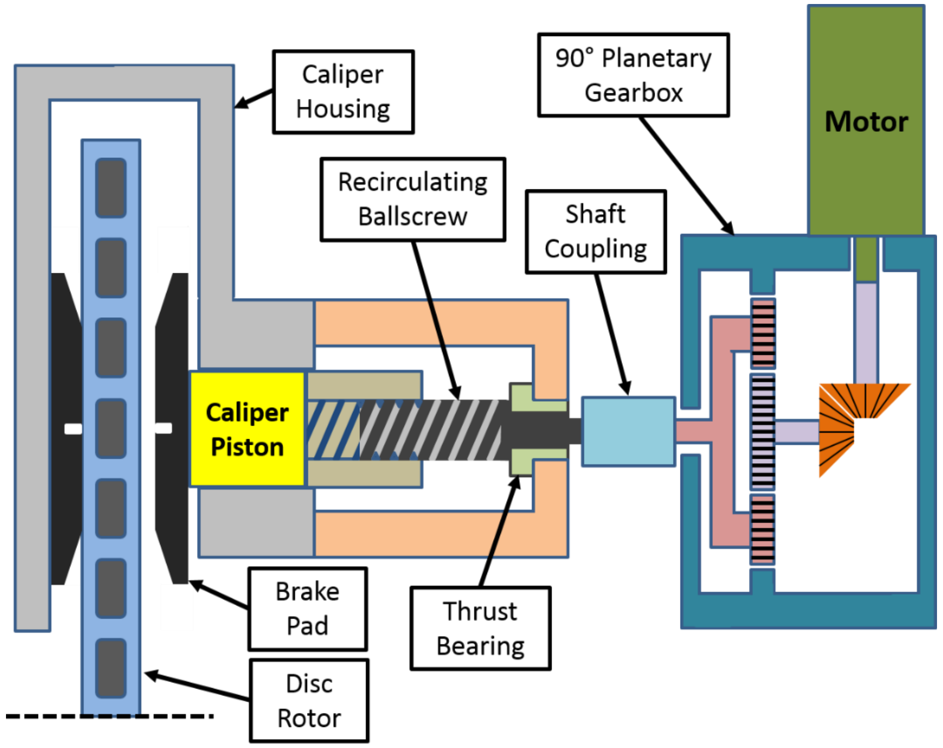

FIGURE 22: EMB SCHEMATIC

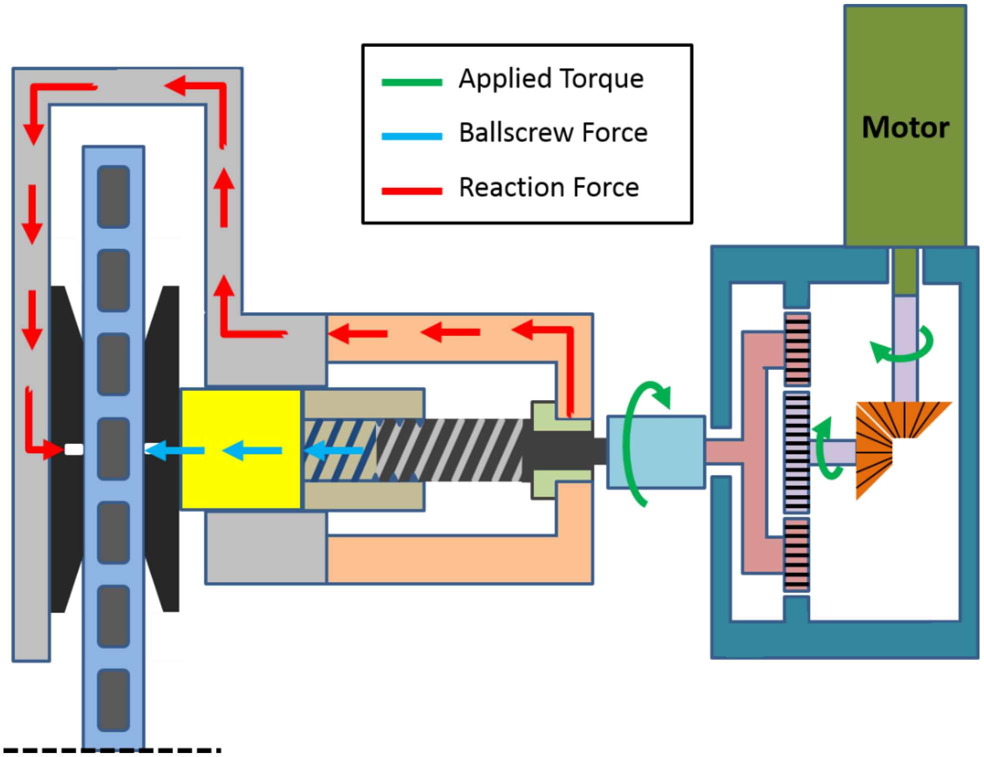

FIGURE 23: EMB LOADING PATH

backlash into the system. A ballscrew was chosen instead of a traditional leadscrew to significantly decrease the friction and hysteresis in the system; however, the dynamics of the ballscrew still have the possibility to add complicated dynamics into the system.

Figure 23 shows the loading path that is experienced by the electromechanical brake system under braking. The torque that is applied to the ballscrew is translated to an axial load on the interior brake pad. This force has to be reacted back through the ballscrew and thrust bearing back into the caliper housing. This then results in an equal and opposite force being applied on the exterior brake pad. Utilization of this force path (which represents the standard force path for a brake caliper) minimizes the axial loads on the gearbox and allows both brake pads to experience equal normal loads[5].

Figure 24 shows a detailed drawing of the designed system, where it can be seen that the motor and gearbox are fixed against the fixture's back plate, and thus do not require the ball screw to carry any of the weight of the motor. And Figure 25 - Figure 27 show the fabricated and mounted system on the ABS fixture. In addition to the electromechanical brake system a higher resolution velocity encoder (1024 pulse quadrature decoder) was connected to the wheel to provide accurate and high frequency measurements of the wheel speed.

---

[5] Note that the coupling between the gearbox and the ballscrew has been designed to allow motion in the axial direction, thus allowing the caliper freedom to move laterally and minimizing the axial loads on the gearbox.

In order to get a 1st order estimate of the dynamics of the electromechanical brake system, a load cell was put in place of the disc rotor, which can be seen in Appendix B, and a step input in control voltage was supplied to the motor controller. The response of this input can be seen in Figure 28 below as a compressive force on the load cell. The figure shows that an 1800 mV step in control voltage resulted in a 14kN step in caliper normal load, which is more than sufficient to generate the required braking torque.

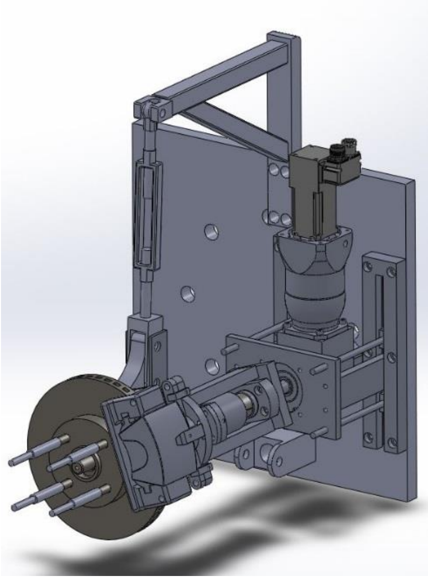

FIGURE 24: DETAILED EMB DRAWING

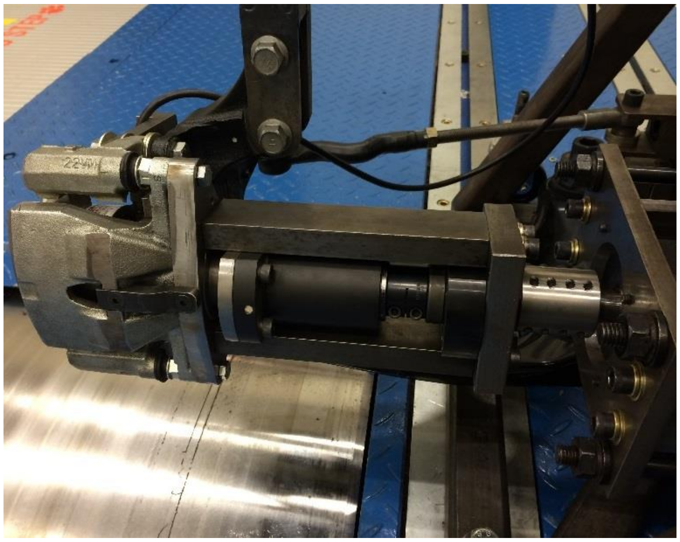

FIGURE 25: FABRICATED EMB

FIGURE 26: FIXTURE OVERVIEW (VIEW 1)

FIGURE 27: FIXTURE OVERVIEW (VIEW 2)

The braking system was further characterized through a sine sweep torque command given to the motor controller. The measured response as well as a 3rd order transfer function estimation of the system is presented below in Figure 30. This 3rd order model can then be used to get an estimate of the phase and magnitude response of the EMB system, as shown in Figure 29. The bandwidth of the system, calculated as -3dB from the peak gain at 1Hz (chosen as the DC gain was not able to be clearly defined due to signal limitations) is approximately 34Hz. This bandwidth is significantly higher than the hydraulic braking pressure apply (2.0 Hz) and release (5.3Hz) bandwidths.

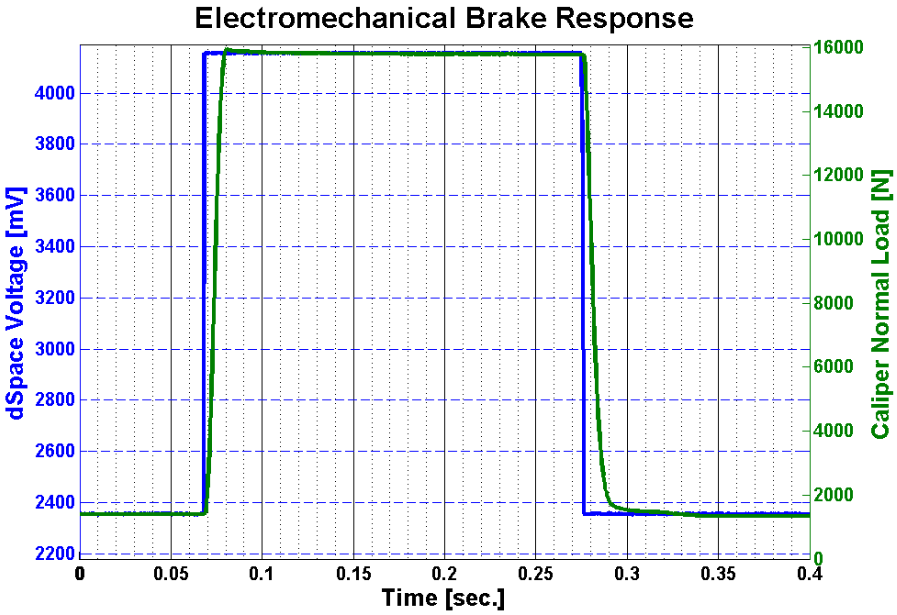

FIGURE 28: EMB STEP RESPONSE

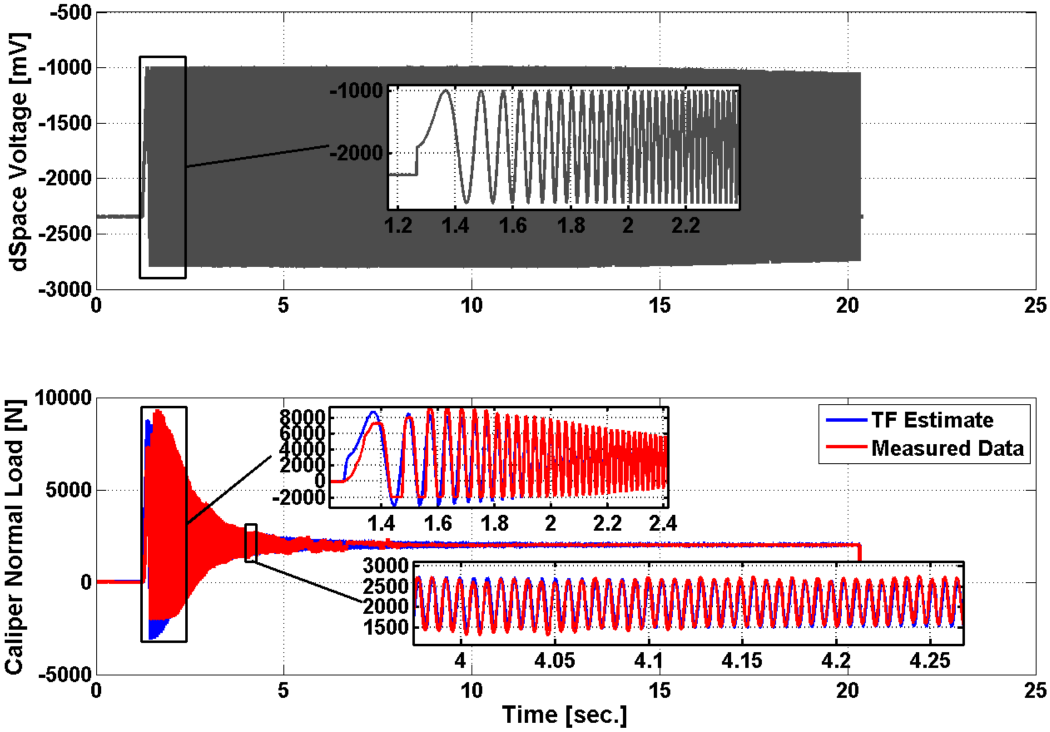

FIGURE 30: EMB TRANSFER FUNCTION ESTIMATION

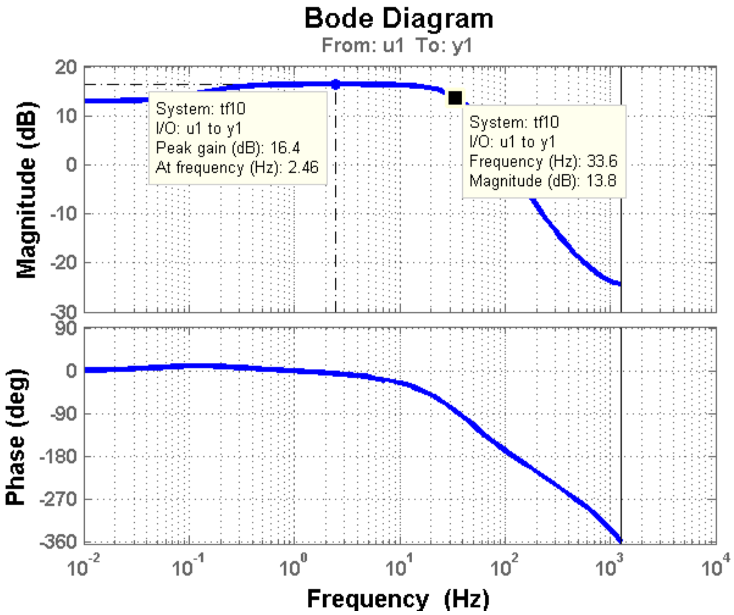

FIGURE 29: EMB ESTIMATION OF BODE DIAGRAM

## 3.6 CHAPTER SUMMARY

In this chapter, a detailed tire torsional model combined with the Average Lumped Parameter LuGre friction model was developed for a quarter-car model with brake hydraulics. An experimental test fixture was also introduced that has the ability to switch between traditional brake hydraulics or electro-mechanical brake (EMB) system. The EMB system was designed and implemented in order to increase the bandwidth of the brake torque application system, thus allowing the controllers to be developed in later chapters to take advantage of the tire’s torsional dynamics.

# CHAPTER 4: PERIPHERAL WHEEL ACCELERATION CONTROLLER

The objective of this chapter is to conduct an investigation on the interactions of tire/wheel designs with the workings of typical commercial ABS control system. To this end, sensitivity studies of the commercial ABS controller are conducted on the achievable braking performance by changing the parameters of the ABS control algorithm and the various tire and wheel design parameters. These studies will be used to highlight the influence that the tire torsional characteristics can have on the standard commercially available ABS controller based on peripheral wheel acceleration. The observations obtained through simulation work will also be validated with experimental investigations performed on the quarter-vehicle hydraulic-brake based ABS braking test fixture.

## 4.1 MODELING OF A PERIPHERAL WHEEL ACCELERATION ABS CONTROLLER

For the purpose of this research an acceleration-based ABS controller is adopted as a controller that is representative of a commercially viable ABS structure that mainly uses wheel-acceleration information computed from wheel speed sensor signals. This acceleration-based ABS controller has been modeled after the ABS control cycles that have been published by the ABS system supplier Bosch [26]. The ABS controller cycles through various control phases is designed around a set of predetermined wheel-acceleration thresholds that are highlighted in Figure 31. For a detailed description of the cycles and thresholds please refer to Appendix C.

Since the controller acts upon wheel acceleration thresholds, it is instructive to analyze the open-loop acceleration responses for a tire (Tire 2) following a step increase in valve voltage, as shown in Figure 32. It can be seen that the unfiltered wheel acceleration exhibits large magnitude oscillations before it begins to converge on a specific acceleration. The unfiltered ring acceleration shows oscillations that are smaller, but similar.

Figure 32 also shows the open-loop response for Tire 2 under different filter settings. For the investigations in this work, the filter type was chosen to be 4th-order Butterworth filter due to its good balance between a reasonable roll-off of $80dB\ /\ decade$ and minimal added phase lag. The 15Hz filter, which will roll off to -20dB at approximately 27Hz, is decent at filtering out the tire/wheel dynamics. With the 15Hz filter the signal is somewhat similar to the unfiltered ring accelerations as some of the torsional dynamics attributed to the sidewall (and the high frequency tread dynamics) have been filtered out;

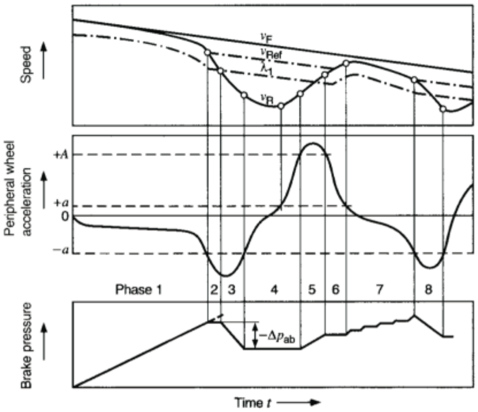

FIGURE 31: BOSCH WHEEL-ACCELERATION BASED ABS ALGORITHM

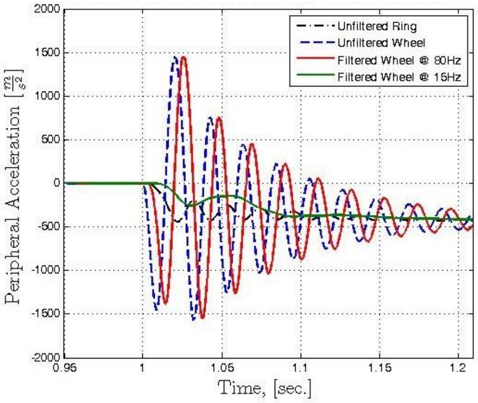

FIGURE 32: STEP-RESPONSE OF UNFILTERED & FILTERED TANGENTIAL ACCELERATIONS FOR OPEN-LOOP HUB/TIRE MODEL (SIMULATION)

however the filtered signal still misses some of the oscillations that can be observed in the ring dynamics. The controller is designed to act upon these gradual filtered acceleration changes so that there is a smooth flow between the controller phases.

The simulation responses for the ABS controller are presented below in Figure 33, where after multiple trial and error simulations, an appropriate set of controller thresholds have been determined. As can be seen the controller, by using the filtered wheel acceleration data, is somewhat effective at controlling the ring slip and velocity throughout the event; although the controller struggles to maintain a consistent slip ratio. Also, as shown earlier, the unfiltered wheel accelerations are rather oscillatory and very noisy; but, the filter removes most of the oscillations from the wheel accelerations to attempt to be more representative of the ring dynamics.

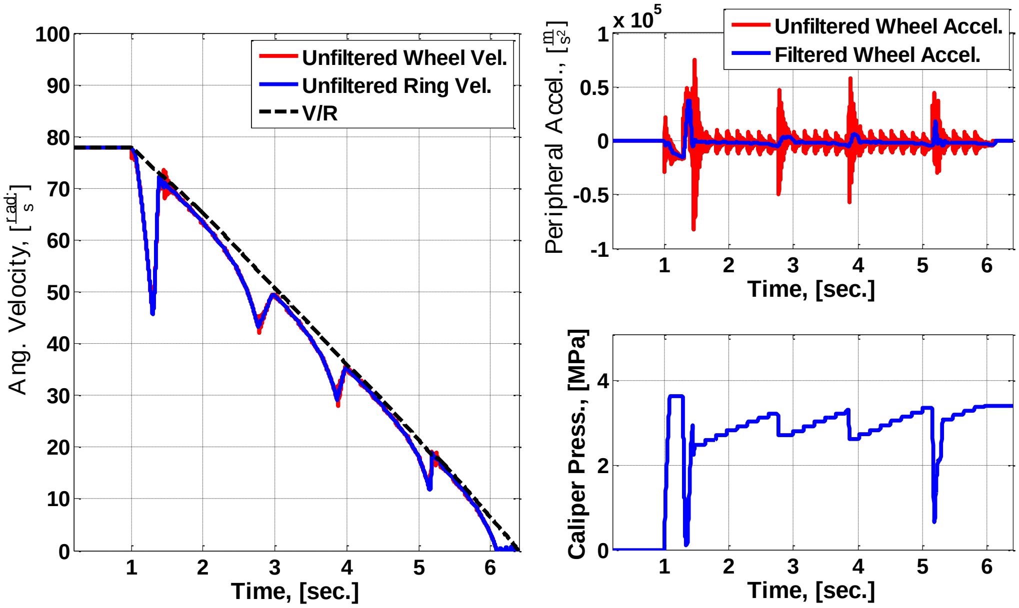

FIGURE 33: ACCELERATION-BASED CONTROLLER RESPONSE FOR TIRE 1 PARAMETERS

The experimental system responses for the acceleration-based ABS controller with the low-torsional stiffness tire are presented below in Figure 34, with a 10Hz filter cutoff frequency and utilizing the hydraulic-brake based test fixture. The controller controls the wheel slip ratio and produces a response that is very similar in nature to the simulation based results. It should be noted that upon initial braking there are some initial oscillations in the response that were not present in the simulation-based testing. However, these oscillations appear to settle within approximately 0.5 sec. It is thought that these initial vibrations may be due to flexibilities in the suspension system, which were not included in the simulation model, and inherent experimental limitations on wheel acceleration estimations.

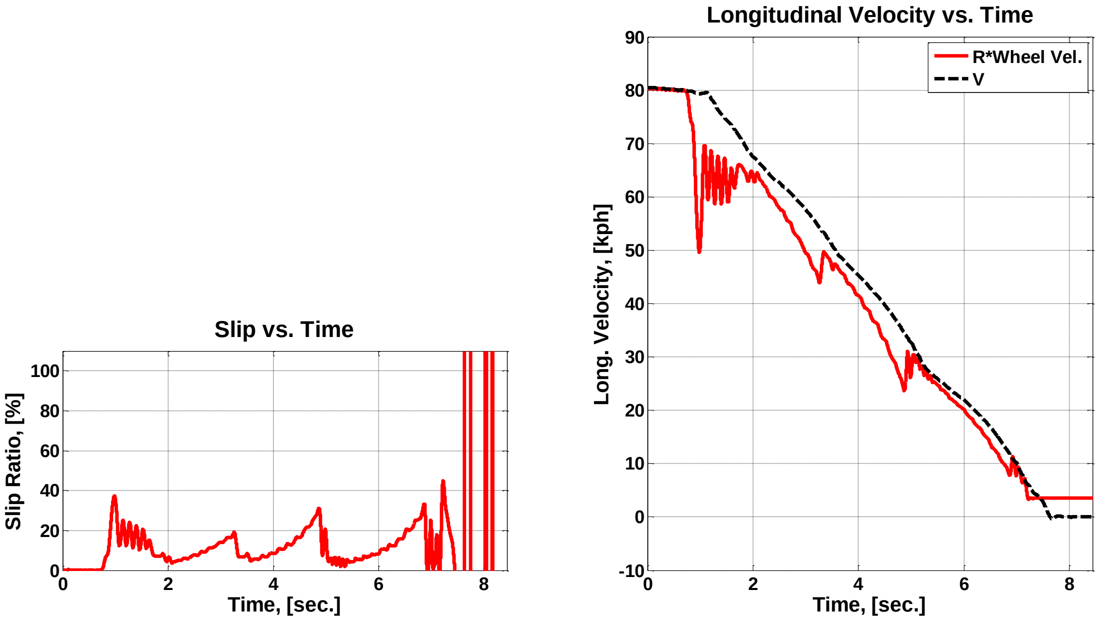

FIGURE 34: EXPERIMENTAL RESPONSE OF ACCELERATION-BASED ABS CONTROLLER

## 4.2 SENSITIVITY STUDY TO TIRE/WHEEL PARAMETERS

### 4.2.1 EFFECT OF FILTER CUTOFF FREQUENCY

Figure 35 shows the simulation-based sensitivity results where the controller was nominally designed for the Tire 2 with a 15Hz filter cutoff frequency, as represented by the black dot. The filter cutoff frequency was then varied between 1.5Hz and 80Hz. As expected, the stopping distance and control activity are minimized at the nominal cutoff frequency of 15Hz. It is interesting to note that if the filter cutoff frequency is lowered, below approximately 12 Hz, the stopping distance dramatically increases. This can be attributed to a low cutoff frequency filter removing most of the tire-wheel dynamics from the system and resulting in an ABS system that can only respond to the upper and lower wheel slip ratio thresholds. However, if the cutoff frequency of the filter is increased significantly above the nominal frequency then the control activity begins to increase. This is explained by noting that at these settings, the tire-wheel torsional dynamics have not been sufficiently filtered. This causes the controller to become more active as the most extreme thresholds ($+A$ and $-a$) are easily crossed causing the controller to quickly switch between pressure-increase and pressure-decrease states. This also results in a controller that is ineffective and will consistently saturate at the upper or lower wheel slip ratios.

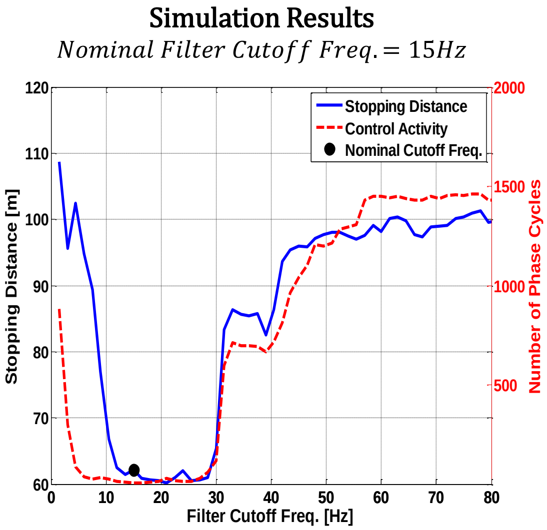

FIGURE 35: CUTOFF FILTER FREQUENCY SENSITIVITY STUDY FOR TIRE 2 PARAMETERS – SIMULATION RESULTS

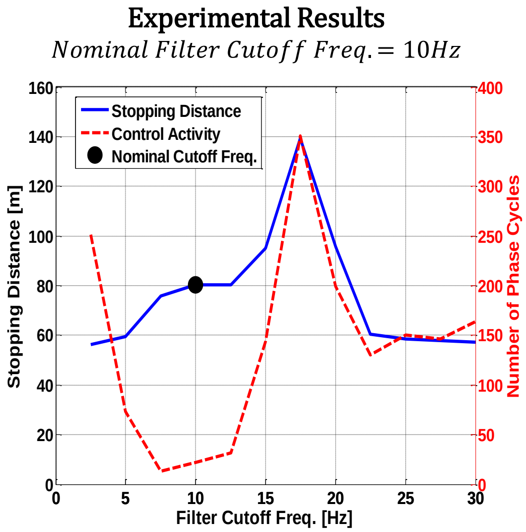

FIGURE 36: CUTOFF FILTER FREQUENCY SENSITIVITY STUDY FOR TIRE 2 PARAMETERS – EXPERIMENTAL RESULTS

Figure 36 shows the results for the Tire 2 tire on the experimental test rig, with a nominal filter cutoff frequency of 10Hz. Due to limitations of the experimental rig, the filter frequency could only be varied from 2.5Hz to 30Hz. However, this frequency range was sufficient to capture the same trends as seen through the simulation results. At the nominal 10Hz case both the control activity and stopping distance were small. And, when the filter frequency was lowered most of the tire-wheel dynamics were removed from the wheel speed signal, which caused an ineffective controller. In the experimental case, there is an increase in the control activity instead of the stopping distance that was observed through simulations. This is due to the fact that in the simulations the controller tended to saturate at the lower wheel slip ratio threshold (which results in a higher stopping distance), while the experimental results tended to saturate at the upper wheel slip ratio (which results in a higher control activity). Neither scenario is desired, but both cases are due to the fact that the wheel speed signal has been filtered too aggressively. Figure 36 also shows that when the filter cutoff frequency is increased significantly beyond its nominal value the control activity again begins to increase; thus resulting in an inefficient controller because the tire/wheel torsional dynamics have not been filtered out. It should also be noticed that even though the control activity decreases after 17.5Hz, the relative control activity still remains significantly larger than nominal and thus still represents an ineffective controller.

The above analyses suggest that even if the torsional stiffness of the tire is varied, the controller will continue to perform as designed as long as the cutoff filter frequency satisfies two conditions:

- The filter cutoff frequency must remain above some minimum frequency for the controller to achieve good performance (stopping distance) with minimal activity.
- The filter cutoff frequency must be set low enough that it will effectively remove the tire/wheel sidewall dynamics from the wheel accelerations used by the controller.

Therefore, when designing the controller and filter parameters, it is logical to set the filter cutoff frequency close to the lower limit in order to accommodate the largest range of tire torsional stiffness.

### 4.2.2 SENSITIVITY TO SIDEWALL TORSIONAL STIFFNESS

Next we consider the sensitivity of the controller to changes in the sidewall torsional stiffness $K_T$. In each case, the controller and filter parameters have been designed for a nominal tire/wheel set. Then, the tire torsional stiffness is varied while the controller and filter parameters are held constant. Simulation-based results, as seen in Figure 37, showed very clearly that there is an increase in control activity when the torsional stiffness was lowered. This was due to the fact that as the torsional stiffness was decreased the torsional natural frequency of the tire approached that of the filter cutoff frequency; thus creating a system that did not effectively filter out the torsional dynamics of the sidewall and resulted in an ineffective controller.

In experimental testing, it is difficult to vary only the torsional stiffness of the system without changing the other system parameters. In an attempt to circumvent this difficulty, the tire pressure was varied while maintaining a constant normal load. A reduction in tire pressure is known to reduce the tire's torsional stiffness; however it will also increase the contact patch length, thus increasing the effective tread stiffness. It is assumed, however, that the torsional stiffness will be the parameter most influenced by the change in the tire pressure.

Figure 38 shows the results for Tire 1 when the inflation pressure was varied. The controller was tuned for the nominal 30 psi inflation pressure. Increases in tire pressure had no effect on the controller's performance. Once the tire pressure decreased below a certain value, thus causing the tire's torsional natural frequency to encroach upon the filter cutoff

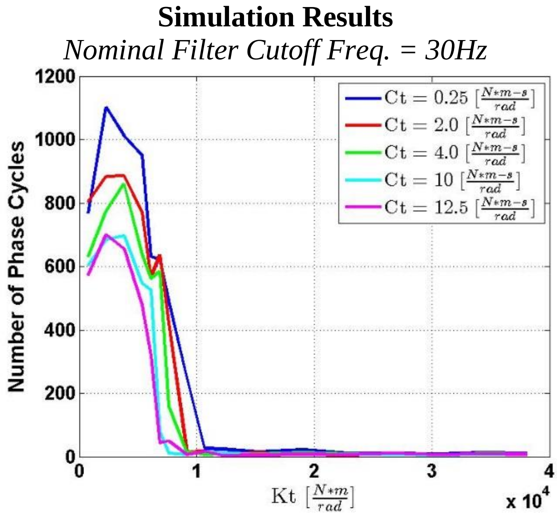
Simulation Results

*Nominal Filter Cutoff Freq. = 30Hz*

**FIGURE 37: KT/CT SENSITIVITY STUDY FOR TIRE 1 PARAMETERS- CONTROL ACTIVITY**

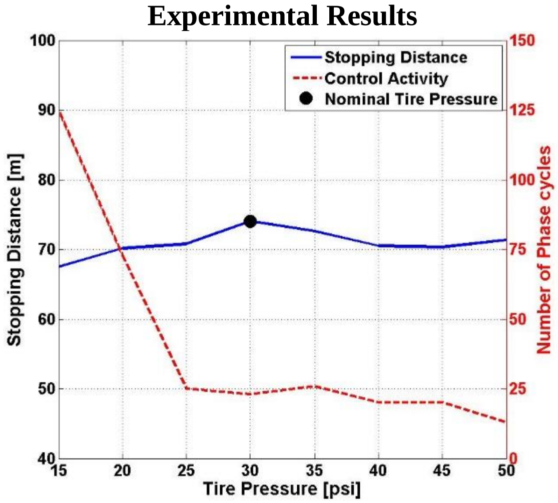
Experimental Results

**FIGURE 38: KT SENSITIVITY STUDY FOR TIRE 1 PARAMETERS- CONTROL ACTIVITY**

frequency, the control activity increased dramatically. This degradation in controller performance is because the torsional natural frequency of the wheel/tire system has been decreased sufficiently so that the filter is no longer effective at filtering out the torsional sidewall dynamics. This reaffirms that it is desirable to set the filter cutoff frequency as close to the lower limit as possible in order to account for the largest range of tire torsional stiffness. Notice that there wasn't a significant change in stopping distance, but this cannot be guaranteed as the controller is not operating as designed when there is such a dramatic increase in control activity (at very low tire pressures).

### 4.2.3 Sensitivity to Wheel and Ring Inertia

Since there is a strong correlation between the free-free torsional natural frequency with respect to the filter cutoff frequency and the controller's performance it is important to evaluate the effect of the wheel and ring inertia on the system. Simulation results show that at high values of both wheel and ring inertia there is an increase in control activity and a trend towards an increase in stopping distance (as shown in Figure 39). This is due to the fact that at high values of inertia the natural frequency of the system is significantly decreased and begins to approach the filter cutoff frequency. However, if the ring inertia is varied individually there is no significant change in the controller performance. This is because the torsional natural frequency is fairly insensitive to changes in ring inertia without a corresponding change in wheel inertia.

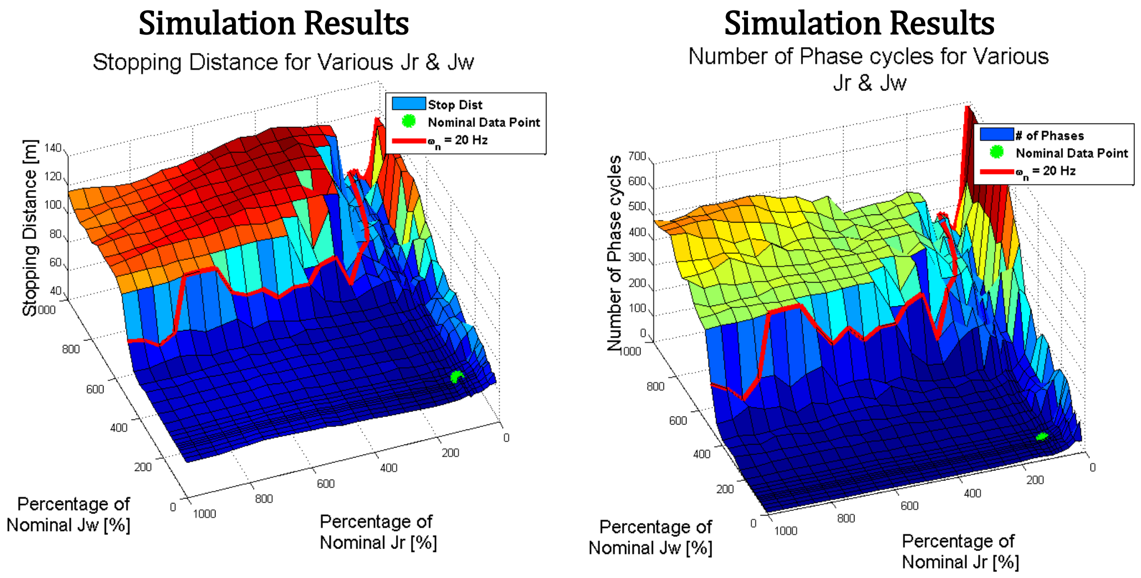

**Figure 39: $J_R$ / $J_W$ Sensitivity Study for tire 1 -- Tuned for Filter Cutoff Frequency = 15Hz**

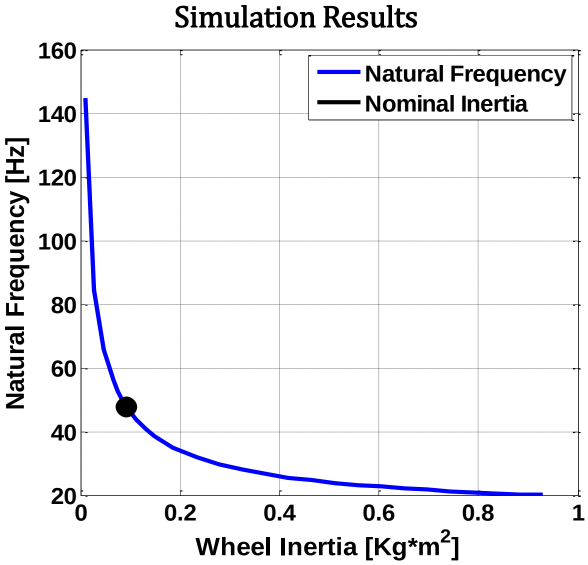

Figure 40: Tire 2 Torsional Natural Frequency vs. Wheel Inertia

There is also a similar trend when only the wheel inertia is varied, although it is not as prominent. Figure 40 shows the change in torsional natural frequency with variations in wheel inertia (as given by Equation 8). Initially the torsional frequency is sensitive to the wheel inertia, but as the inertia is increased dramatically the natural frequency approaches an asymptote around 20 Hz.

In the experimental tests, the ring inertia was unable to be varied independently, and the wheel inertia could only be increased through various combinations of inertia plates that were attached to the wheel. In Figure 41, simulation results show that when the wheel inertia is increased beyond 0.3 $Kg * m^2$ there is an increase in the controller activity, due to the decrease in the tire’s torsional natural frequency. However, the control activity appears to saturate at large values of added inertia due to the limitations mentioned above. Figure 42 shows the results of the same test performed on the experimental test rig. Here

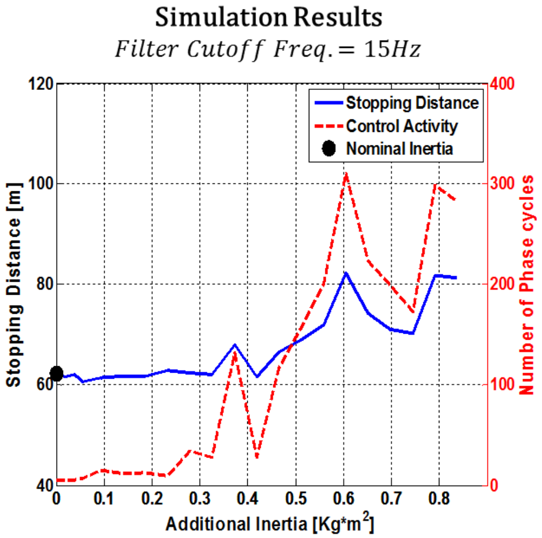

FIGURE 41: $J_W$ SENSITIVITY STUDY FOR TIRE 2 – SIMULATION

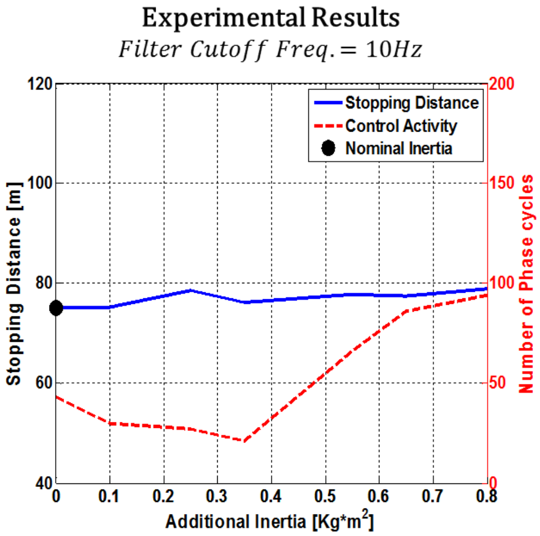

FIGURE 42: $J_W$ SENSITIVITY STUDY FOR TIRE 2 - EXPERIMENTAL

the data shows a similar trend to the simulations as the control activity begins to increase beyond a given wheel inertia and the controller again becomes ineffective at controlling the event. Furthermore, during these tests it was observed that at high values of wheel inertia the controller produced chatter.

## 4.3 CHAPTER SUMMARY

This chapter presented simulation-based and experimental analysis of the interaction between a commercial ABS controller's settings and tire torsional design parameters. The main observations can be summarized as follows:

- The filter cutoff frequency must remain above a certain minimum limit (e.g. 15Hz for the ABS controller in the simulations and 10Hz for the experimental tests) in order to prevent the wheel dynamics from being completely filtered out.

- The filter cutoff frequency must be set sufficiently low enough to filter out the dynamics from the dominant torsional mode

These observations highlight the inability of current commercial ABS controllers to account for tire torsional dynamics. While the controller’s cutoff filter frequency can be designed to allow for a larger range of torsional stiffness’, it is achieved at the expense of ignoring relevant tire dynamics. It is not difficult to imagine that further improvement in performance can be achieved by designing an ABS controller that takes these dynamics into account. In Chapter 5 an adaptive nonlinear traction controller is proposed that incorporates the tire’s torsional and tread dynamics.

# CHAPTER 5: ADAPTIVE NONLINEAR CONTROLLER

Even though in the past few years there has been an increase in the amount of research on traction/ABS controllers and dynamic friction models, there still appears to be no investigation on including the tire's torsional dynamics into the controller design. The objective of this chapter is to expand upon the work of Alvarez, et al. [23] to include and adapt to the tire's sidewall parameters. This chapter will focus on the case where both the tire sidewall and tread parameters are unknown. It has been assumed that the vehicle velocity and the friction function are known based on extensive work completed in this area [23, 24, 29, 50-52]. In addition, this work systematically constructs a virtual damper via backstepping techniques [53, 54] to devise a nonlinear adaptive controller that accommodates tires with low torsional damping.

## 5.1 PARAMETER AND STATE ESTIMATION

In this section, the parameter adaptation laws are formulated. The following parameters are assumed unknown: $\mathrm{K_{tread}},\ \mathrm{C_{tread}},\ \mathrm{K_t},\ \mathrm{C_t}, \text{and } \mathrm{J_w}$.[6] Rearranging Equation (17) and combining with Equations (15), (16), and (19) results in:

$$\frac{\mathrm{dV_r}}{\mathrm{dt}} = -(\mathrm{g} + \mathrm{a}) * \mu + \frac{\mathrm{R_r}}{\mathrm{J_r}}(\mathrm{J_w}\dot{\omega}_\mathrm{w} + \mathrm{T_b}) \tag{29}$$

---

[6] A limitation of this scheme is the assumption that $J_r$ is known. Further work needs to be completed to include this parameter in the adaptation laws.

where, g is acceleration due to gravity, $\mu = F_t/F_z$ is the coefficient of friction, and $a = (R_r^2 m_v g)/(4 * J_r)$. Then, using Equation (20) in Equation (18) and rearranging to isolate the unknown parameters $K_{tread}$ and $C_{tread}$ gives:

$$\mu = K_{tread} z + C_{tread}(V_r - k|\omega_r|R_r z) - \sigma_3 f(V_r)\, z \tag{30}$$

where, $f(V_r) = |V_r|/g(V_r)$ , and $\sigma_3 = K_{tread} * C_{tread}$ is an independent parameter introduced to address the nonlinearities of the system. Recognizing that this equation can now be placed in regressor form:

$$\mu = [z \quad (V_r - k|\omega_r|R_r z) \quad -f(V_r)\, z] * [K_{tread} \quad C_{tread} \quad \sigma_3]^T = U_1 \Sigma_1 \tag{31}$$

$$\tilde{\mu} = \hat{U}_1 \hat{\Sigma}_1 - U_1 \Sigma_1 = \hat{U}_1 \hat{\Sigma}_1 - \mu \tag{32}$$

and assuming that μ, $V$ [7], and $\omega_w$ can be measured, the following gradient-based adaptive law can be constructed:

$$\dot{\hat{\Sigma}}_1 = -\Gamma_1 \hat{U}_1^T \tilde{\mu} \quad \text{where,} \qquad \Gamma_1 = \mathrm{diag}(\gamma_0, \gamma_1, \gamma_3) > 0 \tag{33}$$

where, $\Gamma_1$ is a positive diagonal matrix of adaptation gains and $\hat{U}_1 = \left[\hat{z} \quad \left(\hat{V}_r - k|\hat{\omega}_r|R_r \hat{z}\right) \quad -f\left(\hat{V}_r\right) \hat{z}\right]$ is the regressor matrix evaluated at the estimated states.

---

[7] A significant amount of research has been conducted on the estimation of these variables. These variables are assumed known in this work.

Estimation of the sidewall torsional parameters can also be made by following a similar procedure. We assume that $T_b$ is measurable (can be inferred from bake pressure). By rearranging Equation (15) into a regressor form and solving for $T_b$:

$$T_b = [(\theta_r - \theta_w) \quad (\omega_r - \omega_w) \quad -\dot{\omega}_w] * [K_t \quad C_t \quad J_w]^T = U_2\Sigma_2 \tag{34}$$

$$\widetilde{T} = \widehat{U}_2\hat{\Sigma}_2 - U_2\Sigma_2 = \widehat{U}_2\hat{\Sigma}_2 - T_b \tag{35}$$

The following gradient-based adaptation law can be constructed:

$$\dot{\hat{\Sigma}}_2 = -\Gamma_2 \widehat{U}_2^T\widetilde{T} \quad \text{where,} \ \Gamma_2 = \mathrm{diag}(\gamma_4, \gamma_5, \gamma_6) > 0 \tag{36}$$

The gradient-based adaptation laws can be replaced with least-squares estimators and techniques such as parameter projection and dead-zones can be used add robustness to the adaptation. However, for the investigations in this part the above formulation was found sufficient.

These parameter estimates are then used to construct an estimated plant, of the same structure as Equations (15) - (21), from which the unmeasured state estimates $\hat{\theta}_r$, $\hat{\omega}_r$, and $\hat{z}$ are obtained by direct computation. See Figure 43 for a schematic.

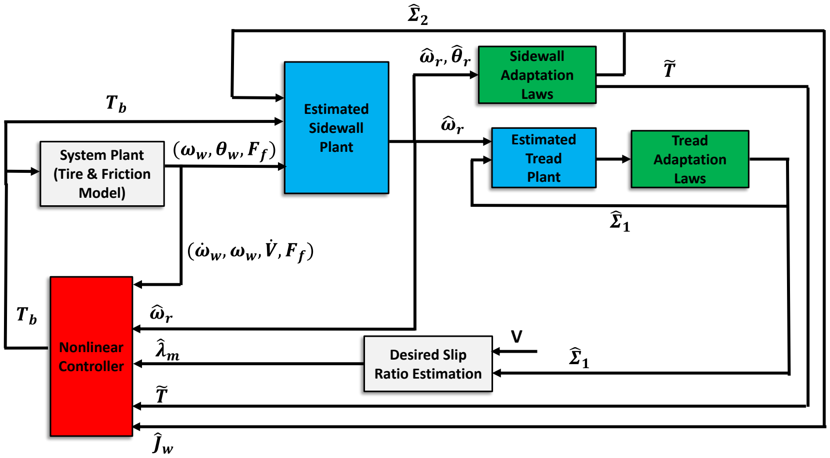

FIGURE 43: SCHEMATIC OF PROPOSED ADAPTIVE CONTROLLER SCHEME

## 5.2 NONLINEAR TRACTION CONTROLLER

The design of the controller is approached in two parts. First, it is treated as a ring slip-tracking problem. Then, additional virtual damping terms are systematically included to overcome oscillations from low tire damping.

For a traction controller, it is desirable to track the ring slip ratio that corresponds to the peak friction force in order to minimize stopping distance. This desired slip ratio $\lambda_m$ can be estimated based upon a pseudo-static computation of the LuGre friction model at a given velocity and assuming a uniformly distributed loading with a rectangular contact patch. Detailed derivations of similar equations which are based on the rigid sidewall model can be found in [18] and [50], where $\omega_r$ is replaced with the rigid wheel rotational velocity. For the purposes of this work, the computation proceeds as follows:

$$\hat{\mathrm{F}}_{\mathrm{ss}} = \mathrm{sgn}\left(\hat{\mathrm{V}}_{\mathrm{r}}\right) \mathrm{F}_{\mathrm{z}}\, \mathrm{g}\left(\hat{\mathrm{V}}_{\mathrm{r}}\right)\left(1 + 2\hat{\gamma}\frac{\mathrm{g}\left(\hat{\mathrm{V}}_{\mathrm{r}}\right)}{\hat{\mathrm{K}}_{\mathrm{tread}}\mathrm{L}\,|\hat{\eta}|}\left(\mathrm{e}^{-\frac{\hat{\mathrm{K}}_{\mathrm{tread}}\mathrm{L}\,|\hat{\eta}|}{2\mathrm{g}\left(\hat{\mathrm{V}}_{\mathrm{r}}\right)}} - 1\right)\right) \tag{37}$$

$$\hat{\gamma} = 1 - \frac{\hat{\mathrm{C}}_{\mathrm{tread}}\left|\hat{\mathrm{V}}_{\mathrm{r}}\right|}{\mathrm{g}(\hat{\mathrm{V}}_{\mathrm{r}})} \tag{38}$$

$$\hat{\eta} = \frac{\hat{\mathrm{V}}_{\mathrm{r}}}{\mathrm{R}_{\mathrm{r}}\hat{\omega}_{\mathrm{r}}} = \frac{\hat{\lambda}_{\mathrm{r}}}{1 - \hat{\lambda}_{\mathrm{r}}} \tag{39}$$

$$\hat{\lambda}_{\mathrm{r}} = \frac{V - \mathrm{R}_{\mathrm{r}}\hat{\omega}_{\mathrm{r}}}{V} = \frac{\hat{\mathrm{V}}_{\mathrm{r}}}{V} \tag{40}$$

where, $L$ is the contact patch length. An estimate of the desired slip ratio $\lambda_m$ can then be obtained by searching Equation (37) for its maximum [23, 29, 50],

$$\hat{\lambda}_m = \underbrace{argmax}_{\hat{\lambda}_r}\left\{F_{ss}(\hat{\lambda}_r\,, V_r\,, \hat{\Sigma})\right\} \tag{41}$$

Figure 44 provides an example of this steady-state curve at various vehicle velocities. Note how the maximum friction coefficient increases as velocity decreases. This trend is a result of the Stribeck curve “flattening” out with decreasing velocity when plotted against slip ratio, as shown in Figure 45. This is because the friction shaping function $g(V_r)$ is a function of the relative velocity and not the slip ratio. As the vehicle velocity decreases, the maximum relative velocity also decreases (however, the maximum slip ratio still remains at 100%). This attribute of the shaping function is also the explanation for the increase in the desired slip ratio $\lambda_{\mathrm{m}}$, which correlates with the maximum friction coefficient, as velocity decreases.

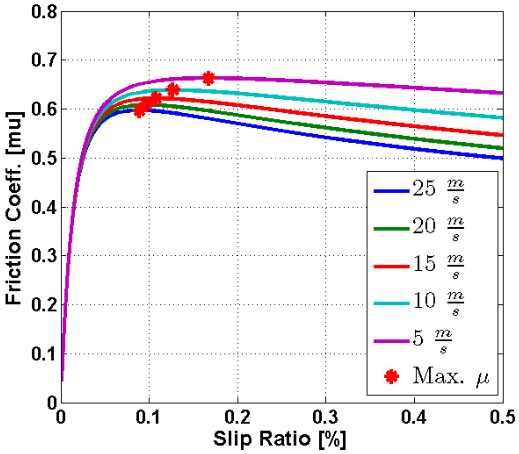

FIGURE 44: STEADY-STATE LUGRE FRICTION CURVE

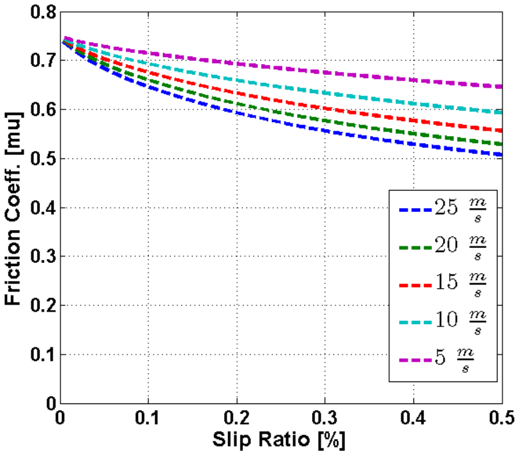

FIGURE 45: STRIBECK CURVE AT VARIOUS VELOCITIES

Then, recognizing that $\widehat{\omega}_r$ and $\hat{\theta}_r$ are only estimated states, Equation (16) can be rewritten as:

$$J_r * \frac{d\widehat{\omega}_r}{dt} = F_t R_r - \widehat{K}_t\left(\hat{\theta}_r - \theta_w\right) - \hat{C}_t(\widehat{\omega}_r - \omega_w) \tag{42}$$

Combining (35) & (42) and utilizing the estimation error $\widetilde{T}$,

$$\frac{d\widehat{\omega}_r}{dt} = \frac{1}{J_r}\left[F_t R_r - \widetilde{\mathrm{T}} - \hat{J}_w * \frac{d\omega_w}{dt} - T_{b1}\right] \tag{43}$$

where $T_{b1}$ is the braking torque applied corresponding to the ring slip-tracking problem. Defining the tracking error dynamics as:

$$e = \widehat{\omega}_r - \hat{Y}_d \quad \Rightarrow \quad \dot{e} = \frac{d\widehat{\omega}_r}{dt} - \dot{\hat{Y}}_d \tag{44}$$

where, $\hat{Y}_d = \frac{V}{R} * \left(1 - \hat{\lambda}_m\right)$ is an estimated desired ring rotational velocity corresponding to the estimated desired slip ratio $\hat{\lambda}_m$. Choosing the following (partial) Lyapunov-like candidate:

$$V = \frac{1}{2}e^2$$

$$\dot{V} = e\left(\frac{1}{J_r}\left[F_tR_r - \widetilde{\mathrm{T}} - \hat{J}_w\frac{d\omega_w}{dt} - T_{b1}\right] - \dot{\hat{Y}}_d\right) \tag{45}$$

If we set the controller as:

$$T_{b1} = F_tR_r - \widetilde{\mathrm{T}} - \hat{J}_w * \frac{d\omega_w}{dt} - J_r\dot{\hat{Y}}_d + J_rc_1e \tag{46}$$

where, $c_1$ is a positive controller gain, then, $\dot{V} = -c_1e^2$ , which is negative semi-definite and ensures the convergence of the error $e$ to zero. This shall be used in the stability analysis of the next section.

While this controller will track the desired slip ratio and accounts for tire flexibilities, observations have shown that the low torsional damping of the tire can result in large initial oscillations of brake torque $T_{b1}$ in the presence of tire/tread parameter estimation errors. In order to address this issue, it has been found that a virtual torsional damper can be simulated through the controller. This virtual damper ($C_{add}$) can be thought of as added in series between the original torsional spring and the tire ring, as shown in Figure 46. By including this virtual damper the controller can effectively emulate a highly damped system. Note that this damper is not placed in series with the physical damper $C_t$ as this would only result in a further decrease in overall damping. The virtual damper can be systematically constructed into the controller using backstepping techniques and the certainty equivalence principle. Similar examples can be found in [53, 55]. Here, choosing the Lyapunov function candidate:

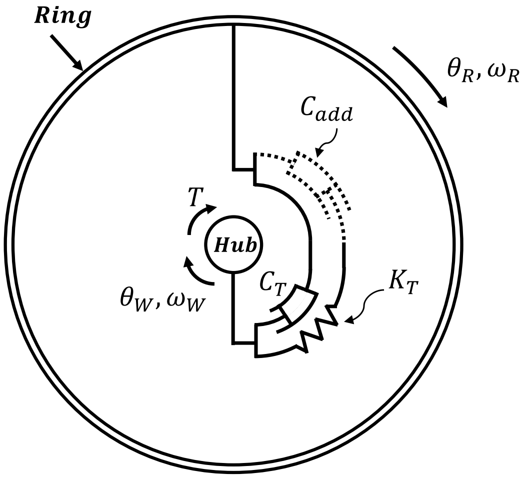

FIGURE 46: HUB/TIRE MODEL EMULATED BY CONTROLLER

$$V_1 = \frac{1}{2} J_r \omega_r^2 + \frac{1}{2} K_t (\theta_w - \theta_r)^2 \tag{47}$$

$$\begin{aligned} \dot{V}_1 = {} & J_r \omega_r \left( \frac{1}{J_r} [-K_t(\theta_r - \theta_w) - C_t(\omega_r - \omega_w)] \right) \\ & + K_t(\theta_w - \theta_r)(\omega_w - \omega_r) \end{aligned} \tag{48}$$

$$= \omega_r \big( C_t(\omega_w - \omega_r) \big) + K_t(\theta_w - \theta_r)\omega_w \tag{49}$$

Let the virtual control $\omega_w = -\omega_D$ in order to make the second term in Equation (49) negative semi-definite[8]. Where, $\omega_D$ represents the relative velocity of the virtual damper and follows the relation $\omega_D = \phi(T_D)$, where $T_D = K_t(\theta_w - \theta_r)$ is the force in the

---

[8] The first term in Equation (49) will be addressed in the following steps

damper[9] and $\phi(*)$ is a gain chosen by the designer and has the same sign as its argument[10]. The derivative of the relative velocity $\omega_D$ can be found through the following analysis:

$$\begin{aligned}\dot{\omega}_D &= \frac{d\phi(T_D)}{dt} = \frac{d\phi(T_D)}{dT_D} * \dot{T}_D \\ &= \frac{d\phi(T_D)}{dT_D} * \big(K_t(\omega_w - \omega_r)\big) \\ &= \zeta * (\omega_w - \omega_r)\end{aligned} \tag{50}$$

where, $\zeta = \frac{d\phi(T_D)}{dT_D} * K_t$ is chosen to be positive. Then, continuing with the backstepping procedure, the following change of variables can be applied:

$$\begin{aligned}\gamma &= \omega_w - (-\omega_D) = \omega_w + \omega_D \\ \dot{\gamma} &= \frac{1}{J_w}\left(K_t(\theta_r - \theta_w) + C_t(\omega_r - \omega_w) - T_{b2}\right) + \dot{\omega}_D\end{aligned} \tag{51}$$

Choosing the following Lyapunov candidate:

$$V_2 = \frac{1}{2}J_r\omega_r^2 + \frac{1}{2}K_t(\theta_w - \theta_r)^2 + \frac{1}{2}J_w\gamma^2 + \frac{1}{2}C_t\left(\frac{dT_D}{d\phi(T_D)}\frac{1}{K_t}\right)\omega_D^2 \tag{52}$$

$$\begin{aligned}\dot{V}_2 = {} & J_r\omega_r\dot{\omega}_r + K_t(\theta_w - \theta_r)(\gamma - \omega_D - \widehat{\omega}_r) + J_w\gamma\dot{\gamma} \\ & + \omega_D\big(C_t(\omega_w - \omega_r)\big)\end{aligned} \tag{53}$$

Combining Equations (51) and (53) and simplifying

---

[9] Since the spring and virtual damper are in series and massless, the force created in the virtual damper is equal to the force created in the physical spring.

[10] It is desirable to emulate a damper that dissipates energy from the system.

$$\dot{V}_2 = -\omega_D\big(K_t(\theta_w - \theta_r)\big) - C_t(\omega_w - \omega_r)^2 + \gamma(-T_{b2} + J_w\dot{\omega}_D) \tag{54}$$

Letting $T_{b2} = J_w\dot{\omega}_D$, Equation (54) becomes

$$\dot{V}_2 = -\omega_D\big(K_t(\theta_w - \theta_r)\big) - C_t(\omega_w - \omega_r)^2 \leq 0 \tag{55}$$

Then, utilizing Equation (50), $T_{b2}$ can be placed in its final form:

$$T_{b2} = \zeta * J_w(\omega_w - \omega_r) \tag{56}$$

Figure 47 shows the response of the system for various choices of $\zeta$ for a step input in brake torque. It is clear that as $\zeta$ is increased, the system's response is more representative of a well-damped system. Utilizing Equations (46) and (56) the final combined brake torque is represented as follows:

$$T_b = F_t R_r - \widetilde{\mathrm{T}} - \hat{J}_w * \frac{d\omega_w}{dt} - J_r\dot{\hat{Y}}_d - J_r c_1 e + \phi_D(\omega_w - \widehat{\omega}_r) \tag{57}$$

When this controller is combined with the parameter and state estimation of the previous section, the closed-loop system can be represented as was shown in Figure 43.

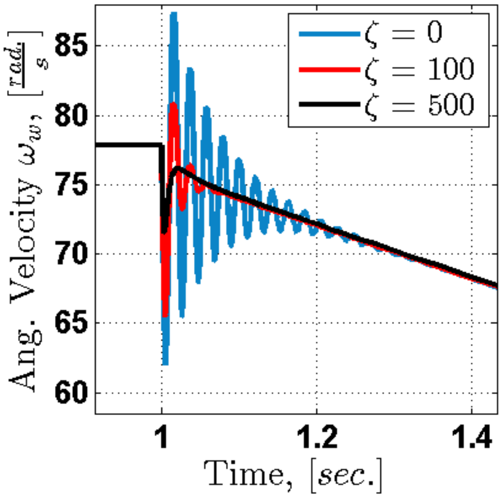

FIGURE 47: RESPONSE OF HUB/TIRE MODEL EMULATED BY CONTROLLER

## 5.3 STABILITY ANALYSIS

The stability of the closed-loop system, comprising of the parameter and state estimators and the controller tracking error, can be analyzed by choosing the following Lyapunov function candidate:

$$W = \frac{1}{2}\tilde{z}^2 + \frac{1}{2}\widetilde{\omega}_r{}^2 + \frac{1}{2}e^2 + \frac{1}{2}\tilde{\Sigma}_1{}^T\Gamma_1^{-1}\tilde{\Sigma}_1 + \frac{1}{2}\tilde{\Sigma}_2{}^T\Gamma_2^{-1}\tilde{\Sigma}_2 \Rightarrow$$

$$\begin{aligned}\dot{W} &= \tilde{z}\dot{\tilde{z}} + \widetilde{\omega}_r\dot{\widetilde{\omega}}_r + e\dot{e} + \tilde{\Sigma}_1{}^T\Gamma_1^{-1}\dot{\tilde{\Sigma}}_1 + \tilde{\Sigma}_2{}^T\Gamma_2^{-1}\dot{\tilde{\Sigma}}_2 \\ &= \tilde{z}\dot{\tilde{z}} + \widetilde{\omega}_r\dot{\widetilde{\omega}}_r + e\dot{e} - \tilde{\Sigma}_1{}^T\widehat{\mathrm{U}}_1\left[\widehat{U}_1\tilde{\Sigma}_1 + \widetilde{U}_1\Sigma_1\right] \\ &\qquad - \tilde{\Sigma}_2{}^T\widehat{\mathrm{U}}_2\left[\widehat{U}_2\tilde{\Sigma}_2 + \widetilde{U}_2\Sigma_2\right] \end{aligned} \tag{58}$$

where, $\widetilde{U}_1 = \widetilde{U}_{11}\widetilde{\omega}_r + \widetilde{U}_{12}\tilde{z}$ and $\widetilde{U}_2 = \widetilde{U}_{21}\tilde{\theta}_r + \widetilde{U}_{22}\widetilde{\omega}_r$. This leads to:

$$\begin{aligned}\widetilde{U}_{11} &= [0 \quad -R_r(1 - kh'(\omega_r)\hat{z}) \quad f'(V_r)\, R_r\hat{z}] \\ \widetilde{U}_{12} &= [1 \quad k|\omega_r|R_r \quad -f(V_r)]\end{aligned} \tag{59}$$

$$\begin{aligned}\widetilde{U}_{21} &= [1 \quad 0 \quad 0] \\ \widetilde{U}_{22} &= [0 \quad 1 \quad 0]\end{aligned} \tag{60}$$

where,

$$f'(V_r) = \frac{df(V_r)}{dV_r} = \frac{1}{\tilde{V}_r}\left[f(V_r) - f\left(\hat{V}_r\right)\right] = \frac{-1}{\widetilde{\omega}_r R_r}\left[f(V_r) - f\left(\hat{V}_r\right)\right] \tag{61}$$

and

$$h(\omega_r) = |\omega_\mathrm{r}| \;\Rightarrow\; h'(V_r) = \frac{dh(\omega_r)}{d\omega_r} = \frac{1}{\widetilde{\omega}_r}[h(\omega_r) - h(\widehat{\omega}_r)] \tag{62}$$

$\dot{\tilde{z}}$ is computed as follows:

$$\begin{aligned}\dot{\tilde{z}} &= V_r - K_{tread} f(V_r) z - k|\omega_r| R_r z \\ &\quad - \left[V_r - \widehat{K}_{tread} f(V_r)\hat{z} - k|\widehat{\omega}_r| R_r \hat{z}\right]\end{aligned}$$

$$\begin{aligned}\xrightarrow{yields}\; \dot{\tilde{z}} &= -\widetilde{\omega}_r R_r [1 - K_{tread} f'(V_r)\hat{z} + k h'(\omega_r)\hat{z}\,] \\ &\quad - \tilde{z}[K_{tread}\, f(V_r) + k R_r h(\omega_r)] \\ &= -\widetilde{\omega}_r A - \tilde{z} B\end{aligned} \tag{63}$$

And $\dot{\tilde{\omega}}_r$ is computed as follows:

$$\begin{aligned}\dot{\tilde{\omega}}_r &= \frac{1}{J_r}[F_t R_r - K_t(\theta_\mathrm{r} - \theta_\mathrm{w}) - C_t(\omega_\mathrm{r} - \omega_\mathrm{w})] \\ &\quad - \frac{1}{J_r}\left[F_t R_r - \widehat{K}_t\left(\hat{\theta}_\mathrm{r} - \theta_\mathrm{w}\right) - \hat{C}_t(\widehat{\omega}_\mathrm{r} - \omega_\mathrm{w})\right]\end{aligned}$$

$$\xrightarrow{yields}\; \dot{\tilde{\omega}}_r = \frac{1}{J_r}\left[-\widetilde{K}_t(\theta_\mathrm{r} - \theta_\mathrm{w}) - \tilde{C}_t(\omega_\mathrm{r} - \omega_\mathrm{w}) - \widehat{K}_t\tilde{\theta}_\mathrm{r} - \hat{C}_t\widetilde{\omega}_\mathrm{r}\right] \tag{64}$$

Utilizing Equations (59) through (64), Equation (58) can be rewritten in quadratic form as follows:

$$\dot{W} = -[\tilde{\Sigma}_1 \quad \tilde{\Sigma}_2 \quad \tilde{z} \quad \tilde{\theta}_r \quad \widetilde{\omega}_r \;\; e][M]\begin{bmatrix}\tilde{\Sigma}_1 \\ \tilde{\Sigma}_2 \\ \tilde{z} \\ \tilde{\theta}_r \\ \widetilde{\omega}_r \\ e\end{bmatrix} = -\phi^T M \phi \tag{65}$$

where, $\phi = [\tilde{\Sigma}_1 \quad \tilde{\Sigma}_2 \quad \tilde{z} \quad \tilde{\theta}_r \quad \widetilde{\omega}_r \;\; e]$, and

$$M = \begin{bmatrix} \widehat{U}_1^T \widehat{U}_1 & 0 & \widehat{U}_1^T U_{12} \Sigma_1 & 0 & \widehat{U}_1^T U_{11} \Sigma_1 & 0 \\ 0 & \widehat{U}_2^T \widehat{U}_2 & 0 & \widehat{U}_2^T U_{21} \Sigma_2 & \widehat{U}_2^T U_{22} \Sigma_2 & 0 \\ 0 & 0 & B & 0 & A & 0 \\ 0 & 0 & 0 & 1 & 0 & 0 \\ 0 & C & 0 & \dfrac{\widehat{K}_T}{J_r} & \dfrac{\hat{C}_T}{J_r} & 0 \\ 0 & 0 & 0 & 0 & 0 & c_1 \end{bmatrix} \tag{66}$$

where,

$$\mathrm{C} = \begin{bmatrix} \dfrac{1}{\mathrm{J_r}}(\theta_\mathrm{r} - \theta_\mathrm{w}) & \dfrac{1}{\mathrm{J_r}}(\omega_\mathrm{r} - \omega_\mathrm{w}) & 0 \end{bmatrix}$$

$M$ can be decomposed into a symmetric matrix $M_1 = (M + M^T)/2$, and a skew-symmetric matrix $M_2 = (M - M^T)/2$. For a real matrix $M$, we have: $-\phi^T M_2 \phi \ = 0$ due to the properties of a skew-symmetric matrix. And it can be shown, for the matrix $M$ given by Equation (66), that the principal minors of $M_1$ are all non-negative, and therefore, $M_1$ is positive semi-definite [56]. Thus,

$$\dot{W} = -\phi^T M_1 \phi \ \leq 0 \tag{67}$$

Thus the equilibrium point $[\tilde{\Sigma}_1 \quad \tilde{\Sigma}_2 \quad \tilde{z} \quad \tilde{\theta}_r \quad \widetilde{\omega}_r \ e] = 0$ is stable and the corresponding estimation and tracking errors are bounded. Using Barbalat's Lemma it can be shown that $\lim_{t \to \infty} e = 0$. However, for guaranteed parameter and state convergence the states are required to be persistently excited.

## 5.4 RESULTS AND DISCUSSIONS

This section tests the closed-loop system presented in this chapter through both simulations and experimental results. Emergency braking tests are simulated for a quarter-car model of a small passenger vehicle (1068 Kg) with an initial velocity of 80kph, and the low torsional stiffness tire. The vehicle begins the braking event at t = 0.5sec.

In order to establish a baseline, it is sought to evaluate the performance of the traction controller when the controller assumes that the tire sidewall is rigid. This is completed by slightly modifying the controller proposed in [23] to use the Average Lumped Parameter LuGre friction model and coupling it with the low torsional stiffness tire. The derivations for this slightly modified controller can be found in Appendix D. The results of these simulation tests are shown in Figure 48 & Figure 49 highlight the difficulty the controller has in preventing initial oscillations in the ring velocity. While the adaptation laws still perform very well in the presence of the un-modeled dynamics, the brake torque and subsequently the ring angular velocity are very oscillatory upon initial brake application. These unmodeled dynamics also cause large oscillations in the brake torque and angular velocities later in the event due to the challenges of maintaining a desired slip

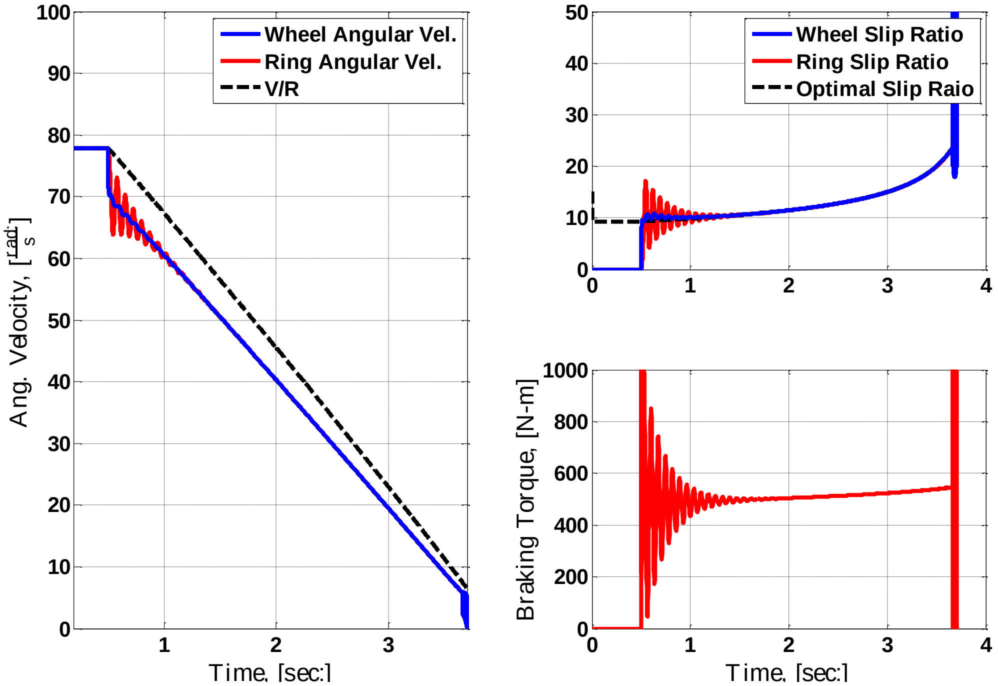

FIGURE 48: BRAKING RESPONSE FOR "RIGID TIRE" BASED ADAPTIVE NONLINEAR CONTROLLER

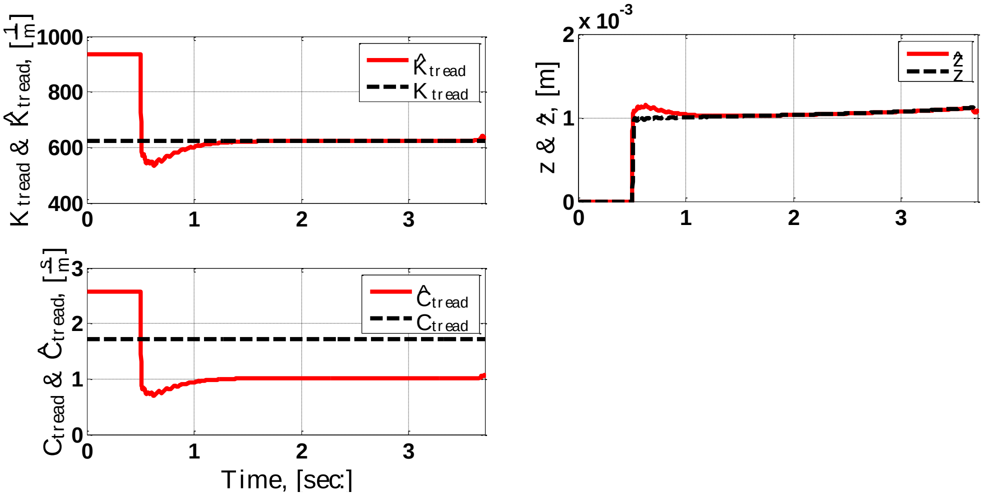

FIGURE 49: PARAMETRIC ESTIMATIONS & ERRORS FOR "RIGID TIRE" BASED ADAPTIVE NONLINEAR CONTROLLER

ratio at low velocities. It should also be noted that there is an increase in the optimal slip ratio as velocity decreases. This trend is consistent with the LuGre model as the peak friction coefficient will not occur at a fixed slip ratio.

Figure 50 & Figure 51 show the system response for the adaptive controller proposed in this chapter. The system parameters & estimated states are assumed to be unknown prior to the event. In reality, it is likely that the adaptation laws have been enabled prior to the hard braking event, thus allowing for a more precise estimate of the system parameters and states. However, by assuming that the parameters and states are unknown prior to the event, a dramatic variation in the system parameters can be represented. Initial estimates of the tire's torsional properties are assumed to be on the order of a standard tire. These initial parameters are chosen to highlight the most challenging case when an initial

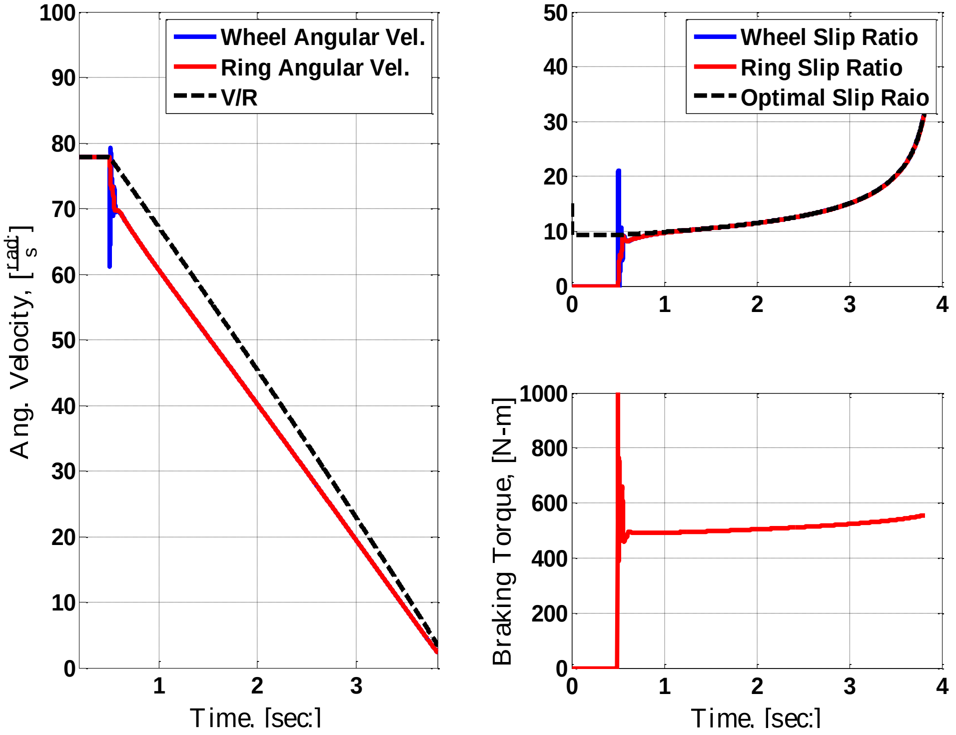

FIGURE 50: BRAKING RESPONSE FOR ADAPTIVE NONLINEAR CONTROLLER (UNKNOWN PARAMETERS)

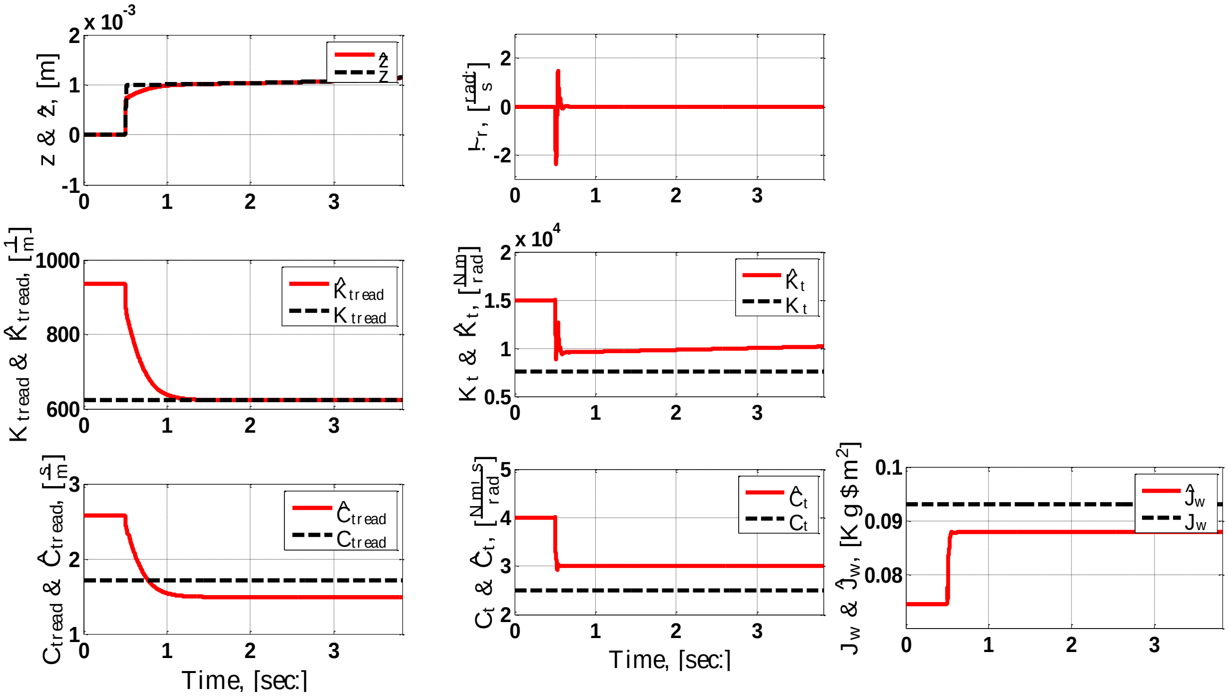

FIGURE 51: PARAMETRIC ESTIMATIONS & ERRORS FOR ADAPTIVE NONLINEAR CONTROLLER (UNKNOWN PARAMETERS)

estimated tire is significantly stiffer than the actual tire. An example of this scenario may be when there is a sudden loss in tire pressure or immediately following the installation of a new set of low-torsional stiffness tires.

Figure 51 shows the parameter and state estimations for the braking event. The estimated states errors $\tilde{z}$ and $\widetilde{\omega}_r$ as well as the estimated tread parameter $K_{tread}$ quickly converge to zero. The remainder of the parameter estimates also begins to converge towards their actual values. However, due to the lack of persistent excitation these parameter estimates are unable to completely converge. This issue is a common problem in adaptive control as the persistence of excitation decreases with an increase in controller performance when the reference trajectory by itself is unable to sufficiently excite the states.

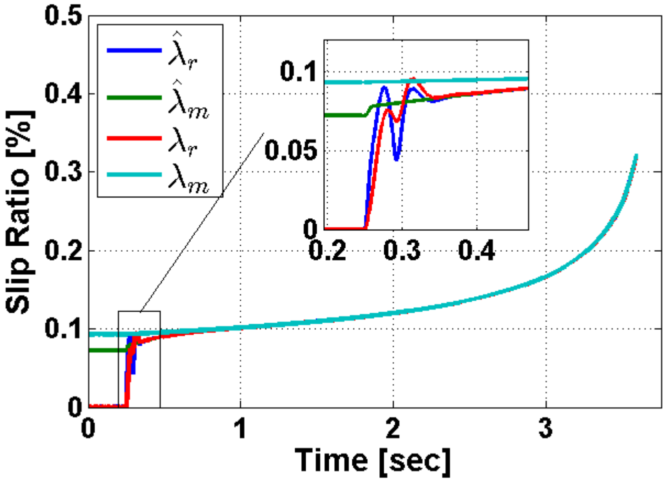

FIGURE 53: SLIP TRACKING RESPONSE -- ADAPTIVE NONLINEAR CONTROLLER

Figure 50 shows the angular velocity trajectories and braking torque for this maneuver. It is important to note that the wheel slip ratio will initially overshoot the optimal slip ratio. This is a desirable response as wheel slip ratio does not appear in the tracking error dynamics (Equation (44)) and the controller is taking advantage of the sidewall

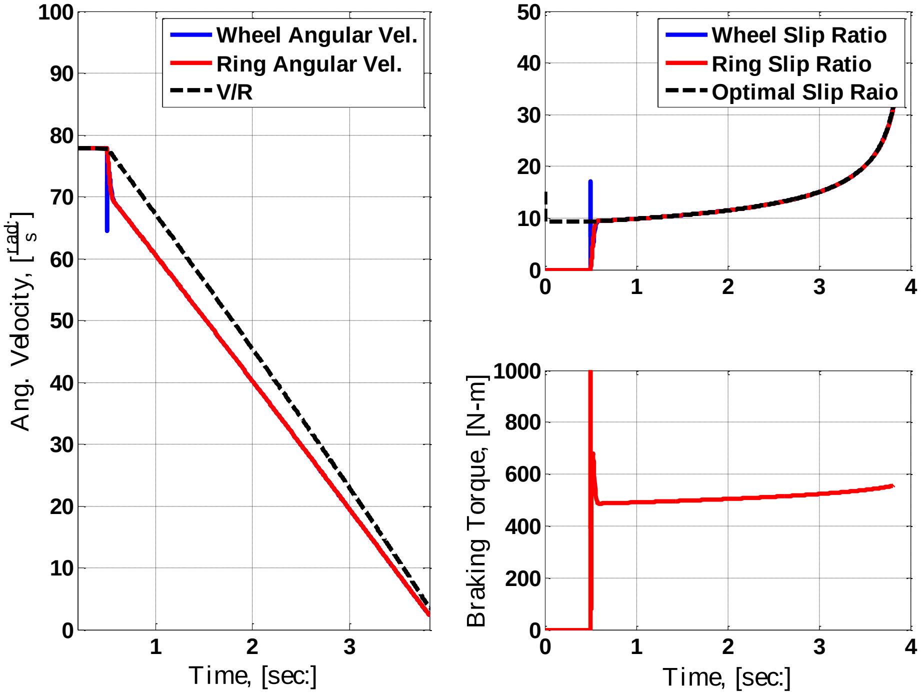

FIGURE 52: BRAKING RESPONSE FOR ADAPTIVE NONLINEAR CONTROLLER (KNOWN TIRE SIDEWALL PARAMETERS)

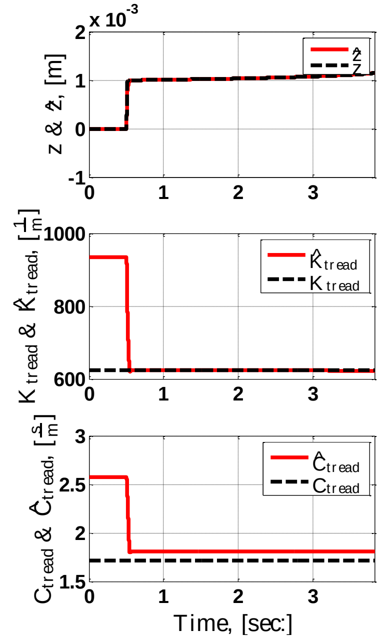

FIGURE 54: PARAMETRIC ESTIMATIONS FOR ADAPTIVE NONLINEAR CONTROLLER (KNOWN TIRE SIDEWALL PARAMETERS)

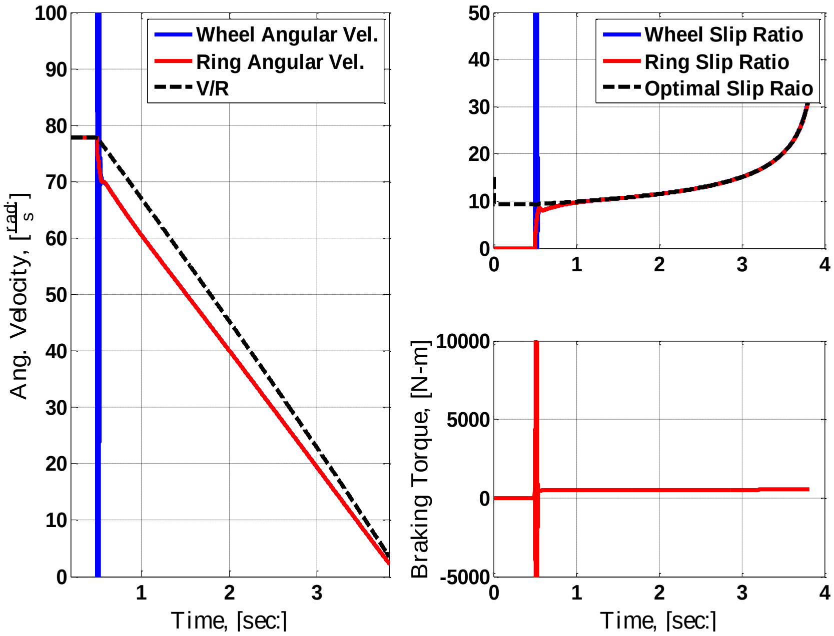

FIGURE 55: BRAKING RESPONSE FOR ADAPTIVE NONLINEAR CONTROLLER (UNKNOWN PARAMETERS & NO VIRTUAL DAMPER)

flexibility in order to build up the ring slip ratio as quickly as possible. Figure 53 shows the system slip ratio tracking response, where $\hat{\lambda}_r$ and $\hat{\lambda}_m$ are the estimated ring and optimal

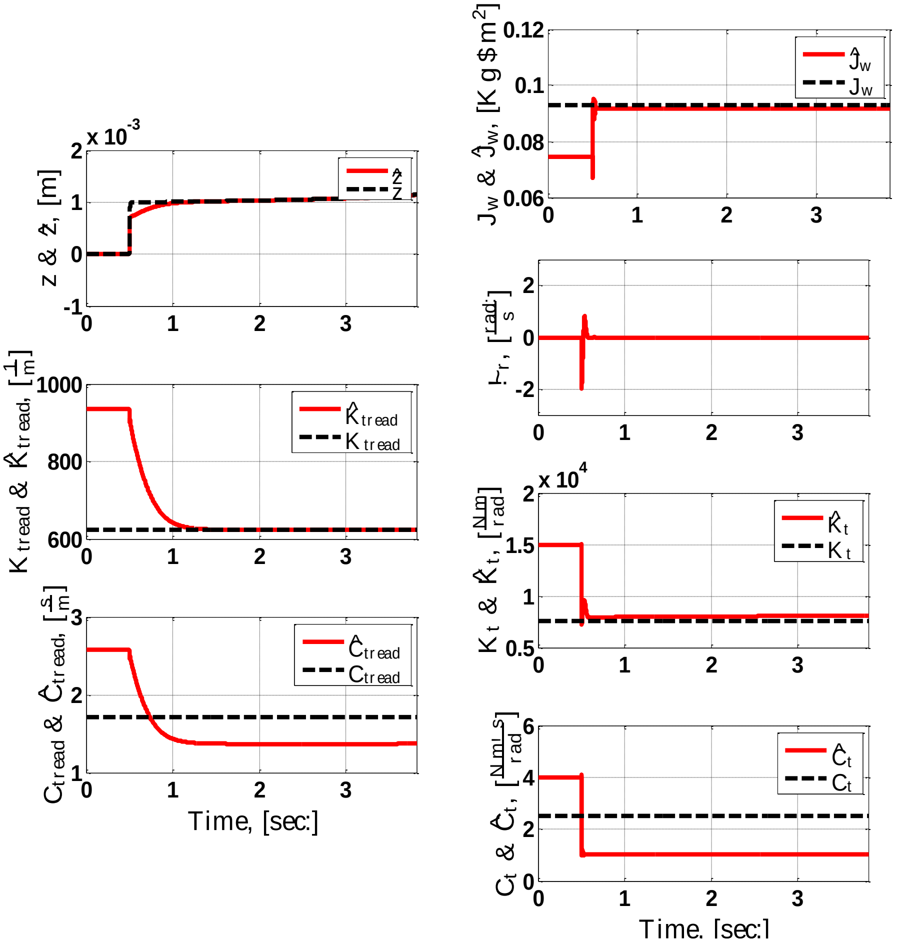

FIGURE 56: PARAMETRIC ESTIMATIONS & ERRORS FOR ADAPTIVE NONLINEAR CONTROLLER (UNKNOWN PARAMETERS & NO VIRTUAL DAMPER)

slip ratios, respectively and $\lambda_r$ and $\lambda_m$ represent the actual ring and optimal slip ratios. This figure shows that the response of the actual ring angular velocities is actually less oscillatory than the estimated ring velocity. This is due to the inclusion of the estimation error $\tilde{T}$ in the controller design, which helps the controller compensate for errors in the state estimations. The plot further shows how the desired slip ratio converges to the optimal slip ratio within the first 0.5 seconds. While all of the estimated parameters are converging towards their true value, some of the parameters were unable to completely converge within a single braking event. As stated earlier, convergence of the parameters within a single braking event proves to be a very challenging task as the level of state excitation decreases as controller performance increases.

Figure 52 & Figure 54 illustrate the system response when the sidewall parameters are known but the tread parameters remain unknown. The tread parameters are able to very quickly converge to their true values. The angular velocity responses, shown in Figure 52, also show a very smooth response with almost no oscillations in the ring angular velocity.

Finally, Figure 55 & Figure 56 show the response of the system when the added virtual damper $C_{add}$ is not emulated through the controller. Although the controller is still very successful at tracking the desired ring slip ratio, the braking torque, shown in Figure 55, is very oscillatory and reaches very large positive and negative values. These dramatic oscillations cause the wheel angular velocity $\omega_w$ to be oscillatory and even reach negative values. These responses are not realistic, due to limits on the brake actuator, and are not desirable. Therefore, to better account for the tire's low torsional damping, it is useful to include a virtual damper through the controller in order to emulate a well-damped system.

In addition to the simulation-based results, the nonlinear controller was implemented experimentally by using the electromechanical brake test fixture discussed earlier. Figure 57 shows the experimental response of the system with no parameter adaptation and assuming that the system represents the high torsional stiffness tire, instead of the actual low torsional stiffness tire. The response of the system follows the optimal slip ratio reasonably well and the dyno velocity reaches zero within 4 seconds and 53

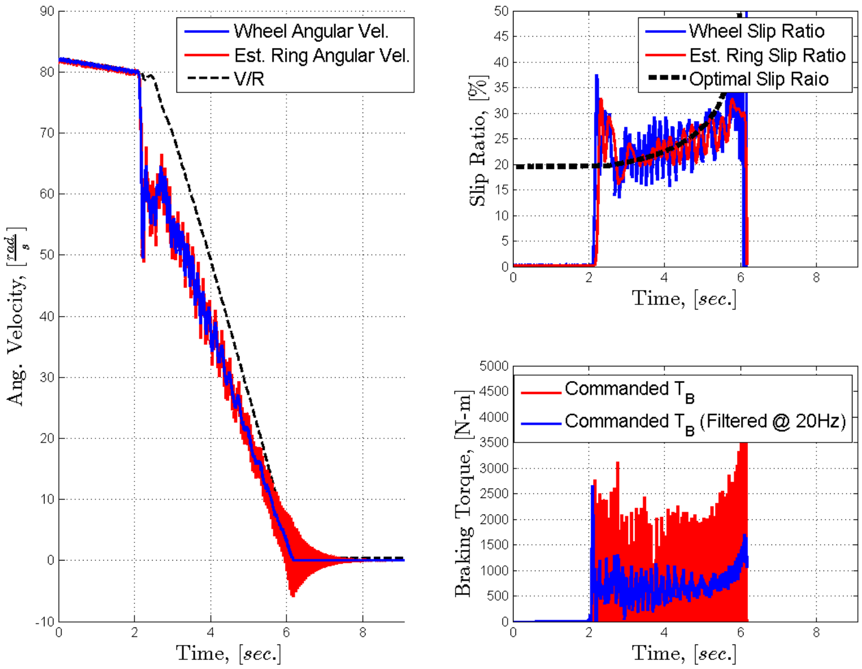

FIGURE 57: EXPERIMENTAL BRAKING RESPONSE FOR NONLINEAR CONTROLLER (UNKNOWN PARAMETERS & NO ADAPTATION)

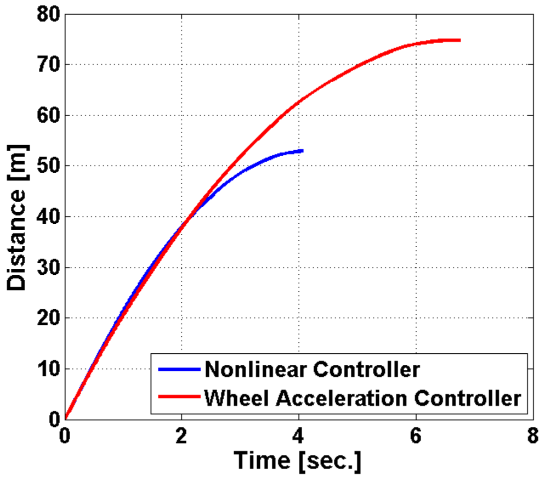

FIGURE 58: EXPERIMENTAL BRAKING DISTANCE COMPARISON

meters; quicker than the 6.75 seconds and approximately 75 meters required for the tuned peripheral wheel acceleration controller at an equivalent load, as shown in Figure 58.

While these results show that the controller is able to maintain a high level of friction force throughout the event, the response is considerably more oscillatory than what is seen in the simulations and the commanded brake torque appears to have significant chatter. It should be noted that the commanded brake torque is shown in both in an unfiltered and 20Hz filtered state, as the filtered signal is more representative of the brake torque actually applied to the wheel after accounting for the actuator's bandwidth.

One of the main sources for disturbances in the experimental system is related to a 1st harmonic disturbance in friction force. It is assumed that this disturbance is caused by either the warping of the brake disc rotor due to the repeated emergency braking events, or the non-uniformity of the tire in conjunction with a fixed suspension height (thus resulting in a change in Fz). Figure 59 shows an example of this disturbance by comparing a step command in the brake torque signal, which for the purposes of this discussion has been converted to an estimated friction force, with the measured friction force on the rolling tire (note that this is not an ABS event, but is instead a diagnostic test where the control signal

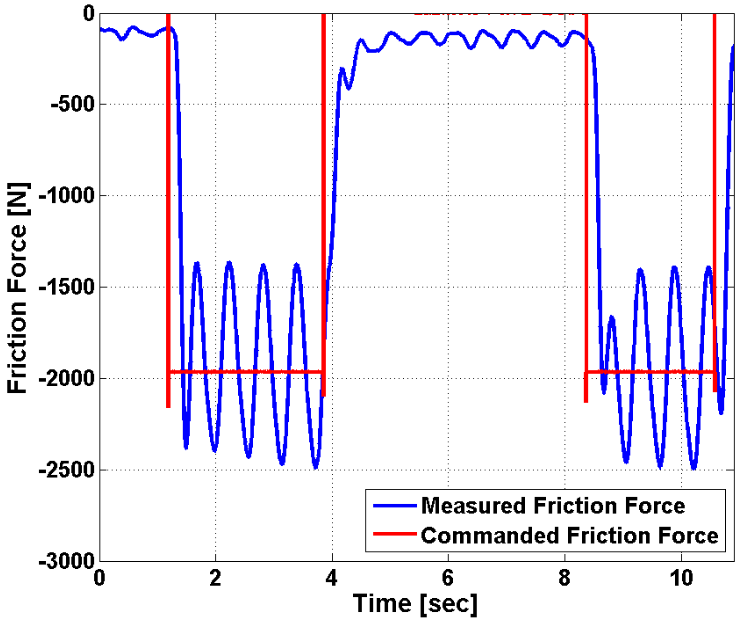

FIGURE 59: EXPERIMENTAL DISTURBANCE IN FRICTION FORCE

is manually controlled). When the commanded friction force is held around -2000N, there is an approximate 1000N peak-to-peak oscillation in measured friction force due to the warped brake rotor. Experimental tests also show that the peak-to-peak magnitude of these oscillations is approximately equal to 50% of the nominal friction force.

Given the magnitude of this disturbance, it is understandable the controller experienced some oscillations and chatter in the control signal. It also demonstrates the robustness of the controller to these large disturbances in brake torque while still having a significant improvement in braking efficiency over the peripheral wheel acceleration controller. One reason the controller was able to perform reasonably in the presence of the disturbances was due to the inclusion of the virtual damper. Throughout the experimental tests the virtual damper became a vital tuning parameter of the controller and was able to have a significant effect on the performance of the controller in the presence of this disturbance. The virtual damper effectively penalized the oscillations between the angular velocities $\omega_w$ & $\omega_r$ and attempted to produce a system response similar to that of a well-damped tire.

Also, due to the disturbances the parameter adaptation scheme was not able to be successfully introduced into the experimental tests. Upon attempts to incorporate the adaptation laws, the disturbances in the measured friction force caused the system to appear as if it was reacting to small changes in brake torque, thus resulting in the system's estimated stiffness parameters becoming divergent. If further work was completed towards possible methods of directly measuring the brake torque, it is possible that these measurements could not only be included in the observers, but also compensated for through the controller.

In order to verify the response of the closed-loop system to a disturbance in brake torque, a simulation test was run when a 1st harmonic disturbance of both 5% and 50% peak-to-peak magnitude is imposed on the brake torque with no parameter adaptation, assuming known tread parameters and unknown sidewall parameters. Figure 60 & Figure 61 show the responses of the system to a 5% and 50% disturbance; and in concurrence with the experimental results, the simulation results show a significant amount of oscillations in the system response. Furthermore, simulations were conducted including parametric

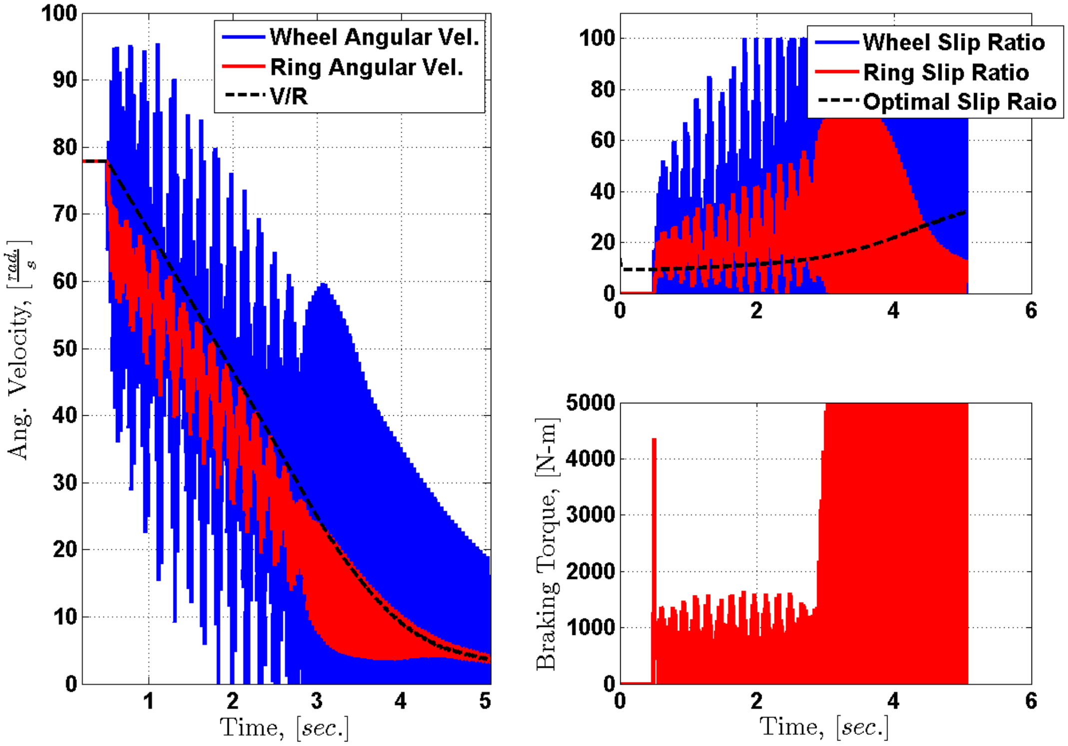

FIGURE 60: SIMULATION BRAKING RESPONSE (WITH 5% PEAK-TO-PEAK DISTURBANCE IN TB)

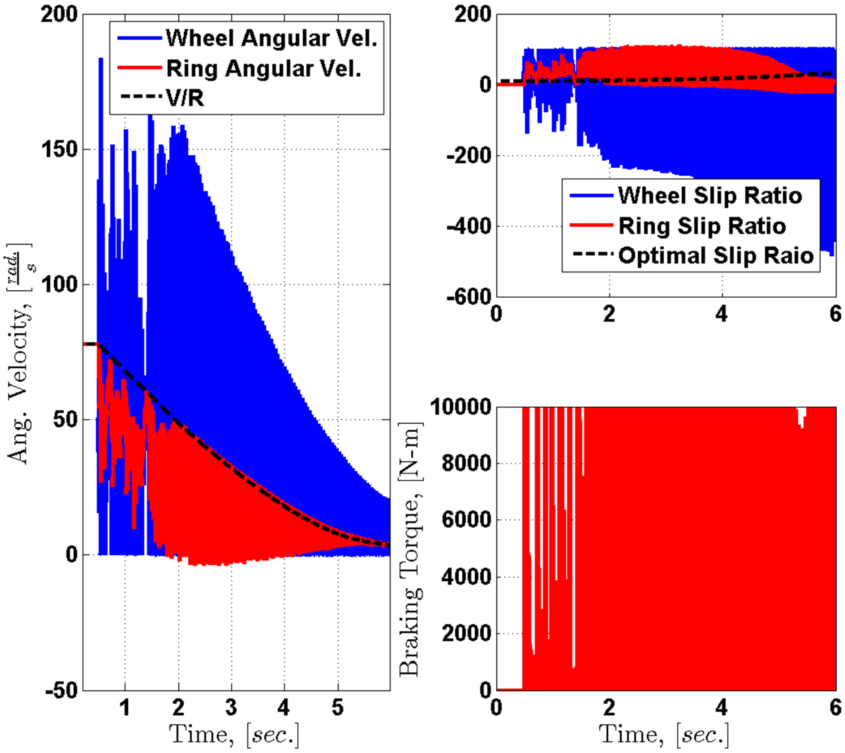

FIGURE 61: SIMULATION BRAKING RESPONSE (WITH 50% PEAK-TO-PEAK DISTURBANCE IN TB)

adaptation and verified that, under the large 50% peak-to-peak disturbance in brake torque, the stiffness parameters were indeed divergent. These results can be seen in Figure 62 & Figure 63.

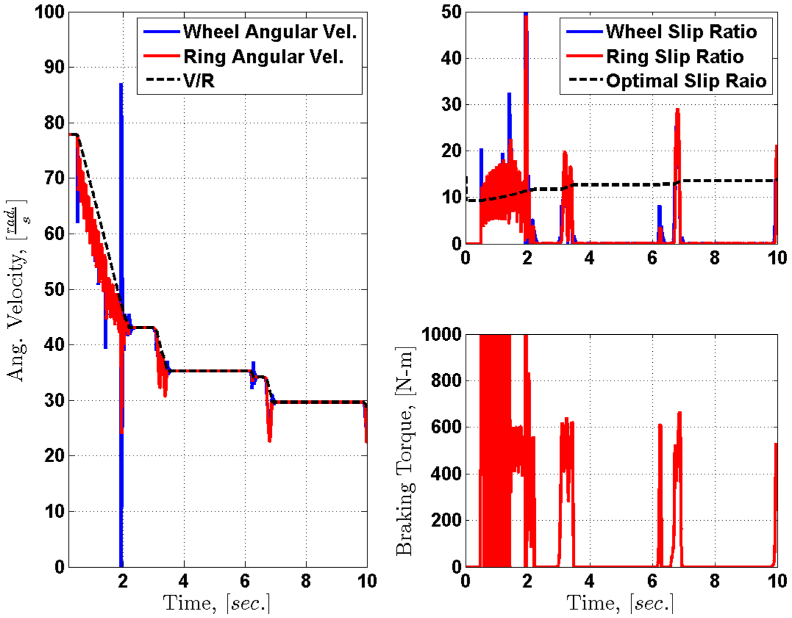

FIGURE 62: SIMULATION BRAKING RESPONSE (WITH 50% PEAK-TO-PEAK DISTURBANCE IN TB AND PARAMETER ADAPTATION)

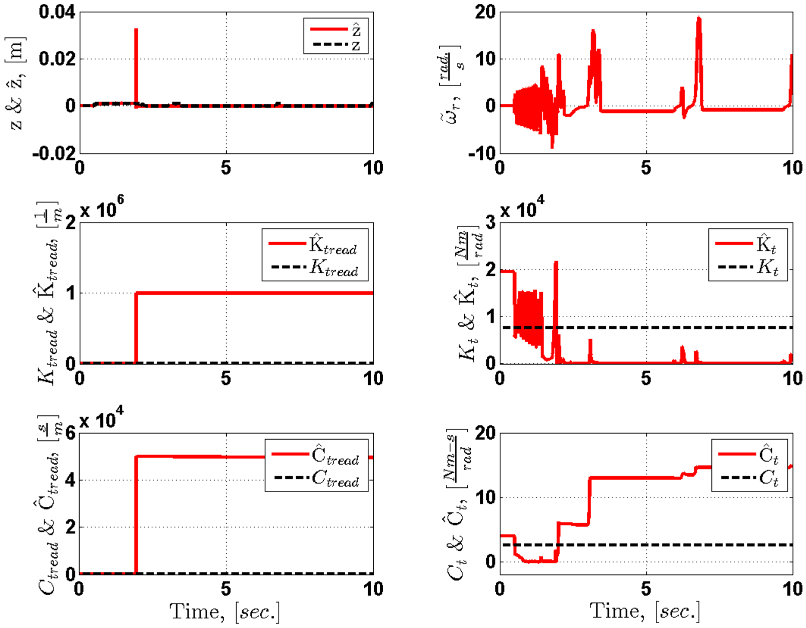

FIGURE 63: PARAMETRIC ESTIMATIONS & ERRORS FOR ADAPTIVE NONLINEAR CONTROLLER (WITH 50% PEAK-TO-PEAK DISTURBANCE IN TB AND PARAMETER ADAPTATION)

## 5.5 CHAPTER SUMMARY

In this chapter an adaptive controller was proposed that estimates both the tire sidewall and tread parameters & states using a dynamic friction/tread model and a torsionally flexible tire model. The scheme assumes that the vehicle longitudinal velocity, traction force at the ground, wheel speed, and brake torque are measureable. The controller was designed to account for the tire's sidewall flexibility, to track the optimal slip ratio, and included a virtual damper in order to emulate a highly damped system. Closed-loop stability analysis was performed using Lyapunov functions to prove boundedness of the parameter and state errors as well as the controller tracking error. Simulation results showed that the controller was able to successfully track the desired slip ratio even when the initial parameters are assumed to be unknown. When the sidewall parameters are known but the tread parameters are not, the adaptive controller scheme showed very quick convergence of the tread parameters and states and was able to track the optimal slip ratio with minimal control effort.

Experimental tests were also completed using only the nonlinear controller with no parameter adaptation. Results showed that the controller was able to track the desired slip ratio reasonably well even when significant disturbances were present. The author was unable to successfully include the parameter adaptation scheme into the experimental tests due to the disturbances which would drive the system's stiffness parameters to zero. The disturbances, if caused by changes in the normal load, are partially due to the fixture's fixed suspension height. Further work could be completed to replace the fixture’s turnbuckle with a strut and redesign the EMB to allow it to “float” with the wheel carrier. The current EMB system could also possibly be replaced with a more direct connection. Additional observers and adaptation techniques can also be included to eliminate the requirements of longitudinal velocity or friction force measurements and prior knowledge of the friction function.

# CHAPTER 6: ADAPTIVE SLIDING MODE CONTROLLER

As discussed in Chapter 2 and Chapter 5, the adaptive traction controller has limitations regarding robustness in the absence of persistent excitation and is difficult to guarantee closed-loop transient performance. These issues can be addressed by utilizing the modularity of the closed-loop system to replace the nonlinear controller from Chapter 5 with a sliding mode controller, which is more robust to model uncertainties and can be designed to meet certain performance requirements. When this controller is combined with the parameter and state estimation of the previous section, the closed-loop system is represented as shown in Figure 64. It should be noted that while the parameter adaptation scheme may not be required to achieve robust stability when using the sliding mode controller, it can be used to increase the systems robust performance as the estimated plant parameters approach their true values.

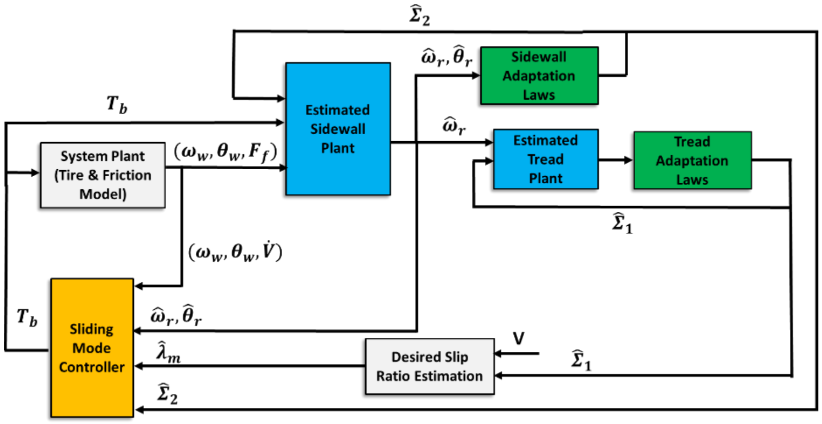

FIGURE 64: SCHEMATIC OF PROPOSED ADAPTIVE SLIDING MODE CONTROLLER SCHEME

The derivations of a sliding-mode controller based on the rigid-ring flexible sidewall model are presented in the following.

## 6.1 CONTROLLER DERIVATION

Placing the sidewall dynamics in state-space form

$$\begin{bmatrix}\omega_w\\ \dot{\omega}_w\\ \omega_r\\ \dot{\omega}_r\end{bmatrix} = \begin{bmatrix} 0 & 1 & 0 & 0\\ -\frac{K_t}{J_w} & -\frac{C_t}{J_w} & \frac{K_t}{J_w} & \frac{C_t}{J_w}\\ 0 & 0 & 0 & 1\\ \frac{K_t}{J_r} & \frac{C_t}{J_r} & -\frac{K_t}{J_r} & -\frac{C_t}{J_r}\end{bmatrix}\begin{Bmatrix}\theta_w\\ \omega_w\\ \theta_r\\ \omega_r\end{Bmatrix} + \begin{bmatrix}0\\ -\frac{1}{J_w}\\ 0\\ 0\end{bmatrix}T_b + \begin{bmatrix}0\\ 0\\ 0\\ \frac{R}{J_r}\end{bmatrix}F_t \tag{68}$$

And defining the sliding mode surface as:

$$\mathrm{s} = \mathrm{c}_1(\omega_\mathrm{r} - \omega_w) + c_2(\omega_r - \omega_d) \tag{69}$$

where, the sliding motion occurs when the ring angular velocity $\omega_r$ reaches the sliding subspace/surface $\mathrm{s} = 0$ at the desired angular velocity $\omega_d = \frac{V}{R}(1 - \lambda_m)$. The term $\mathrm{c}_1(\omega_\mathrm{r} - \omega_w)$ is included to penalize excessive oscillations in torsional dynamics, and will approach zero under quasi-steady state conditions. An equivalent control law can be found differentiating $s(x, \omega_d)$ with respect to time along the system trajectory, where x is the state vector in (68):

$$\begin{aligned}\dot{s}(x,\omega_d) &= \frac{\partial s}{\partial x}A(x) + \frac{\partial s}{\partial x}B(x)u - c_2\dot{\omega}_d \\ &= [0\ \ -c_1\ 0\ (c_1+c_2)]\begin{bmatrix} 0 & 1 & 0 & 0 \\ -\dfrac{K_t}{J_w} & -\dfrac{C_t}{J_w} & \dfrac{K_t}{J_w} & \dfrac{C_t}{J_w} \\ 0 & 0 & 0 & 1 \\ \dfrac{K_t}{J_r} & \dfrac{C_t}{J_r} & -\dfrac{K_t}{J_r} & -\dfrac{C_t}{J_r} \end{bmatrix}\begin{Bmatrix} \theta_w \\ \omega_w \\ \theta_r \\ \omega_r \end{Bmatrix} \\ &\quad + [0\ \ -c_1\ 0\ (c_1+c_2)]\begin{bmatrix} 0 \\ -\dfrac{1}{J_w} \\ 0 \\ 0 \end{bmatrix} T_b - c_2\dot{\omega}_d \end{aligned} \tag{70}$$

The nominal control input $T_{bn}$ required to keep the state trajectories on the sliding surface $s(x,\omega_d) = 0$ can then be solved by setting Equation (70) to zero.

$$\begin{aligned} T_{bn} &= -\left(\frac{\partial s}{\partial x}B(x)\right)^{-1}\frac{\partial s}{\partial x}(A(x) - c_2\dot{\omega}_d) \\ &= \left([0\ \ -c_1\ 0\ (c_1+c_2)]\begin{bmatrix} 0 \\ -\dfrac{1}{J_w} \\ 0 \\ 0 \end{bmatrix}\right)^{-1}\left([0\ \ -c_1\ 0\ (c_1+c_2)]\begin{bmatrix} 0 & 1 & 0 & 0 \\ -\dfrac{K_t}{J_w} & -\dfrac{C_t}{J_w} & \dfrac{K_t}{J_w} & \dfrac{C_t}{J_w} \\ 0 & 0 & 0 & 1 \\ \dfrac{K_t}{J_r} & \dfrac{C_t}{J_r} & -\dfrac{K_t}{J_r} & -\dfrac{C_t}{J_r} \end{bmatrix}\begin{Bmatrix} \theta_w \\ \omega_w \\ \theta_r \\ \omega_r \end{Bmatrix}\right) \\ &= K_t\left(1 + \frac{J_w}{J_r}\frac{c_1+c_2}{c_1}\right)(\theta_r - \theta_w) + C_t\left(1 + \frac{J_w}{J_r}\frac{c_1+c_2}{c_1}\right)(\omega_r - \omega_w) + c_2\dot{\omega}_d\frac{J_w}{c_1} \end{aligned} \tag{71}$$

When the system states are not on the sliding surface an additional corrective braking torque $T_{bc}$ must be added to the nominal braking torque $T_{bn}$. This braking torque is determined from the following reaching condition:

$$s\dot{s} \leq -\eta|s| \tag{72}$$

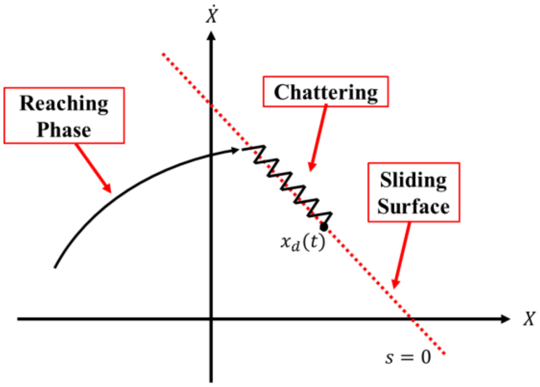

FIGURE 65: SLIDING MODE CONTROL CHATTERING

where, η is a strictly positive gain. Combining Equation (70) and (72), it can be shown that the corrective braking torque is

$$\mathrm{T_{bc}} \leq \frac{-\eta\, \mathrm{J_w}}{\mathrm{c_1}} sgn(s) \tag{73}$$

Combining Equations (71) and (73) the final combined brake torque is represented as follows:

$$\begin{aligned} T_b &= T_{bn} + T_{bc} \\ &= K_t\left(1 + \frac{J_w}{J_r}\frac{c_1 + c_2}{c_1}\right)(\theta_r - \theta_w) + C_t\left(1 + \frac{J_w}{J_r}\frac{c_1 + c_2}{c_1}\right)(\omega_r - \omega_w) \\ &\qquad + c_2\dot{\omega}_d\frac{J_w}{c_1} - \frac{-\eta\, \mathrm{J_w}}{\mathrm{c_1}} sgn(s) \end{aligned} \tag{74}$$

It is well known that in practice sliding mode controllers tend to exhibit chattering. This is caused due to the discontinuous nature of the control law across the sliding surface (Figure 65).

While this discontinuity is beneficial for accommodating model uncertainties, noise, and disturbances, the control switches in practice are not are not perfect or immediate. This results in controller chattering which may excite high-frequency dynamics and result in degraded performance. One method that is frequently used to address this issue is to include a boundary layer around the sliding surface that allows the reaching function to have a smooth transition from full control actuation (e.g. sgn(s) ) to zero. This can be implemented by replacing $\mathrm{sgn}(\mathrm{s})$ with the boundary layer condition $\mathrm{f(s)} = \frac{\mathrm{s}}{|\mathrm{s}|+\delta}$, where $\delta > 0$. Utilizing this technique, the resultant control law can be expressed as:

$$\begin{aligned} T_b = {} & K_t\left(1+\frac{J_w}{J_r}\frac{c_1+c_2}{c_1}\right)(\theta_r-\theta_w)+C_t\left(1+\frac{J_w}{J_r}\frac{c_1+c_2}{c_1}\right)(\omega_r-\omega_w) \\ & + c_2\dot{\omega}_d\frac{J_w}{c_1}-\frac{\eta\,\mathrm{J_w}}{\mathrm{c_1}}f(s) \end{aligned} \tag{75}$$

In addition to the sliding mode controller being robust to parametric uncertainties, it can also be shown that the sliding surface or boundary layer will be reached in finite time (smaller than $s(t=0)/\eta$ ) [57]. Upon implementation of the controller, the unmeasured states $\theta_r$ & $\omega_r$ are replaced with their estimates. It is shown in [60] that the system is robust to uncertain systems and external disturbances within a set of bounds defined by η. Closed-loop stability analysis, similar to the method used for the adaptive nonlinear controller, was performed using Lyapunov functions to prove boundedness of the parameter and state errors as well as the controller tracking error and is included in Appendix E.

## 6.2 RESULTS AND DISCUSSIONS

Figure 66 and Figure 68 show the response of the system with the sliding mode controller assuming that the sidewall parameters are known. In simulation, the controller is very effective at reaching and maintaining the optimal slip ratio. The ring angular velocity reaches its target velocity within five-hundredths of a second and remains on the sliding surface with little to no oscillations. As with the nonlinear controller, the tread parameters converge close to their true values within 0.5 seconds.

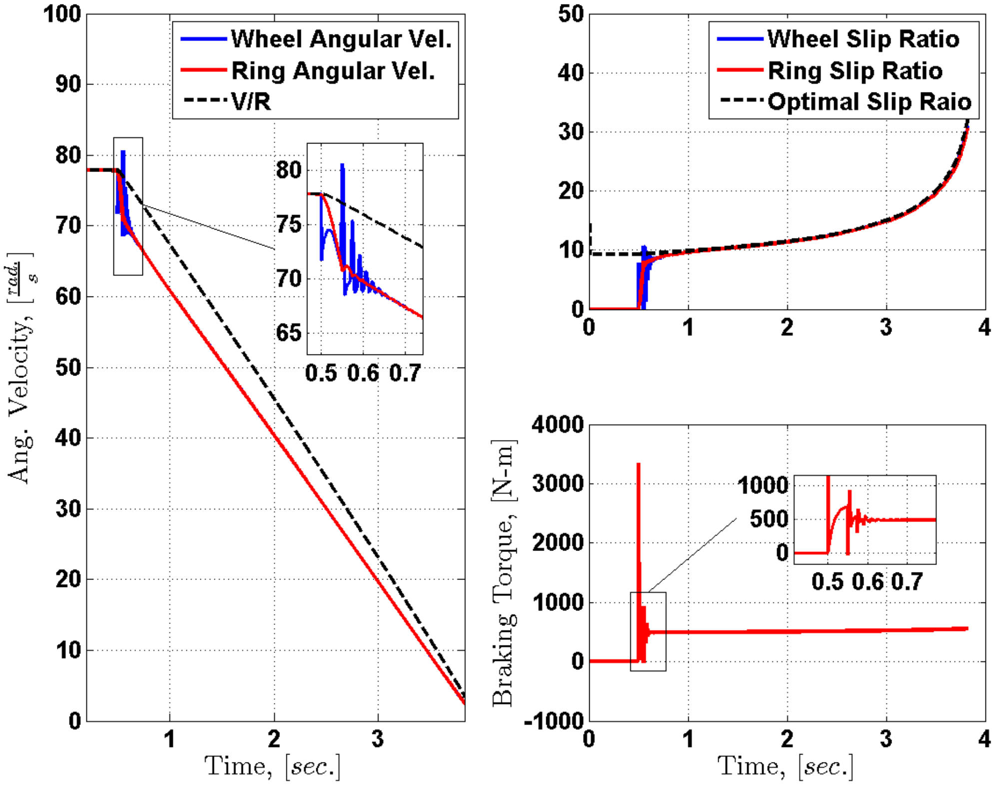

**FIGURE 66: BRAKING RESPONSE FOR SLIDING MODE CONTROLLER (KNOWN SIDEWALL PARAMETERS)**

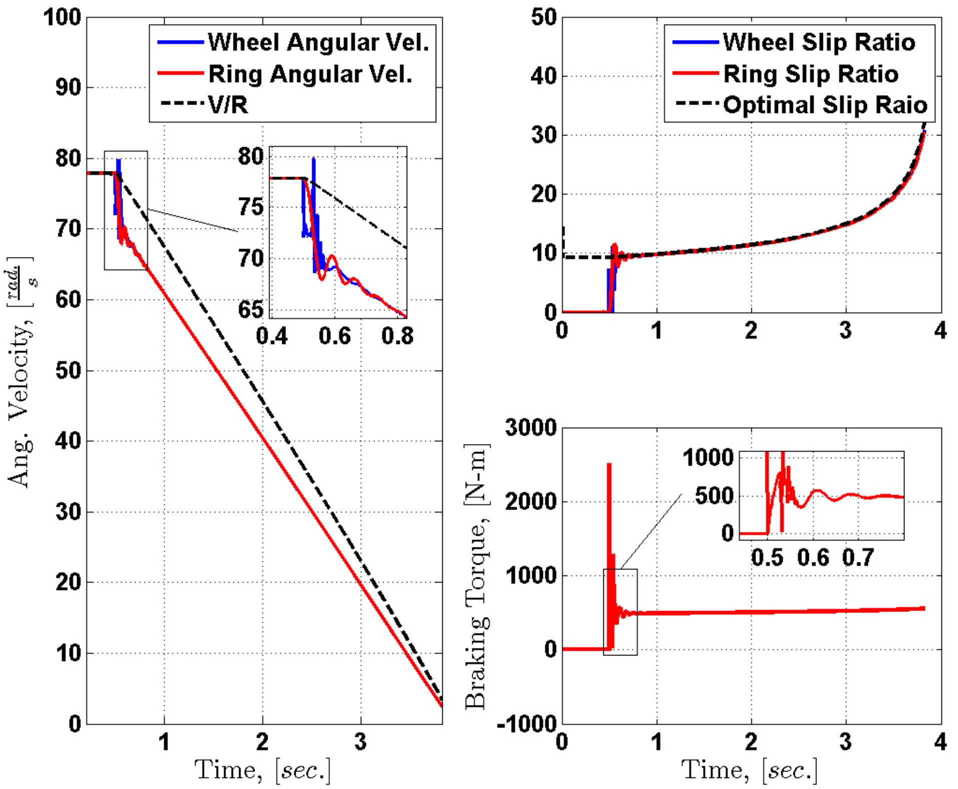

FIGURE 67: BRAKING RESPONSE FOR SLIDING MODE CONTROLLER (UNKNOWN PARAMETERS)

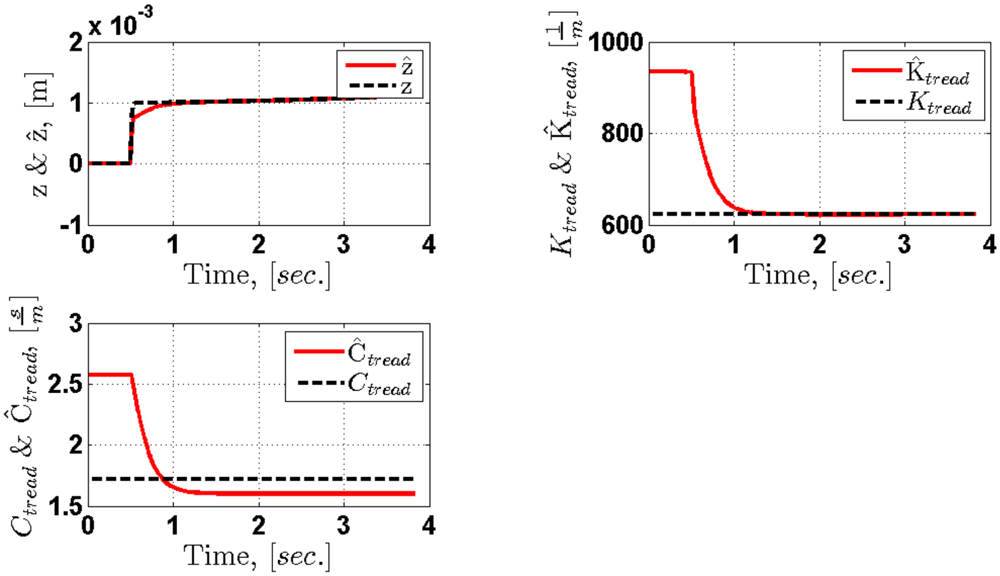

FIGURE 68: PARAMETRIC ESTIMATIONS & ERRORS FOR SLIDING MODE CONTROLLER (KNOWN SIDEWALL PARAMETERS)

Figure 67 and Figure 69 represent the controller response, in conjunction with the sidewall and tread adaptation schemes, when both the tread and sidewall parameters are assumed to be of the torsionally stiffer tire. Here the system has some small oscillations in angular ring velocity due to the state estimation error. The results also highlight the difficulties in estimating the parameter $\widehat{K}_T$ as the controller's performance increases.

While the simulation results show that there is indeed some oscillation in actual angular ring velocity, the controller is in fact very successfully forcing the estimated angular ring velocity to track the desired velocity by driving the function $s(x, \omega_d)$ to zero (Figure 70). This results in a system where the actual angular ring velocity exhibits oscillations while the estimated angular ring velocity, which is used in the parameter adaptation laws (Equation (35)), has minimal oscillations, as shown in Figure 71. This

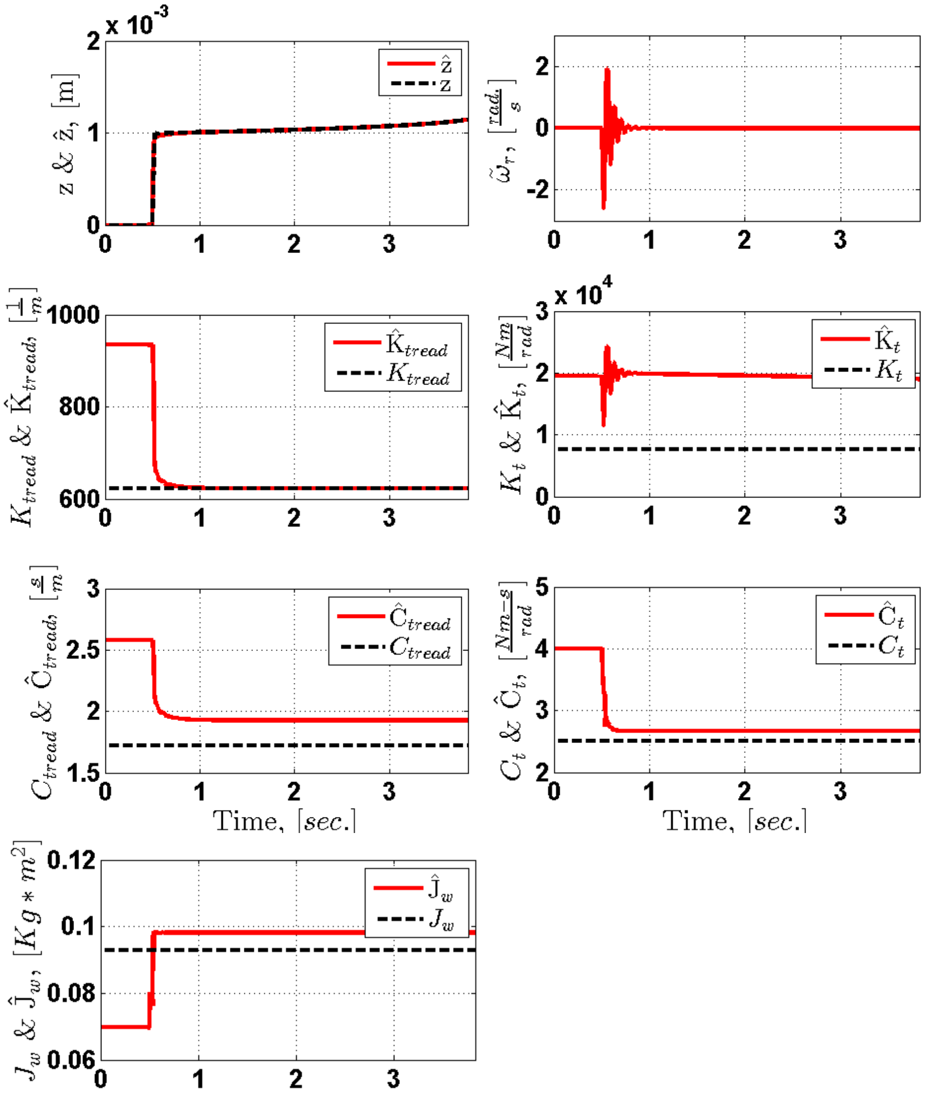

FIGURE 69: PARAMETRIC ESTIMATIONS & ERRORS FOR SLIDING MODE CONTROLLER (UNKNOWN PARAMETERS)

results in a reduction of the persistence of excitation, as seen by the adaptation laws, thus reducing the ability to estimate the system parameters. This phenomena highlights the following dilemma encountered with many adaptive control systems; better plant parameter/state estimation generally improves tracking performance, however, better tracking performance of an estimated state can reduce the parameter convergence rate (through lack of persistent excitation)

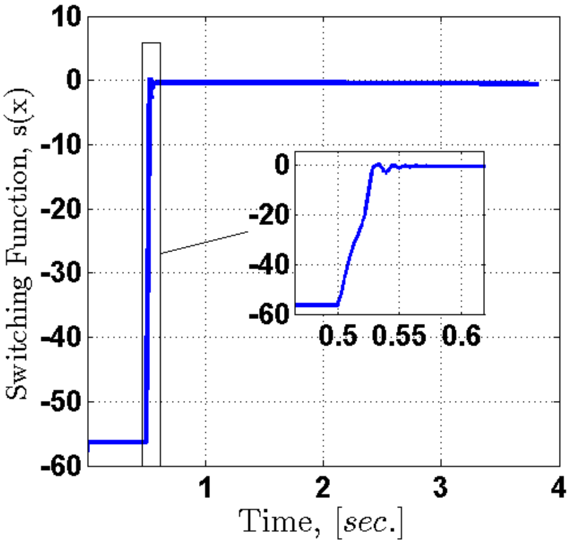

**FIGURE 70: SLIDING FUNCTION FOR SLIDING MODE CONTROLLER (UNKNOWN PARAMETERS)**

The sensitivity of the controller performance to an unmeasured brake torque disturbance was evaluated in Figure 72 by including a 50% peak-to-peak 1st harmonic oscillation to the applied brake torque $T_b$. These results are representative of the sliding mode controller assuming known tread parameters, unknown sidewall parameters, and no parameter adaptation. The sliding mode controller, which is known for its robustness to unmodeled dynamics and disturbances, performs significantly better than the nonlinear controller in the presence of the brake torque disturbance, however the controller still exhibits some large and high-frequency oscillations in $T_b$.

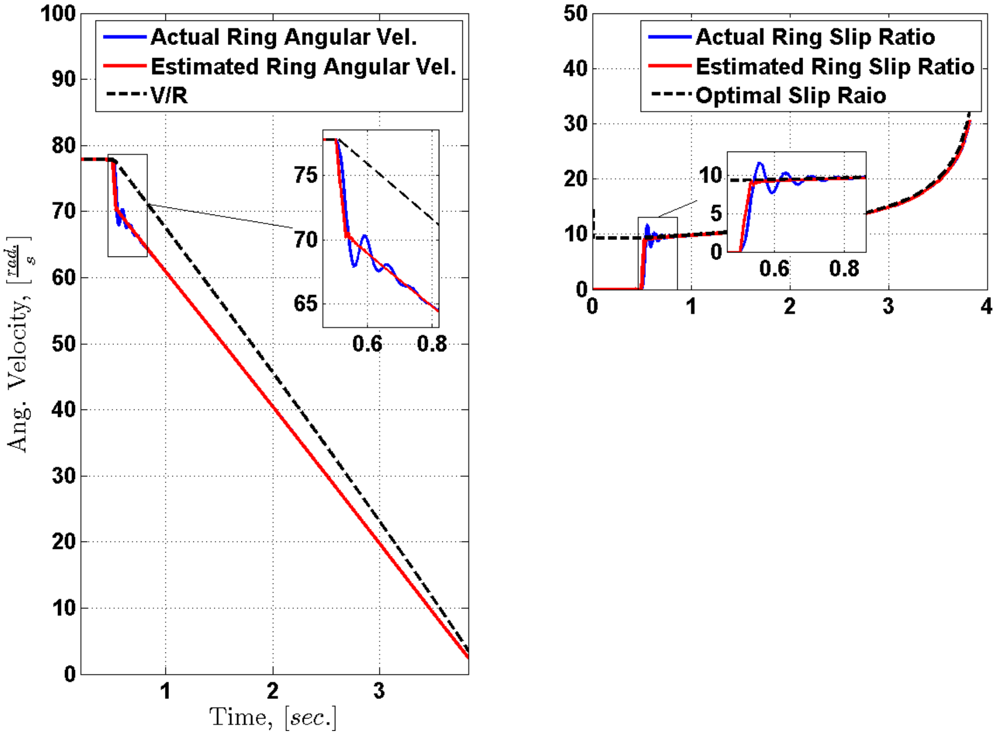

FIGURE 71: COMPARISON OF ACTUAL & ESTIMATED STATES FOR SLIDING MODE CONTROLLER (UNKNOWN PARAMETERS)

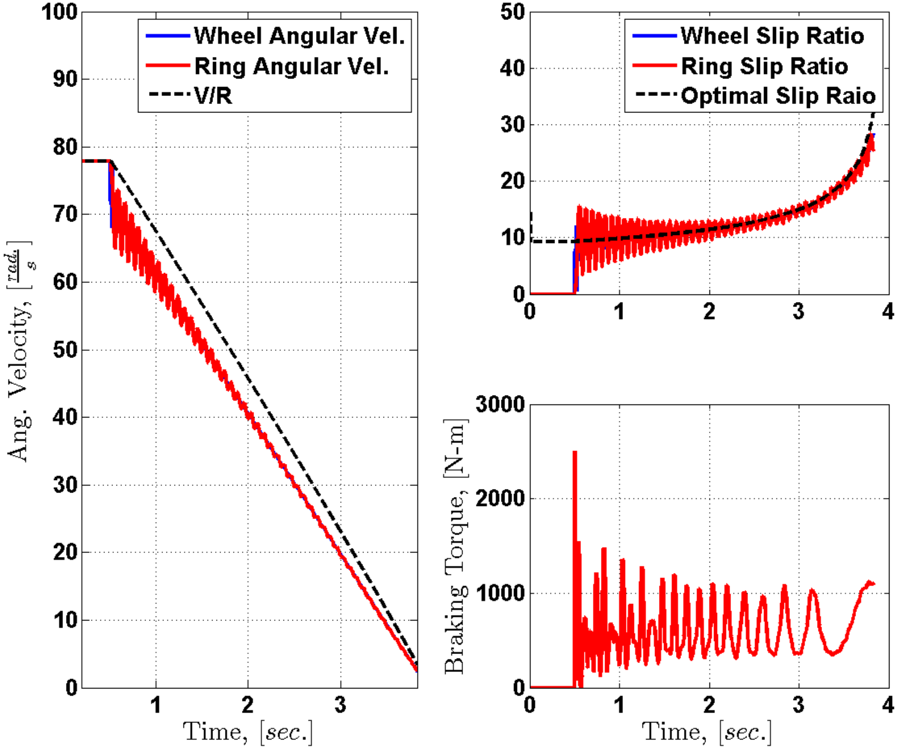

FIGURE 72: BRAKING RESPONSE FOR SLIDING MODE CONTROLLER (WITH 50% PEAK-TO-PEAK DISTURBANCE IN TB)

## 6.3 CHAPTER SUMMARY

This chapter proposed a sliding mode controller that can be used in conjunction with the sidewall and tread adaptation scheme developed in Chapter 5. The controller was designed as an alternative to the nonlinear controller and to improve the robustness of the system to model uncertainty and unmeasured disturbances. Closed-loop stability analysis was performed using Lyapunov functions to prove boundedness of the parameter and state errors as well as the controller tracking error and is discussed in Appendix E. Simulation results showed that the sliding mode controller was able to track the desired slip ratio in the presence of model uncertainties. The adaptation scheme continued to show quick convergence of the parameters when the sidewall parameters are known but the tread parameters are not. However, when both the sidewall and tread parameters are unknown the adaptation laws are not as effective at the convergence of the sidewall stiffness parameter $K_t$, due to the reduction of persistent excitation as the controller performance increases.

The system's ability to track the desired slip ratio in the presence of unmeasured disturbances was also evaluated by including a 50% peak-to-peak disturbance in brake torque. Results showed that the sliding mode controller has improved performance over the nonlinear controller in the presence of the brake torque disturbance.

# CHAPTER 7: ROBUST OBSERVER

It can be expected that when designing a tracking controller, the controller's performance should increase as the estimation of the state to be tracked is improved. Written in terms of the current problem, the braking/traction controller that is being proposed in this research should have improved performance as the accuracy of the ring velocity estimation is increased. This can be achieved using multiple methods; one of which is utilizing an adaptation scheme, as derived in a previous chapter, to improve the plant parameter estimates. Another option to improve the ring velocity estimation is to design a closed-loop observer which utilizes feedback signals to better estimate the desired states. The following chapter introduces such a closed-loop observer for the ring dynamics.

## 7.1 OBSERVER MODELING

The author investigated several different forms of observers ranging from an adaptive Luenberger observer, to a Dual Extended Kalman Filter, and a novel H-infinity Observer. Due to limitations in the structure of the system (for example, the product of both unknown parameters and unknown states in the system equations) and available measurements, the robust H-infinity observer was determined to be the most appropriate solution for both simulation and experimental implementation. By using robust H-infinity techniques an observer can be designed which accommodates the structure of the system and allows for some uncertainty in sensor noise, unmodeled dynamics, and disturbances; all of which are vitally important for experimental investigation.

Prior to the derivation of the H-infinity observer, a closed-loop observer structure must be introduced. The observer structure used in this chapter is based upon the work of [58] and [59]. In these papers a "dynamic" observer is presented that replaces the static gain of the classical observer structure with a filter that can provide additional degrees of freedom to the system and allow the designer to create a filter such that the estimation error dynamics has some specified frequency characteristics. Framing the observer in this context allows the estimation problem to be viewed as a feedback stabilization problem, thus allowing for the implementation of general control theory.

The general structure of this dynamic observer is shown in Figure 73. Here $P_{actual}$ represents the actual system plant, where $P_0(s)$ is the assumed nominal plant, $\Delta$ is the bounded uncertainty, and $C$ as the output matrix. The estimates of the actual states $x$ and $y$ are constructed through the closed-loop dynamic observer where the input to the nominal plant includes both the control inputs $Bu$ and a correction term $z$. This correction term is the output of the feedback terms $C_1G(s)e$ which are determined by the designer to make the state estimation error $\tilde{x}$ asymptotically converge to zero, and can be designed using traditional control techniques.

The dynamic observer portion of Figure 73 can be written in equation form as follows:

$$\hat{x} = \phi_0(s)(Bu + C_1 x_1) \tag{76}$$

$$x_1 = G(s)e \tag{77}$$

$$\hat{y} = C_y x \tag{78}$$

And rearranging equations (76) and (77) into state-space form,

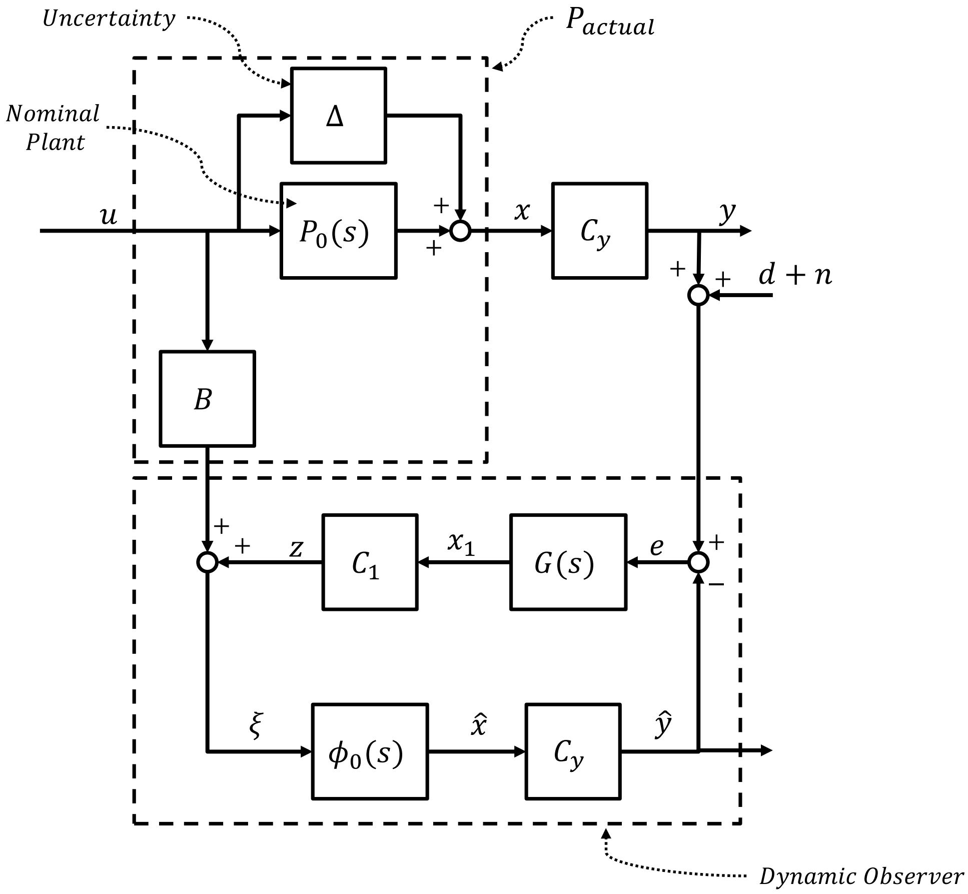

**FIGURE 73: UNCERTAIN PLANT AND DYNAMIC OBSERVER STRUCTURE**

$$\hat{x} = (sI - A)^{-1}(Bu + C_1 x_1) = \int \dot{\hat{x}}\, dt \xrightarrow{yields} \dot{\hat{x}} = A\hat{x} + Bu + C_1 x_1 \tag{79}$$

$$x_1 = (sI - A_1)^{-1} B_1 e = \int \dot{x}_1\, dt \xrightarrow{yields} \dot{x}_1 = A_1 x_1 + B_1 e \tag{80}$$

It can be valuable to realize that by allowing $A_1 = I$ and $x_1 = -B_1 e$, then $\dot{x}_1 = 0$ and equation (79) can be written as:

$$\dot{\hat{x}} = A\hat{x} + Bu - C_1 B_1 e \tag{81}$$

which, is of the same form as the standard constant gain Luenberger Observer. It can also be shown that the dynamic observer will always provide equal or better performance in comparison to the state space observer [58]. Furthermore, the generality and flexibility that is provided through this structure allows the designer to approach the problem as a feedback stabilization system and thus capitalize on more advanced feedback design techniques.

Now considering the stability of the observer, we can analyze the convergence properties of the estimation error as follows:

$$\dot{\tilde{x}} = \dot{x} - \dot{\hat{x}} = (Ax + Bu) - (A\hat{x} + Bu + C_1 x_1) = A\tilde{x} - C_1 x_1 \tag{82}$$

Rewriting Equations (80) and (82) in state space form,

$$\begin{Bmatrix} \dot{x}_1 \\ \dot{\tilde{x}} \end{Bmatrix} = \begin{bmatrix} A_1 & B_1 C_y \\ -C_1 & A \end{bmatrix} \begin{Bmatrix} x_1 \\ \tilde{x} \end{Bmatrix} = \bar{A} \begin{Bmatrix} x_1 \\ \tilde{x} \end{Bmatrix} \tag{83}$$

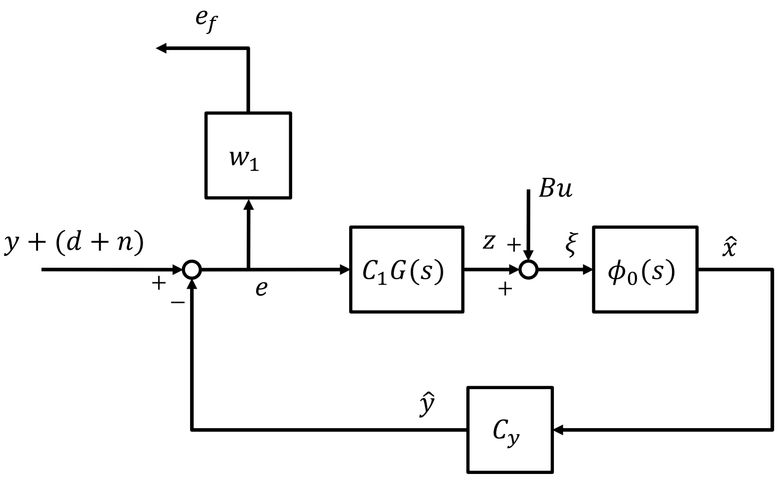

FIGURE 75: DYNAMIC OBSERVER STRUCTURE

The estimation error $e$ is then asymptotically convergent to zero iff $\bar{A}$ is negative definite, where $A_1$, $B_1$, and $C_1$ are chosen by the designer. Additional information and proofs regarding this observer structure can be found in [58, 59].

Since the aforementioned observer structure allows the designer to take advantage of well-established feedback control techniques, and due to the uncertainties and unmodeled dynamics inherent in the system, the author decided to utilize the robust H-infinity technique to achieve stabilization of the observer. In order to construct the H-infinity based observer, it is valuable to first analyze the dynamic observer separate from the plant, as is shown in Figure 75. It should be noted that in addition to the dynamic observer, a weighting function $w_1$ has been added from the error variable $e$. This common

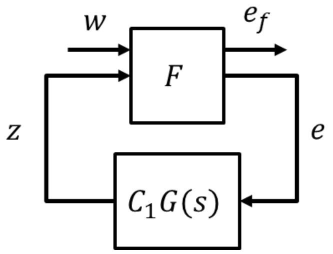

FIGURE 74: LFT FORM OF DYNAMIC OBSERVER

technique in robust control provides the designer the ability to weight the tracking error more or less based on its frequency content. The dynamic observer can be further placed into standard LFT form, as shown in Figure 74.

Where, $F$ is the generalized plant and is of the form:

$$F = \left[\begin{array}{c|cc} A & B_1 & B_2 \\ \hline C_{y1} & D_{11} & D_{12} \\ C_{y2} & D_{21} & D_{22} \end{array}\right] \tag{84}$$

$$A = \begin{bmatrix} 0 & 0 & 1 & 0 \\ 0 & 0 & 0 & 1 \\ -K_t/J_w & K_t/J_w & -C_t/J_w & C_t/J_w \\ K_t/J_r & -K_t/J_r & C_t/J_r & -C_t/J_r \end{bmatrix} \tag{85}$$

$$B_1 = \begin{bmatrix} 0 & 0 & 0 & 0 \\ 0 & 0 & 0 & 0 \\ -1/J_w & 0 & 0 & 0 \\ 0 & R/J_r & 0 & 0 \end{bmatrix} \tag{86}$$

$$B_2 = \begin{bmatrix} 1 & 0 & 0 & 0 \\ 0 & 1 & 0 & 0 \\ 0 & 0 & 1 & 0 \\ 0 & 0 & 0 & 1 \end{bmatrix} \tag{87}$$

$$C_{y1} = \begin{bmatrix} -W_1 & 0 & 0 & 0 \\ 0 & 0 & -W_1 & 0 \end{bmatrix} \tag{88}$$

$$C_{y2} = \begin{bmatrix} -1 & 0 & 0 & 0 \\ 0 & 0 & -1 & 0 \end{bmatrix} \tag{89}$$

$$D_{11} = \begin{bmatrix} 0 & 0 & W_1 & 0 \\ 0 & 0 & 0 & W_1 \end{bmatrix} \tag{90}$$

$$D_{21} = \begin{bmatrix} 0 & 0 & 1 & 0 \\ 0 & 0 & 0 & 1 \end{bmatrix} \tag{91}$$

$$D_{12} = \begin{bmatrix} 0 & 0 & 0 & 0 \\ 0 & 0 & 0 & 0 \end{bmatrix} \tag{92}$$

$$D_{22} = \begin{bmatrix} 0 & 0 & 0 & 0 \\ 0 & 0 & 0 & 0 \end{bmatrix} \tag{93}$$

The input vector $w$ and the internal state vector $x$ are also defined as follows:

$$w = \begin{bmatrix} T_B \\ F_f \\ \theta_w \\ \omega_w \end{bmatrix} \tag{94}$$

$$x = \begin{bmatrix} \theta_w \\ \theta_r \\ \omega_w \\ \omega_r \end{bmatrix} \tag{95}$$

An H-infinity observer can then be designed using standard robust control techniques to minimize the H-infinity norm of the external outputs $e_f$. This can be expressed as follows:

$$\begin{aligned} \hat{y} &= C_y[\phi_0(s)Bu + \phi_0(s)C_1G(s)e] \\ &= \left(I + C_y\phi_0(s)C_1G(s)\right)^{-1}[C_y\phi_0(s)Bu + \phi_0(s)C_1G(s)y] \end{aligned} \tag{96}$$

And therefore, $e_f$ can be defined as:

$$\begin{aligned} e_f &= W_1(y - \hat{y}) \\ &= W_1\left(y - \left(I + C_y\phi_0(s)C_1G(s)\right)^{-1}\left[C_y\phi_0(s)Bu + \phi_0(s)C_1G(s)y\right]\right) \\ &= W_1\left(I + C_y\phi_0(s)C_1G(s)\right)^{-1}\left[-C_y\phi_0(s)Bu + y\right] \\ &= W_1\left(I + C_y\phi_0(s)C_1G(s)\right)^{-1}\left[-C_y\phi_0(s)Bu + \Delta u + (n + d)\right. \\ &\qquad\qquad \left. + \; C_y\phi_0(s)Bu\right] \\ &= W_1\left(I + C_y\phi_0(s)C_1G(s)\right)^{-1}[\Delta u + (n + d)] \end{aligned} \tag{97}$$

Then, by designing the H-infinity observer to minimize the $\|*\|_\infty$ of the closed-loop transfer function matrix from inputs to weighted error $e_f$, the effects of model uncertainties, noise, and disturbances will consequently also be minimized[11]. The response of this observer to an impulse of 2500 Nm in brake torque $T_b$ can be observed in Figure 76, where the nominal observer plant parameters differ significantly from the actual model parameters (as shown in Table 4). Here the estimated state $\widehat{\omega}_r$ follows the actual ring velocity $\omega_r$ well and converges to the true value within 0.04 sec despite the model parameters differing from the true values by up to 250%.

**TABLE 4: NOMINAL OBSERVER PARAMETERS VS. ACTUAL PLANT PARAMETERS:**

| | Nominal Observer Parameters | Actual Plant Parameters |
|---|---|---|
| $K_t\ \left[\frac{Nm}{rad}\right]$ | 19,438 | 7,616 |
| $C_t\left[\frac{Nm}{rad * s}\right]$ | 4 | 2.5 |
| $J_r\ [Kg * m^2]$ | 0.75 | 1 |
| $J_w\ [Kg * m^2]$ | 0.06975 | 0.093 |

---

[11] Additional frequency weighting can be included for the noise and disturbances

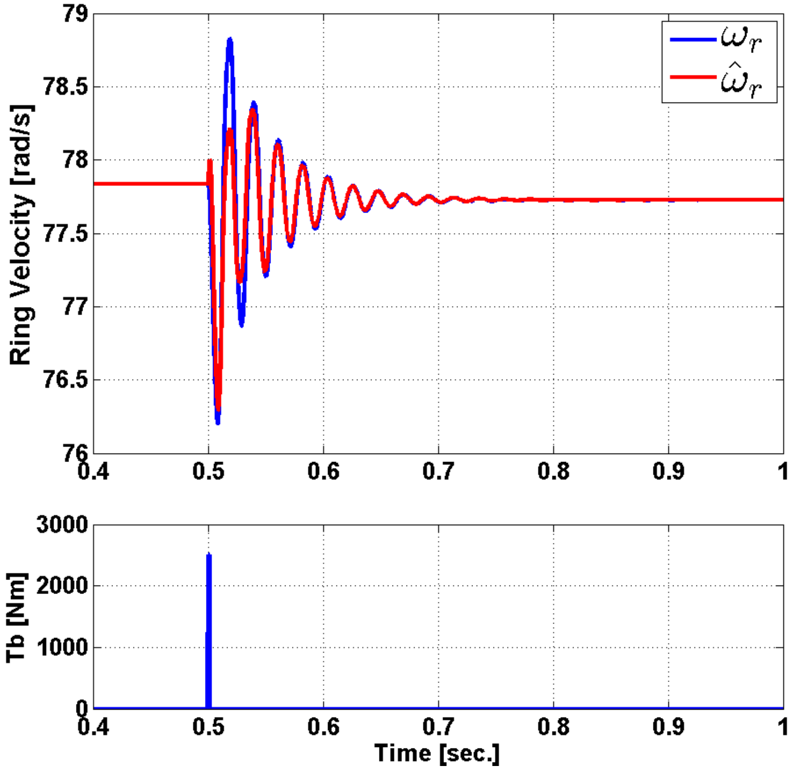

FIGURE 76: ROBUST OBSERVER RESPONSE TO BRAKE TORQUE IMPULSE

It is important to realize that under quasi-steady state conditions, when $\omega_r$ equals $\omega_w$ the estimation error $e$ becomes small and Equation (96) approaches $\hat{y} = C\phi_0(s)Bu$. This results in the observer's output becoming similar to the nominal plant $P_0$ under quasi-steady state conditions. This means that the observer will track the states well during the initial dynamic region, but can struggle to track states such as position when it reaches quasi steady-state conditions. Due to this limitation, and the lack of parametric estimation feedback to the nominal plant $P_0$, it is not beneficial to incorporate the sidewall adaptation scheme with the robust sidewall observer in its current structure as the parameter estimations will converge to those of the nominal plant $P_0$ when there is a lack of persistent excitation.

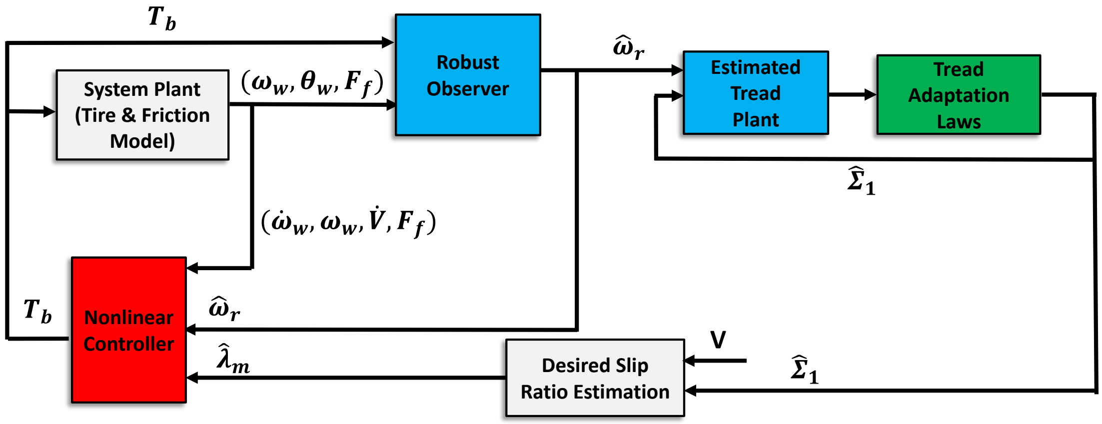

FIGURE 77: SCHEMATIC OF PROPOSED NONLINEAR CONTROLLER SCHEME W/ ROBUST OBSERVER

Combining the robust observer with the nonlinear controller and the tread adaptation scheme, the closed-loop structure is shown in Figure 77.

## 7.2 RESULTS AND DISCUSSIONS

Figure 78 and Figure 79 show the system response for the nonlinear controller combined with the robust observer proposed in this chapter, where the braking event begins at 0.5 seconds. In this simulation the robust observer's nominal plant $P_0$ is that of the standard torsional stiffness tire, while the actual tire is in fact the low torsional stiffness tire (representative of a worst-case scenario). The system parameters & estimated states are assumed to be unknown prior to the event. The system response shows that the robust observer/nonlinear controller combination is very effective at controlling the target ring slip ratio, even though the assumed sidewall parameters differ from the actual parameters by as much as 250%. Figure 79 shows the tread parameter and state estimations for the braking event. Note that the sidewall adaptation scheme is not included for the reasons stated earlier. The estimated states errors $\tilde{z}$ and $\widetilde{\omega}_r$ quickly converge to zero and the estimated tread parameter $K_{tread}$ quickly converges to its true value within 0.5sec, even though the estimated sidewall parameters are unknown. Figure 80 shows the system slip ratio tracking response and again highlights that the response of the actual ring angular velocity is less oscillatory than the estimated ring velocity. It also shows how the target slip ratio converges upon the optimal slip ratio as the tread parameters converge to their true values. The results of these simulations demonstrates the robustness of the observer to parametric variations in the plant.

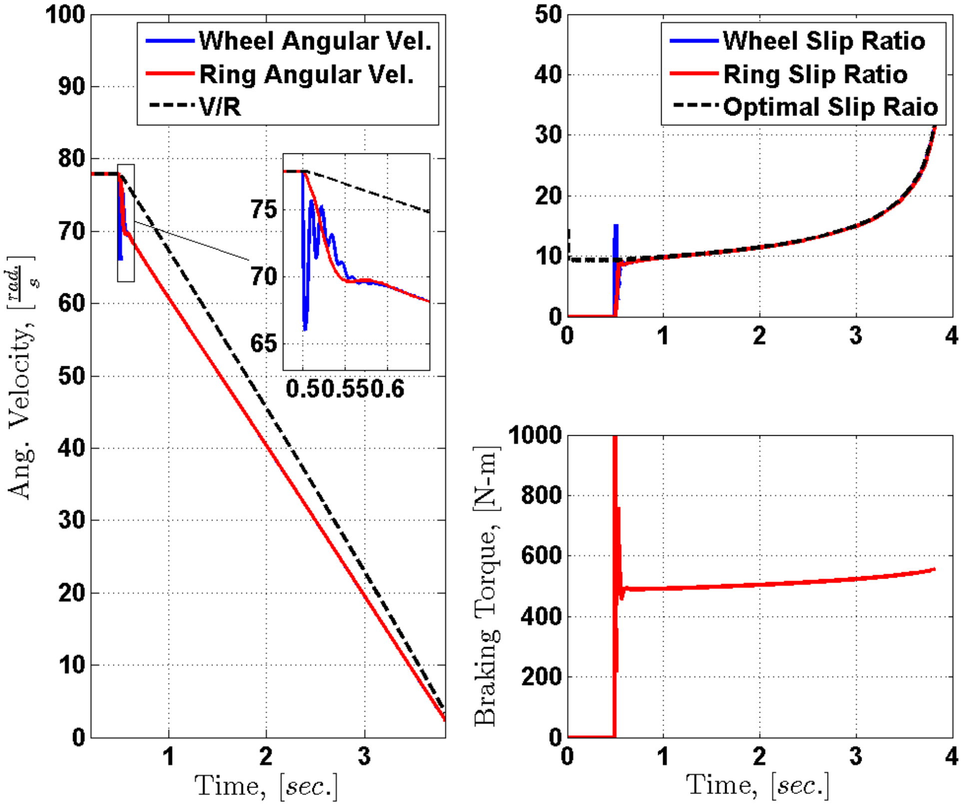

**FIGURE 78: BRAKING RESPONSE FOR PROPOSED NONLINEAR CONTROLLER W/ ROBUST OBSERVER (UNKNOWN PARAMETERS)**

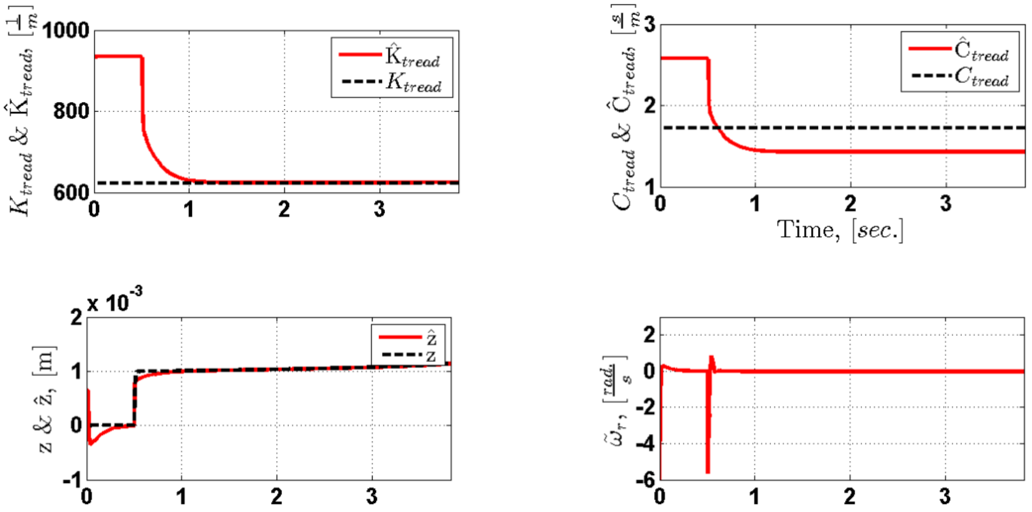

**FIGURE 79: TREAD PARAMETER ESTIMATIONS AND ERRORS FOR PROPOSED NONLINEAR CONTROLLER W/ ROBUST OBSERVER (UNKNOWN PARAMETERS)**

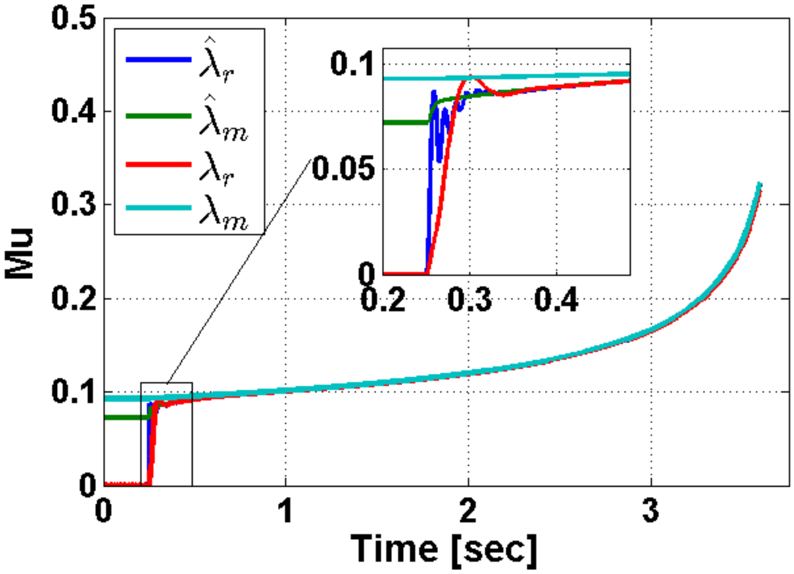

**FIGURE 80: SLIP TRACKING RESPONSE -- NONLINEAR CONTROLLER W/ ROBUST OBSERVER (UNKNOWN PARAMETERS)**

Figure 81 and Figure 82 represent the simulated system response when a 5% magnitude 1st harmonic disturbance is placed on the braking torque $T_b$, the tread parameters and the sidewall parameters are unknown. The response of the robust observer when incorporated with nonlinear controller produces a significantly improved response when compared with the results from the open-loop observer in Figure 60. In fact, the oscillations that were present in Figure 60 are all but eliminated. However, in Figure 83 and Figure 84, when the peak-to-peak magnitude of the disturbance is increased to 50%, as was observed in the experimental results, the oscillations become more prominent. Even still, the disturbance does not cause the same level of chattering in the control signal that was observed when only the open-loop observer was utilized. Notwithstanding, in experimental testing the disturbances were significant enough to prevent the robust observer from being successfully implemented on the experimental test fixture.

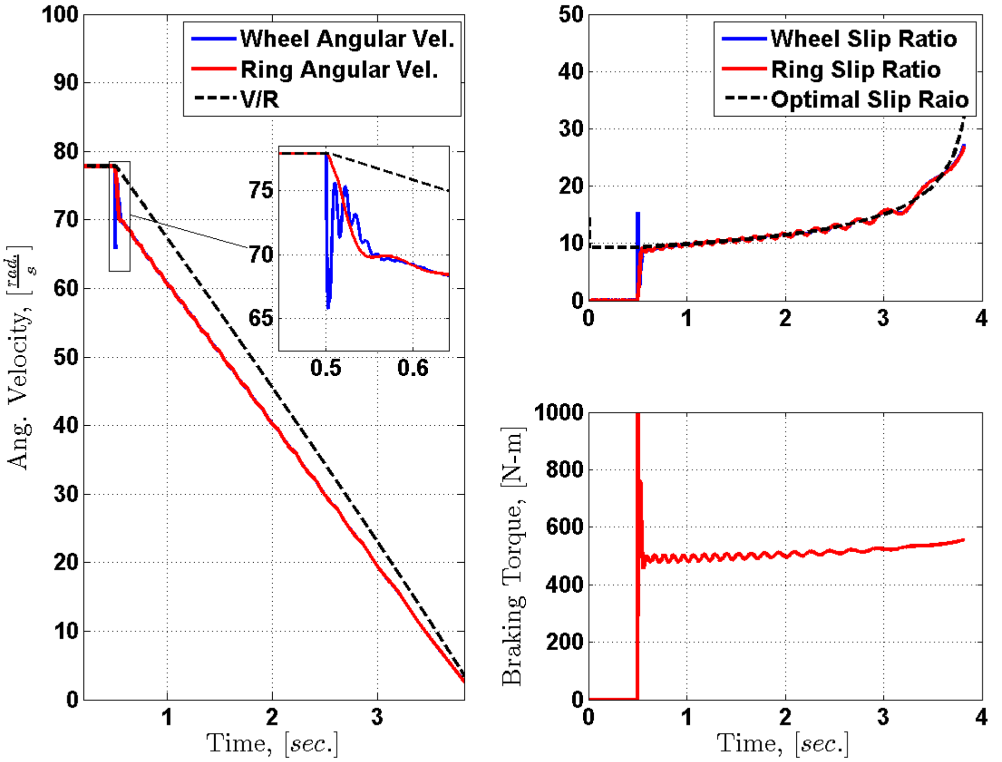

FIGURE 81: BRAKING RESPONSE FOR PROPOSED NONLINEAR CONTROLLER W/ ROBUST OBSERVER (WITH 5% PEAK-TO-PEAK DISTURBANCE IN TB)

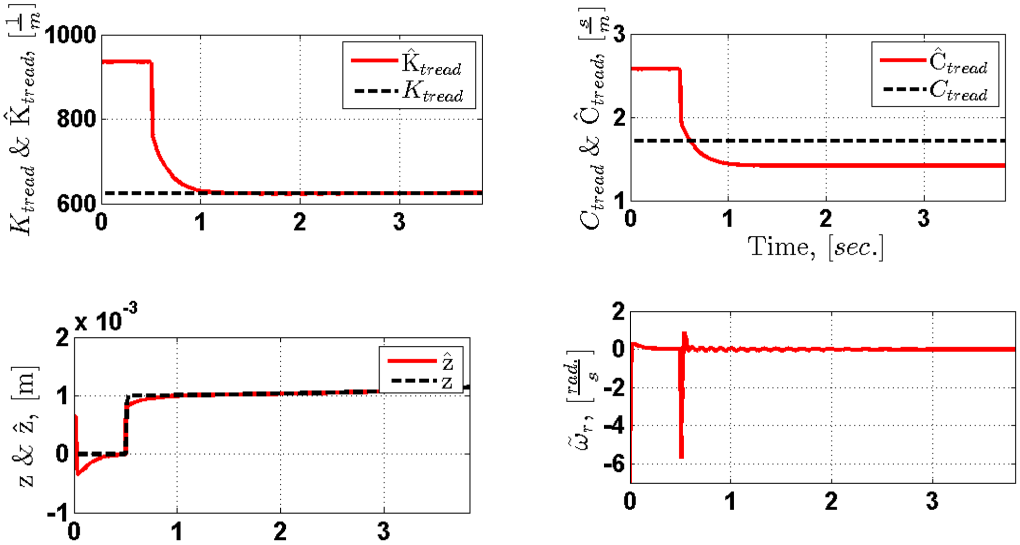

FIGURE 82: TREAD PARAMETER ESTIMATIONS AND ERRORS FOR PROPOSED NONLINEAR CONTROLLER W/ ROBUST OBSERVER (WITH 5% PEAK-TO-PEAK DISTURBANCE IN TB)

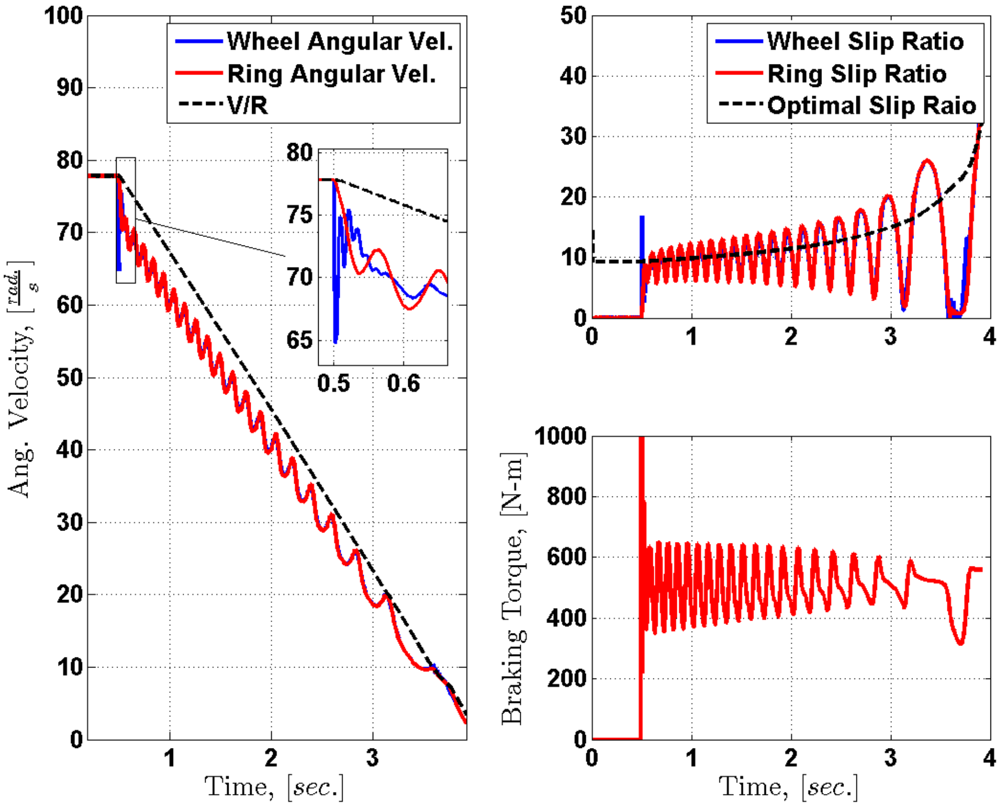

**FIGURE 83: BRAKING RESPONSE FOR PROPOSED NONLINEAR CONTROLLER W/ ROBUST OBSERVER (WITH 50% PEAK-TO-PEAK DISTURBANCE IN TB)**

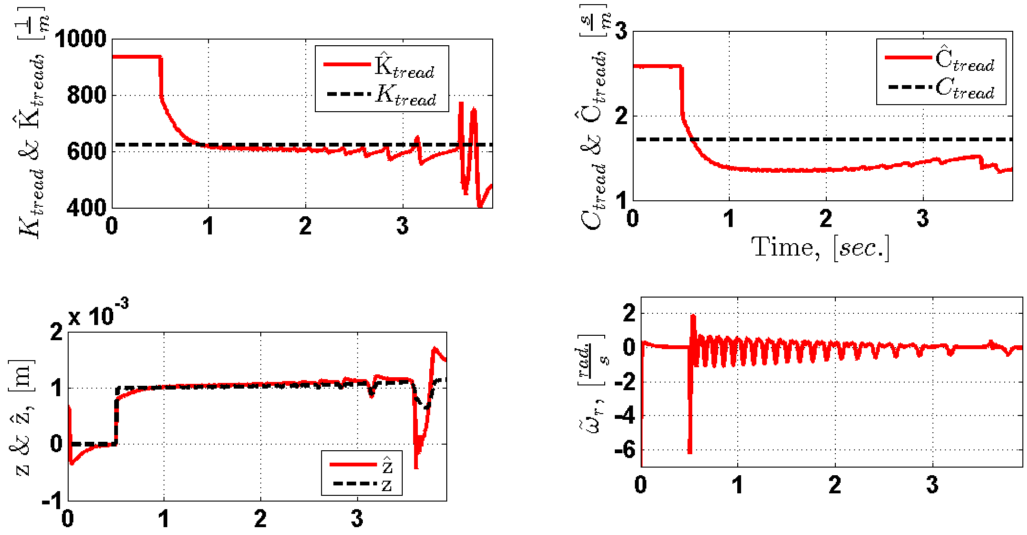

**FIGURE 84: TREAD PARAMETER ESTIMATIONS AND ERRORS FOR PROPOSED NONLINEAR CONTROLLER W/ ROBUST OBSERVER (WITH 50% PEAK-TO-PEAK DISTURBANCE IN TB)**

The robust observer can also be combined with the sliding mode controller that was developed in Chapter 6. Similar to the robust observer/nonlinear controller configuration, there is no sidewall parameters adaptation, but the tread adaptation scheme is still included. Figure 85 and Figure 86 show the response of this system when the observer's nominal plant $P_0$ represents the standard torsional stiffness tire, instead of the actual low torsional stiffness tire. The tread parameters are also assumed to be unknown. The system is successful at reaching the target ring slip ratio within 0.01 seconds and with minimal oscillations. It is apparent that in this configuration the sliding mode controller introduces some small chattering in the brake torque $T_b$, due to some of the estimation error from the robust observer.

Figure 87 and Figure 88 show the system response when a 5% peak-to-peak brake torque disturbance is introduced into the plant. The response is very similar to the response in Figure 81 and Figure 82, has very few oscillations, and is fairly robust to these disturbances. Figure 89 and Figure 90 are representative of the system in the presence of a 50% peak-to-peak brake torque disturbance. Once again the response is still very close to the robust observer/nonlinear controller case and is significantly improved over the open-loop observer cases. There appears to be some chattering in the system when the actual ring slip ratio touches zero at approximately 3 seconds, however the controller recovers from these oscillations quickly.

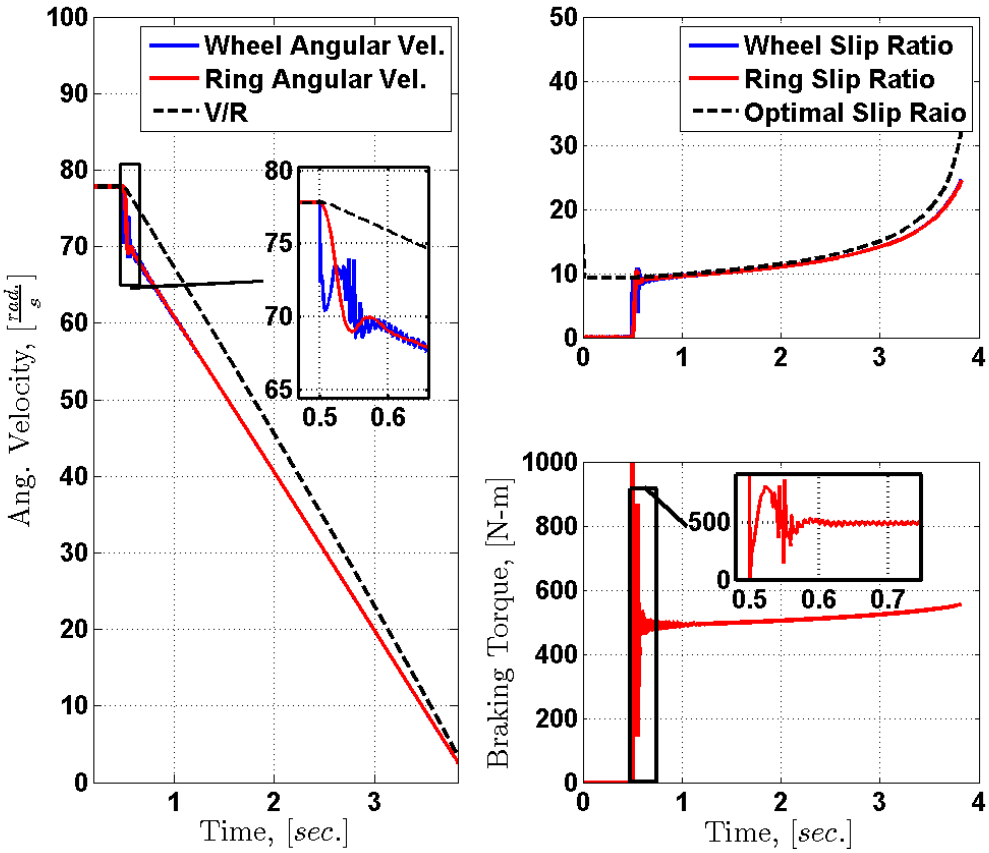

FIGURE 85: BRAKING RESPONSE FOR PROPOSED SLIDING MODE CONTROLLER W/ ROBUST OBSERVER (UNKNOWN PARAMETERS)

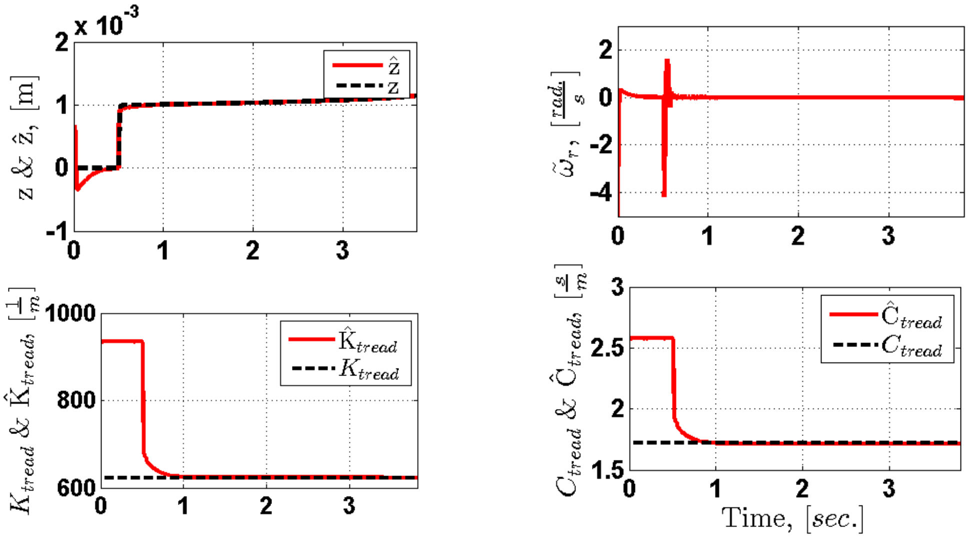

FIGURE 86: TREAD PARAMETER ESTIMATIONS AND ERRORS FOR PROPOSED SLIDING MODE CONTROLLER W/ ROBUST OBSERVER (UNKNOWN PARAMETERS)

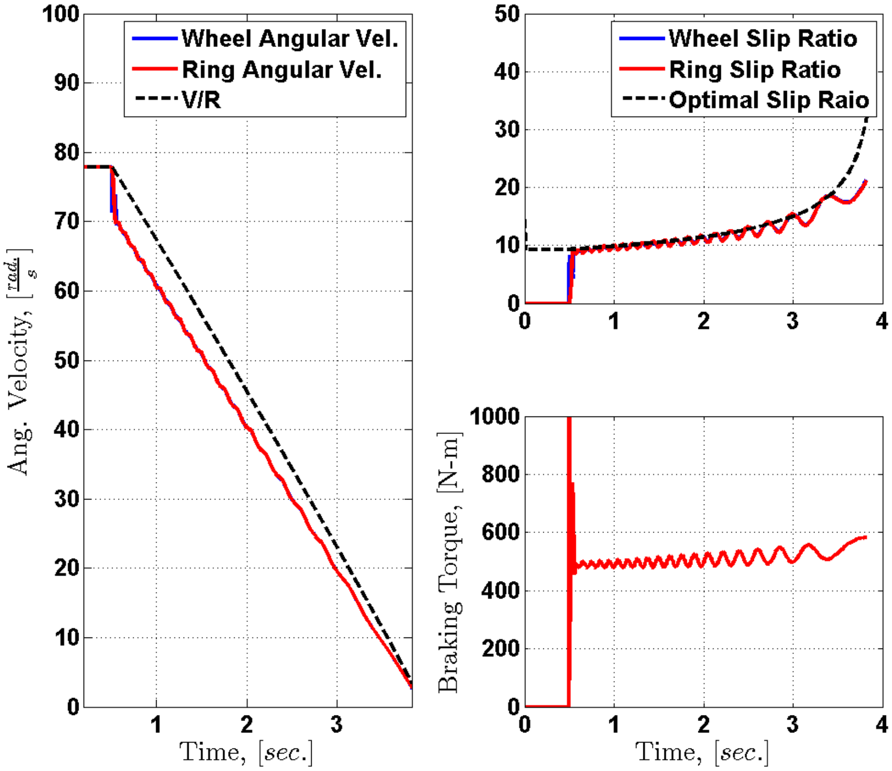

FIGURE 87: BRAKING RESPONSE FOR PROPOSED SLIDING MODE CONTROLLER W/ ROBUST OBSERVER (WITH 5% PEAK-TO-PEAK DISTURBANCE IN TB)

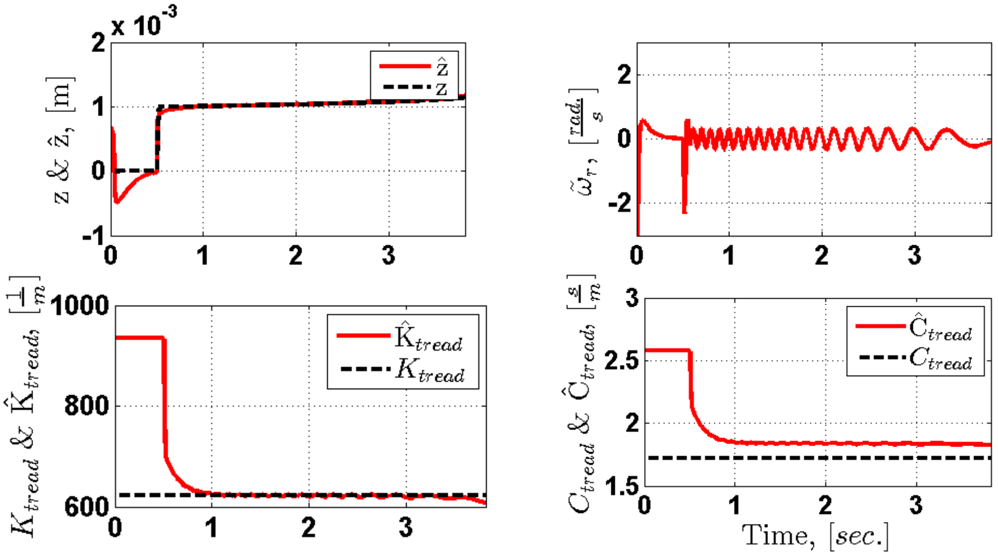

FIGURE 88: TREAD PARAMETER ESTIMATIONS AND ERRORS FOR PROPOSED SLIDING MODE CONTROLLER W/ ROBUST OBSERVER (WITH 5% PEAK-TO-PEAK DISTURBANCE IN TB)

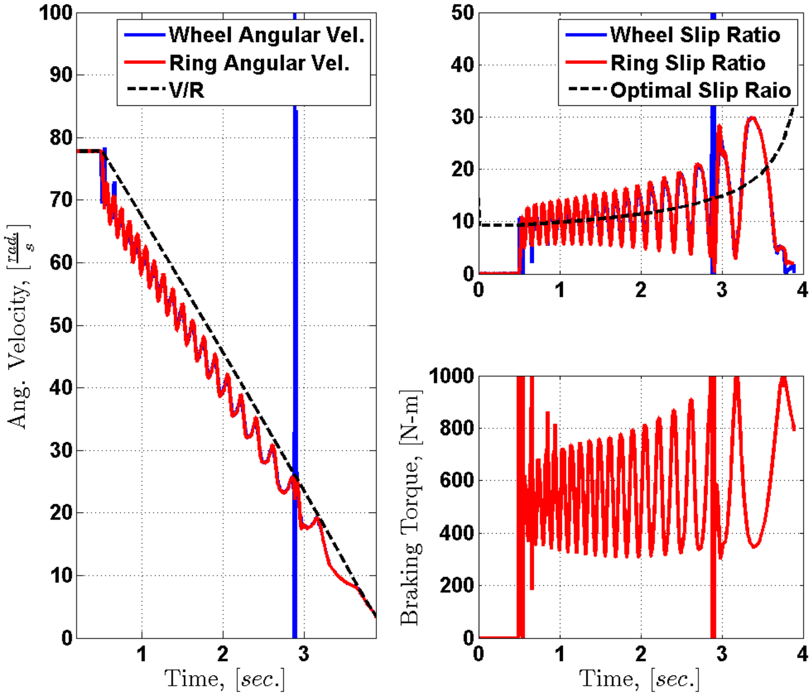

FIGURE 89: BRAKING RESPONSE FOR PROPOSED SLIDING MODE CONTROLLER W/ ROBUST OBSERVER (WITH 50% PEAK-TO-PEAK DISTURBANCE IN TB)

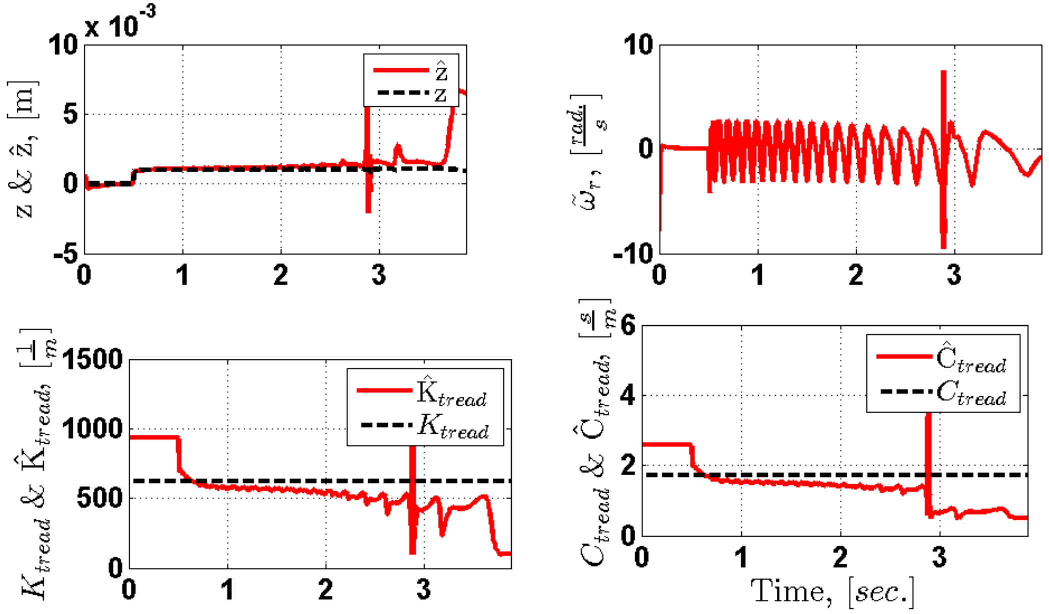

FIGURE 90: TREAD PARAMETER ESTIMATIONS AND ERRORS FOR PROPOSED SLIDING MODE CONTROLLER W/ ROBUST OBSERVER (WITH 50% PEAK-TO-PEAK DISTURBANCE IN TB)

## 7.3 CHAPTER SUMMARY

In this chapter, a closed-loop observer based on dynamic observer and $H_\infty$ techniques was proposed and can be combined with the nonlinear and sliding mode controllers (from Chapters 5 & 6) as well as the tread adaptation scheme. This observer can be used in place of the sidewall adaptation laws to estimate the position and velocity states, $\theta_r$ and $\omega_r$, respectively. The observer was designed as an alternative option to the open-loop sidewall observer used in Chapter 5, but in its current state removes the capability sidewall parameter adaptation.

Simulation results showed that when the nonlinear controller was combined with the robust observer, the system was very effective at tracking the optimal slip ratio. The system also demonstrated an increased robustness to unmeasured disturbances in brake torque. This system provided very similar responses when the robust observer and sliding mode controller were combined, even in the presence of the brake torque disturbances.

Further work could be conducted towards reincorporating the sidewall parametric adaptation scheme back into the closed-loop system. One potential method to achieve this capability, while still utilizing the robust control method, would be to utilize a scheduling technique that would switch between a bank of pre-formulated $H_\infty$ observers based on a parallel gradient-based adaptation law.

# CHAPTER 8: SUMMARY AND CONCLUSIONS

## 8.1 CONCLUSIONS

This dissertation investigated the interaction of tire torsional dynamics with anti-lock braking systems and traction controllers. This is done by first analyzing the limitations of a commercial ABS controller, and then, developing a set of new adaptive and robust control systems. The proposed closed-loop systems approach the problem in three parts: 1) estimation of the system states using open-loop and/or robust observers; 2) estimation of the tire sidewall/tread parameters through adaptation laws; 3) tracking control of the estimated state with nonlinear and sliding-mode controllers. This approach produced a comprehensive method of tracking the optimal ring slip ratio even when the tire's sidewall and tread parameters are unknown.

For the presented investigations, a detailed tire torsional dynamics model with a dynamic friction model was developed and coupled to a quarter-car model with a dynamic hydraulic/electromechanical braking system. An experimental test fixture was built that is capable of switching between a traditional brake hydraulic system or a custom-built electro-mechanical brake (EMB) system. The EMB system was designed to increase the bandwidth of the brake torque application system over the hydraulic-based system, thus allowing the controllers to better resolve and control the tire's torsional dynamics.

In Chapter 4, a detailed analysis of the interaction between a commercial ABS controller's settings and the tire's torsional dynamics was conducted through both simulations and experimental tests. It was clearly demonstrated through several tests that the controller's performance degraded when controller's filter was unable to effectively remove the tire's torsional dynamics. These observations highlighted the inability of current commercial ABS controllers to account for tire torsional dynamics and demonstrated a potential safety risk to the customer in the event of a change in the tire's torsional stiffness.

In Chapter 5, a nonlinear controller combined with a parametric adaptation scheme was proposed that estimates both the tire sidewall and tread parameters. The closed-loop system assumes that the vehicle longitudinal velocity, ground friction force, wheel speed, and brake torque are measureable. The development of the nonlinear controller, which was designed using Lyapunov techniques, also included a virtual damper that was systematically incorporated into the controller using backstepping techniques and the certainty equivalence principle. While the virtual damper showed an improvement in controller performance during simulations, it proved to be a vital tuning parameter during experimental tests and had a significant effect on the performance of the controller in the presence of brake torque disturbances. Closed-loop stability analysis was performed on the system using Lyapunov's direct method to prove boundedness of the parameter and state errors as well as the controller tracking error.

Numerous detailed simulations demonstrated that the nonlinear controller was able to track the optimal slip ratio with minimal control effort even when the initial parameters are assumed to be unknown. The adaptation laws showed very quick convergence of the tire's parameters and states. Experimental tests were also conducted using the nonlinear controller with no parameter adaptation and showed reasonable tracking of the desired slip ratio even when significant brake torque disturbances were present. However, the parameter adaptation schemes were not successfully incorporated due to large torque disturbances, which would drive the estimated stiffness parameters to zero. The large disturbances are attributed to specific limitations of the experimental test-rig including the rapid warping of the disc rotor from repeated braking events, wear of suspension components (such as the wheel bearing), a fixed suspension height which accentuates changes in normal load (from tire non-uniformity the dyno roller curvature), lack of brake torque $T_b$ measurements, and partial restriction of floating caliper due to ballscrew/gearbox coupling requirements.

In Chapter 6, an adaptive sliding mode controller was introduced that can be used in conjunction with the sidewall and tread adaptation scheme developed in Chapter 5. The controller was designed to improve the robustness of the system to model uncertainty and unmeasured disturbances. Closed-loop stability was verified for the system using Lyapunov analysis. Simulation results showed that, similar to the nonlinear controller, the sliding mode controller was able to track the desired slip ratio in the presence of model uncertainties. The adaptation scheme showed quick convergence of the tread parameters and sidewall damping term; however, it was not as successful at estimating the sidewall stiffness parameter $K_t$, due to a decrease in persistent excitation resulting from an increase in controller performance. The sliding mode controller proved to be more robust than the nonlinear controller in the presence of unmeasured disturbances such as a 50% peak-to-peak disturbance in brake torque.

In order to improve upon the ring state estimations, a closed-loop observer was proposed in Chapter 7 based on a dynamic observer and $H_\infty$ techniques. The observer was designed to replace the open-loop state estimation and can be combined with both the nonlinear and sliding mode controllers (from Chapters 5 & 6) as well as the tread adaptation scheme. The robust observer (which is an off-line $H_\infty$ design) removes the need for estimating the sidewall parameters $K_t$ and $C_t$ as it simply assumes they remain bounded. To accommodate larger variations of these parameters, it is possible to schedule the $H_\infty$ filters accordingly. Due to the robustness of the observer, simulation results showed that both the nonlinear controller and the sliding mode controller have very good performance when combined with the robust observer and tread adaptation scheme. The systems are both very robust to disturbances in unmeasured brake torque and are still fairly successful at adapting to the tread parameters.

## 8.2 MAIN CONTRIBUTIONS

The main contributions of this dissertation are summarized as follows:

1. The development of a nonlinear controller that incorporates both the torsional sidewall dynamics and a dynamic friction model

2. Development and implementation of a sliding-mode controller to account for the tire’s dominant dynamics and tread-ground contact friction dynamics
3. Development of an adaptation scheme for sidewall torsional dynamics and tread-friction model parameters
4. The development of a novel virtual damper emulation that can be incorporated into the controller to produce a closed-loop system response that acts similar to a well-damped system
5. A robust observer that allows for robust tracking of the system states in the presence of uncertainties and external disturbances

## 8.3 FURTHER WORK

The following is a brief list of refinements that could be pursued:

- Development of additional observers and adaptation techniques to eliminate the requirements of longitudinal velocity or friction force measurements and prior knowledge of the friction function.
- Investigation into observers or sensors that provide improved estimation of the brake torque generated by the caliper in the presence of disc rotor warping

- Accommodate a larger range of sidewall parameter uncertainties via the robust observer. One potential solution could be to utilize a scheduling technique that would switch between a bank of pre-formulated $H_\infty$ or similar observers based on a parametric estimations from an adaptation scheme running in parallel.
- Expansion of the experimental test fixture to allow vertical motion of the wheel, thus minimizing the effects of non-uniformity and more closely representing the actual vehicle usage. Also, one may also pursue redesign or replacement the EMB system to a more direct connection to the caliper in order to further increase the actuator bandwidth and remove any dynamics associated with the gearset and ballscrew

# APPENDICES

# APPENDIX A

## NOMENCLATURE

$\theta_r, \omega_r$ – Rotational Deflection & Velocity of the Ring
$\theta_w, \omega_w$ – Rotational Deflection & Velocity of the Wheel
$K_t$ – Torsional Stiffness of the Wheel/Ring
$C_t$ – Torsional Damping of the Wheel/Ring
$J_w$ – Wheel Inertia
$J_r$ – Ring Inertia
$m_v$ – Vehicle Mass
$R_r$ – Ring Radius
$R_w$ – Wheel Radius
$T_b$ – Braking Torque on the Wheel
$F_t$ – Frictional Ground Force at the Ring
$F_z$ – Vertical Load on Tire
$V$ – Vehicle Velocity
$V_r$ – Relative Sliding Velocity
$V_s$ – Stribeck Relative Velocity
$z$ – Tread Deflection
$g(V_r)$ – Friction Coefficient Curve
$\mu_c$ – Coulomb Friction
$\mu_s$ – Sliding Friction
$\alpha$ – Friction Curve Shaping Factor

## WHEEL/TIRE/TREAD PARAMETERS

| | **Parameters** |
|---|---|
| $K_{tread}$ $[1/m]$ | 623 |
| $C_{tread}$ $[s/m]$ | 1.72 |
| $R_r$ $[m]$ | 0.2855 |
| $R_w$ $[m]$ | 0.154 |
| $m_v$ $[Kg]$ | 1068 |
| $\mu_c$ | 0.75 |
| $\mu_s$ | 0.4 |
| $V_s$ $[m/s]$ | 10 |
| α | 0.75 |

### BRAKE HYDRAULIC PARAMETERS

$A_b$ – Brake Pad Area
$A_{vi}$ – Effective input valve area
$A_{vo}$ – Effective output valve area
$C_d$ – Discharge coefficient
$K_v$ – Valve gain
$P_{atm}$ – Atmospheric pressure
$P_c$ – Caliper pressure
$P_m$ – Master cylinder pressure
$q_i$ – Flow into valve
$q_o$ – Flow out of valve
$R_b$ – Effective Brake Pad Radius
$V$ – Volume of oil in brake lines and caliper
$\beta$ – Bulk modulus of fluid
$\rho$ – Fluid density
$\tau$ – Valve time constant
$\mu_{cal_s}$ – Static Caliper Coefficient of Friction
$\mu_{cal_k}$ – Kinetic Caliper Coefficient of Friction
$u_v$ – Valve Voltage

| | **Brake Hydraulic Parameters** |
|---|---|
| $\beta\ [GPa]$ | 1 |
| $\rho\ [Kg/L]$ | 0.85 |
| $P_m\ [MPa]$ | 5 |
| $A_{\max\ input}\ [mm^2]$ | 0.14 |
| $A_{\max\ output}\ [mm^2]$ | 0.04 |
| $C_d$ | 0.6 |
| $V\ [cm^3]$ | 50 |
| $R_b\ [m]$ | 0.1 |
| $A_b\ [m^2]$ | 0.0018 |
| $K_v$ | 1 |
| $\tau\ [Hz]$ | 100 |
| $\mu_{cal_s}$ | 0.8 |
| $\mu_{cal_k}$ | 0.45 |
| $u_v\ [V]$ | 0→1 |

# APPENDIX B

FIGURE 91: EMB W/ LOAD CELL (VIEW 1)

FIGURE 92: EMB W/ LOAD CELL (VIEW 2)

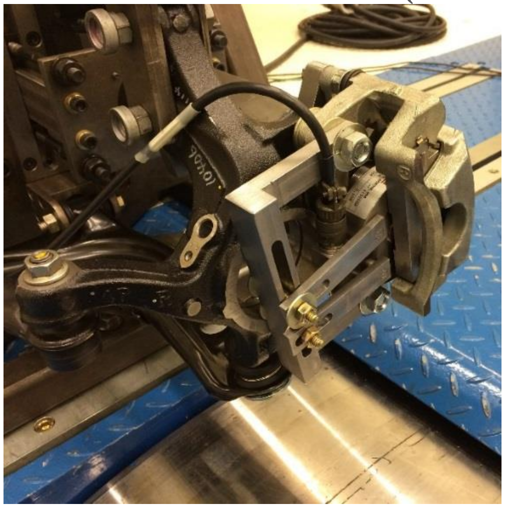

FIGURE 93: EMB W/ LOAD CELL (VIEW 3)

# APPENDIX C

## ACCELERATION-BASED ABS CONTROLLER

For this work, an acceleration-based ABS controller has been modeled after the ABS control algorithm outlined by the ABS system supplier Bosch [26]. The ABS controller cycles through various control phases is designed around a set of predetermined thresholds that are highlighted in Figure 94. While a brief description of the cycles and thresholds is given below, the reader is referred to source [26] for details .

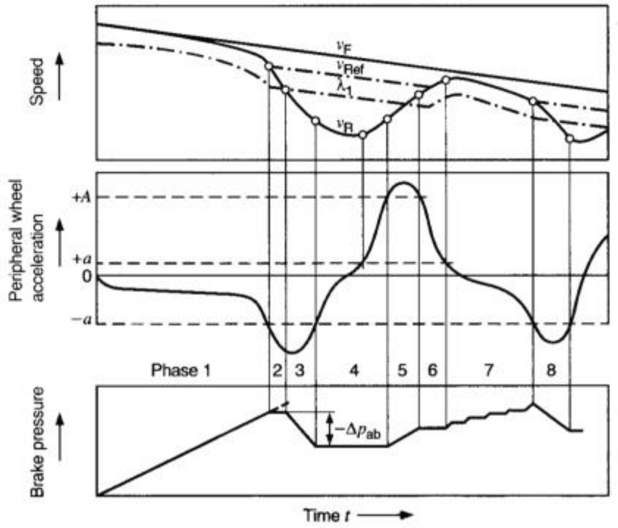

**FIGURE 94: BOSCH WHEEL-ACCELERATION BASED ABS ALGORITHM**

When the ABS is triggered it enters the first phase of the controller where the brake pressure increases until the peripheral wheel acceleration crosses the threshold (-*a*). The controller then switches to holding the brake pressure (Phase 2), to ensure that the tire friction has become fully saturated. Once the slip switching threshold ($\lambda_1$) has been reached, the controller will reduce the brake pressure (Phase 3) until the wheel peripheral acceleration exceeds the threshold (-*a*). Phase 4 represents a pressure holding phase where the wheel begins to accelerate again as the ring slip enters the stable region of the μ-slip curve. Phases 5 through 7 then represent various stages of pressure holding and pressure increases in order to approach the maximum friction coefficient. Once the peripheral wheel acceleration again crosses the threshold (-*a*) then the ring slip is assumed to be in the unstable region. The controller then immediately returns to Phase 3, where the brake pressure is decreased, and the cycle is repeated. Once the estimated vehicle velocity has fallen below a set minimum speed then the controller is deactivated and the brake pressure is allowed to increase, up to the master cylinder pressure, until the vehicle reaches a complete stop.

# APPENDIX D

# ADAPTIVE TRACTION CONTROLLER BASED ON THE RIGID WHEEL MODEL

## MODELING OF AN ADAPTIVE TRACTION CONTROLLER BASED ON A RIGID SIDEWALL TIRE

In this section the author utilizes a slightly modified version of the adaptive controller that was presented in [23], where the average lumped LuGre friction model is used in the adaptation laws instead of the distributed LuGre friction model. This controller also assumes that tire has a rigid sidewall, and thus the tire's torsional dynamics are not included in the controller. Note however, that the torsional dynamics of the wheel/tire system are still included in the simulated model, and will thus have an effect on the controller's performance. This controller is derived from the following assumed system dynamics:

$$J * \frac{d\omega_w}{dt} = F_t R_r - T_b \tag{98}$$

$$\frac{m_v}{4} * \frac{dV}{dt} = -F_t \tag{99}$$

$$F_t = F_z(K_{tread} z + C_{tread} \dot{z}) \tag{100}$$

$$V_r = V - R_r * \omega_w \tag{101}$$

$$\dot{z} = V_r - \frac{K_{tread}|V_r|}{g(V_r)} z - k|\omega_w|R_r z \tag{102}$$

$$g(V_r) = \mu_c + (\mu_s - \mu_c)e^{-\left|{V_r}/{V_s}\right|^{\alpha}} \tag{103}$$

Rearranging Equation 54 and combining with Equation 56 and 53 will result in the following relationship:

$$\frac{dV_r}{dt} = -(g + a) * \mu + eK_b P_c \tag{104}$$

where, $g$ is gravity, $\mu = F_x/F_n$ is the coefficient of friction, $K_b$ is the braking torque gain, $e = R_r/J$ , and $a = (R_r^2 m_v g)/(4 * J)$. Then, combining Equation 57 into Equation 55 and rearranging to isolate the unknown parameters $K_{tread}$ and $C_{tread}$ gives,

$$\mu = K_{tread} z + C_{tread}(V_r - k|\omega_w|R_r z) - \sigma_3 f(V_r)\, z \tag{105}$$

where, $f(V_r) = |V_r|/g(V_r)$, and $\sigma_3 = K_{tread} * C_{tread}$. Recognizing that this equation can now be placed in regressor-based form, and assuming that $\mu$ can be measured [12], the following gradient-based adaptive law can be constructed:

$$\mu = [z \quad (V_r - k|\omega_w|R_r z) \quad f(V_r)\, z] * [K_{tread} \quad C_{tread} \quad \sigma_3]^T = U\Sigma \tag{106}$$

$$\tilde{\mu} = U\Sigma - \hat{U}\hat{\Sigma} = \mu - \hat{U}\hat{\Sigma} \tag{107}$$

$$\dot{\hat{\Sigma}} = -\Gamma\, \hat{U}^T \tilde{\mu} \quad \text{where, } \Gamma = \text{diag}(\gamma_0, \gamma_1, \gamma_3) > 0 \tag{108}$$

Now that an estimation of the parameters has been made, a controller can be designed to track a desired slip ratio $\lambda_m$. This desired slip ratio can be estimated based upon a pseudo-static computation of the LuGre friction model at a given velocity and assuming a uniformly distributed loading with a rectangular contact patch.

$$F_{ss} = sgn(V_r)\, F_z\, g(V_r) \left(1 + 2\gamma \frac{g(V_r)}{K_{tread}L\,|\eta|} \left(e^{-\frac{K_{tread}L\,|\eta|}{2g(V_r)}} - 1\right)\right) \tag{109}$$

$$\gamma = 1 - \frac{C_{tread}\,|V_r|}{g(V_r)} \tag{110}$$

$$\eta = \frac{V_r}{R_r \omega_w} = \frac{\lambda_w}{1 - \lambda_w} \tag{111}$$

---

[12] Note that this is a reasonable assumption as the value of $\mu$ can be obtained through measurement of the vehicle's longitudinal acceleration and knowledge of the vehicle loading.

where, $L$ is the contact patch length. Detailed derivations of these equations can be found in [18] and [50]. The desired slip ratio $\lambda_m$ can then be estimated by searching Equation 64 for its maximum,

$$\hat{\lambda}_m = \underbrace{argmax}_{\lambda_w}\left\{F_{ss}(\lambda_w\ ,\ V_r\ ,\hat{\Sigma})\right\} \tag{112}$$

A desired relative velocity error can then be developed for the controller to minimize.

$$\tilde{s} = V_r - \ \hat{\lambda}_m V = V\left(1-\hat{\lambda}_m\right) - \ R_r\omega_w \tag{113}$$

Then, taking the derivative with respect to time,

$$\dot{\tilde{s}} = \dot{V}\left(1-\hat{\lambda}_m\right) - V\frac{\partial\hat{\lambda}_m}{\partial V}\dot{V} - \ V\frac{\partial\hat{\lambda}_m}{\partial\omega_w}\dot{\omega}_w - \ a\mu\ + eK_bP_c \tag{114}$$

And then finally solving for $P_c$ gives,

$$P_c = \frac{1}{eK_b}\left[-\dot{V}\left(1-\hat{\lambda}_m\right) + V\frac{\partial\hat{\lambda}_m}{\partial V}\dot{V} + \ V\frac{\partial\hat{\lambda}_m}{\partial\omega_w}\dot{\omega}_w + \ a\mu - \ \zeta\tilde{s}\right] \tag{115}$$

where, $\dot{\tilde{s}} = \ -\zeta\tilde{s}$ and $\zeta > 0$. The partial derivatives if the desired slip ratio estimate $\hat{\lambda}_m$ are calculated numerically using the finite difference method. The stability of the controller can then be determined choosing the following Lyapunov function:

$$W = \frac{1}{2}\tilde{s}^2 \quad \Rightarrow \ \dot{W} = -\zeta\tilde{s}^2 \ \le 0 \tag{116}$$

Therefore $\tilde{s}$ is asymptotically stable. The stability of the estimators can also be analyzed by choosing the following Lyapunov candidate:

$$W = \frac{1}{2}\tilde{z}^2 + \frac{1}{2}\tilde{\Sigma}^T\Gamma^{-1}\tilde{\Sigma} \;\; \Rightarrow \;\; \dot{W} = \tilde{z}\dot{\tilde{z}} + \tilde{\Sigma}^T\Gamma^{-1}\dot{\tilde{\Sigma}} = \tilde{z}\dot{\tilde{z}} + \tilde{\Sigma}^T\Gamma^{-1}\left[-\Gamma\,\widehat{U}^T\tilde{\mu}\right] \qquad (117)$$

where $\dot{\tilde{z}}$ is calculated as follows:

$$\dot{\tilde{z}} = V_r - K_{tread}f(V_r)z - k|\omega_w|R_r z - \left[V_r - \widehat{K}_{tread}f(V_r)\hat{z} - k|\omega_w|R_r\hat{z}\right]$$

$$\xrightarrow{yields} \;\; \dot{\tilde{z}} = -(K_{tread}\,f(V_r) + k|\omega_w|R_r)\tilde{z} - f(V_r)\,\hat{z}\,\widetilde{K}_{tread} \qquad (118)$$

And noting that,

$$\tilde{\Sigma}^T\Gamma^{-1}\dot{\tilde{\Sigma}} = \tilde{\Sigma}^T\Gamma^{-1}\left[-\Gamma\,\widehat{U}^T\tilde{\mu}\right] = -\tilde{\Sigma}^T\,\widehat{U}^T\left[\widehat{U}\tilde{\Sigma} + \widetilde{U}\Sigma\right] \qquad (119)$$

Where,

$$\widetilde{U} = [1 \quad -k|\omega_w|R_r \quad -f(V_r)]\tilde{z} \qquad (120)$$

Utilizing Equations 73, 74, and 75, Equation 72 can be rewritten in quadratic form as follows:

$$\dot{W} = -[\tilde{\Sigma} \quad \tilde{z}]\begin{bmatrix} \widehat{U}^T\widehat{U} & \widehat{U}^T\widehat{U}\Sigma \\ [-f(V_r)\hat{z} \quad 0 \quad 0] & (K_{tread}\,f(V_r) + k|\omega_w|R_r) \end{bmatrix}\begin{bmatrix} \tilde{\Sigma} \\ \tilde{z} \end{bmatrix} = -\phi^T M\phi \quad (121)$$

Where, $\phi = \left[\widetilde{K}_{tread} \quad \widetilde{C}_{tread} \quad \tilde{\sigma}_3 \quad \tilde{z}\right]$, and

$$M = \begin{bmatrix} \hat{z}^2 & (V_r - k|\omega_w|R_r\hat{z})\hat{z} & -\hat{z}^2 f(V_r) & \hat{z}\omega_1 \\ (V_r - k|\omega_w|R_r\hat{z})\hat{z} & (V_r - k|\omega_w|R_r\hat{z})^2 & -(V_r - k|\omega_w|R_r\hat{z})f(V_r)\hat{z} & (V_r - k|\omega_w|R_r\hat{z})\omega_1 \\ -\hat{z}^2 f(V_r) & -(V_r - k|\omega_w|R_r\hat{z})f(V_r)\hat{z} & f^2(V_r)\hat{z}^2 & -f(V_r)\hat{z}\,\omega_1 \\ -f(V_r)\hat{z} & 0 & 0 & (K_{tread}\,f(V_r) + k|\omega_w|R_r) \end{bmatrix} \qquad (122)$$

Where, $\omega_1 = K_{tread} - k|\omega_w|R_r\,C_{tread} - f(V_r)\,\sigma_3$ . Then realizing that $M$ can be decomposed into a symmetric matrix $M_1$, and a skew-symmetric matrix $M_2$, then, $\dot{W} = -\phi^T M_1\phi - \phi^T M_2\phi$ . And noting that $-\phi^T M_2\phi = 0$ due to the properties of a skew-symmetric matrix, then, $\dot{W} = -\phi^T M_1\phi$ , where $M_1 = (M + M^T)/2$ . Therefore,

$$M = \begin{bmatrix} \hat{z}^2 & (V_r - k|\omega_w|R_r\hat{z})\hat{z} & -\hat{z}^2 f(V_r) & -\frac{1}{2}\big(\omega_1 - f(V_r)\big)\hat{z} \\ (V_r - k|\omega_w|R_r\hat{z})\hat{z} & (V_r - k|\omega_w|R_r\hat{z})^2 & -(V_r - k|\omega_w|R_r\hat{z})f(V_r)\hat{z} & \frac{1}{2}(V_r - k|\omega_w|R_r\hat{z})\omega_1 \\ -\hat{z}^2 f(V_r) & -(V_r - k|\omega_w|R_r\hat{z})f(V_r)\hat{z} & f^2(V_r)\hat{z}^2 & -\frac{1}{2}f(V_r)\hat{z}\,\omega_1 \\ -\frac{1}{2}\big(\omega_1 - f(V_r)\big)\hat{z} & \frac{1}{2}(V_r - k|\omega_w|R_r\hat{z})\omega_1 & -\frac{1}{2}f(V_r)\hat{z}\,\omega_1 & (K_{tread}\, f(V_r) + k|\omega_w|R_r) \end{bmatrix} \tag{123}$$

Since the $det[M_1(1{:}\,j, 1{:}\,j)] \geq 0$ for $j = 1,2,3, and\ 4$, then $M_1 \geq 0$. Thus,

$$\dot{W} = -\phi^T M_1 \phi \ \leq 0 \tag{124}$$

Which states that the Lyapunov function is negative semi-definite. Thus the stability of $\tilde{\Sigma} = 0$ and $\tilde{z} = 0$ is guaranteed and the errors will converge to zero given persistence of excitation.

# APPENDIX E

## STABILITY ANALYSIS FOR SLIDING MODE CONTROLLER BASED ON A TORSIONALLY FLEXIBLE TIRE

The stability analysis for the sliding mode controller proposed in Chapter 6 can be completed following a very similar procedure as used for the nonlinear controller in Chapter 5, with only a couple of minor substitutions. The stability of the closed-loop system, comprising of the parameter and state estimators and the controller tracking error, can be analyzed by choosing the following Lyapunov function candidate:

$$W = \frac{1}{2}\tilde{z}^2 + \frac{1}{2}\widetilde{\omega}_r{}^2 + \frac{1}{2}s^2 + \frac{1}{2}\tilde{\Sigma}_1{}^T \Gamma_1^{-1}\tilde{\Sigma}_1 + \frac{1}{2}\tilde{\Sigma}_2{}^T \Gamma_2^{-1}\tilde{\Sigma}_2 \ \Rightarrow$$

$$\dot{W} = \tilde{z}\dot{\tilde{z}} + \widetilde{\omega}_r\dot{\widetilde{\omega}}_r + e\dot{e} + \tilde{\Sigma}_1{}^T \Gamma_1^{-1}\dot{\tilde{\Sigma}}_1 + \tilde{\Sigma}_2{}^T \Gamma_2^{-1}\dot{\tilde{\Sigma}}_2 \tag{125}$$

$$= \tilde{z}\dot{\tilde{z}} + \widetilde{\omega}_r\dot{\widetilde{\omega}}_r + e\dot{e} - \tilde{\Sigma}_1{}^T \widehat{\mathrm{U}}_1\left[\widehat{U}_1\tilde{\Sigma}_1 + \widetilde{U}_1\Sigma_1\right]$$

$$- \tilde{\Sigma}_2{}^T \widehat{\mathrm{U}}_2\left[\widehat{U}_2\tilde{\Sigma}_2 + \widetilde{U}_2\Sigma_2\right]$$

where, $\widetilde{U}_1 = \widetilde{U}_{11}\widetilde{\omega}_r + \widetilde{U}_{12}\tilde{z}$ and $\widetilde{U}_2 = \widetilde{U}_{21}\tilde{\theta}_r + \widetilde{U}_{22}\widetilde{\omega}_r$. This leads to:

$$\widetilde{U}_{11} = [0 \quad -R_r(1 - kh'(\omega_r)\hat{z}) \quad f'(V_r)\, R_r\hat{z}]$$
$$\widetilde{U}_{12} = [1 \quad k|\omega_r|R_r \quad -f(V_r)] \tag{126}$$

$$\widetilde{U}_{21} = [1 \quad 0 \quad 0]$$
$$\widetilde{U}_{22} = [0 \quad 1 \quad 0] \tag{127}$$

where,

$$f'(V_r) = \frac{df(V_r)}{dV_r} = \frac{1}{\tilde{V}_r}\left[f(V_r) - f\left(\hat{V}_r\right)\right] = \frac{-1}{\widetilde{\omega}_r R_r}\left[f(V_r) - f\left(\hat{V}_r\right)\right] \tag{128}$$

and

$$h(\omega_r) = |\omega_\mathrm{r}| \;\Rightarrow\; h'(V_r) = \frac{dh(\omega_r)}{d\omega_r} = \frac{1}{\widetilde{\omega}_r}[h(\omega_r) - h(\widehat{\omega}_r)] \tag{129}$$

$\dot{\hat{z}}$ is computed as follows:

$$\dot{\hat{z}} = V_r - K_{tread} f(V_r)z - k|\omega_r|R_r z \tag{130}$$

$$= -\widetilde{\omega}_r A - \tilde{z}B$$

And $\dot{\tilde{\omega}}_r$ is computed as follows:

$$\begin{aligned}\dot{\tilde{\omega}}_r \; &= \frac{1}{J_r}[F_t R_r - K_t(\mathrm{\theta_r} - \; \mathrm{\theta_w}) - C_t(\mathrm{\omega_r} - \; \mathrm{\omega_w})] \\ &\quad - \frac{1}{J_r}\left[F_t R_r - \widehat{K}_t\left(\widehat{\mathrm{\theta}}_\mathrm{r} - \; \mathrm{\theta_w}\right) - \hat{C}_t(\widehat{\mathrm{\omega}}_\mathrm{r} - \; \mathrm{\omega_w})\right]\end{aligned}$$

$$\xrightarrow{yields} \quad \dot{\tilde{\omega}}_r = \frac{1}{J_r}\left[-\widetilde{K}_t(\mathrm{\theta_r} - \mathrm{\theta_w}) - \tilde{C}_t(\mathrm{\omega_r} - \mathrm{\omega_w}) - \widehat{K}_t\tilde{\mathrm{\theta}}_\mathrm{r} \right. \\ \left. - \hat{C}_t\widetilde{\mathrm{\omega}}_\mathrm{r}\right] \qquad (131)$$

Utilizing Equations (59) through (64), Equation (58) can be rewritten in quadratic form as follows:

$$\dot{W} = -[\tilde{\Sigma}_1 \quad \tilde{\Sigma}_2 \quad \tilde{z} \quad \tilde{\theta}_r \quad \widetilde{\omega}_r \;\; s][M]\begin{bmatrix}\tilde{\Sigma}_1 \\ \tilde{\Sigma}_2 \\ \tilde{z} \\ \tilde{\theta}_r \\ \widetilde{\omega}_r \\ s\end{bmatrix} = \; -\phi^T M \phi \qquad (132)$$

where, $\phi = [\tilde{\Sigma}_1 \quad \tilde{\Sigma}_2 \quad \tilde{z} \quad \tilde{\theta}_r \quad \widetilde{\omega}_r \;\; s]$, and

$$M \\ = \begin{bmatrix} \widehat{U}_1^T\widehat{U}_1 & 0 & \widehat{U}_1^T U_{12}\Sigma_1 & 0 & \widehat{U}_1^T U_{11}\Sigma_1 & 0 \\ 0 & \widehat{U}_2^T\widehat{U}_2 & 0 & \widehat{U}_2^T U_{21}\Sigma_2 & \widehat{U}_2^T U_{22}\Sigma_2 & 0 \\ 0 & 0 & B & 0 & A & 0 \\ 0 & 0 & 0 & 1 & 0 & 0 \\ 0 & C & 0 & \dfrac{\widehat{K}_T}{J_r} & \dfrac{\hat{C}_T}{J_r} & 0 \\ 0 & 0 & 0 & 0 & 0 & -\mathrm{\eta}\dfrac{\mathrm{s}}{|\mathrm{s}| + \mathrm{\delta}} \end{bmatrix} \qquad (133)$$

where,

$$\mathrm{C} = \begin{bmatrix} \frac{1}{\mathrm{J_r}}(\theta_\mathrm{r} - \theta_\mathrm{w}) & \frac{1}{\mathrm{J_r}}(\omega_\mathrm{r} - \omega_\mathrm{w}) & 0 \end{bmatrix}$$

$M$ can be decomposed into a symmetric matrix $M_1 = (M + M^T)/2$, and a skew-symmetric matrix $M_2 = (M - M^T)/2$. For a real matrix $M$, we have: $-\phi^T M_2 \phi \ = 0$ due to the properties of a skew-symmetric matrix. And it can be shown, for the matrix $M$ given by Equation (66), that the principal minors of $M_1$ are all non-negative, and therefore, $M_1$ is positive semi-definite [56]. Thus,

$$\dot{W} = -\phi^T M_1 \phi \ \leq 0 \tag{134}$$

Thus the equilibrium point $[\tilde{\Sigma}_1 \quad \tilde{\Sigma}_2 \quad \tilde{z} \quad \tilde{\theta}_r \quad \widetilde{\omega}_r \ e] = 0$ is stable and the corresponding estimation and tracking errors are bounded. Using Barbalat's Lemma it can be shown that $\lim_{t\to\infty} e = 0$. However, for guaranteed parameter and state convergence the states are required to be persistently excited.

# REFERENCES

[1] O. Emereole and M. Good, "The Effect of Tyre Dynamics on Wheel Slip Control Using Electromechanical Brakes," 2005.

[2] J. Chihoon, H. Sungho, and K. Hyunsoo, "Clamping-Force Control for Electromechanical Brake," *Vehicular Technology, IEEE Transactions on,* vol. 59, pp. 3205-3212, 2010.

[3] C. Lee and C. Manzie, "Adaptive Brake Torque Variation Compensation for an Electromechanical Brake," *SAE Int. J. Passeng. Cars - Electron. Electr. Syst.,* vol. 5, pp. 600-606, 2012.

[4] C. Lee and C. Manzie, "High-Bandwidth Clamp Force Control for an Electromechanical Brake," *SAE Int. J. Passeng. Cars - Electron. Electr. Syst.,* vol. 5, pp. 590-599, 2012.

[5] A. Watts, A. Vallance, A. Whitehead, and C. Hilton, "The Technology and Economics of In-Wheel Motors," *SAE Int. J. Passeng. Cars - Electron. Electr. Syst,* vol. 3(2), pp. 37-57, 2010-10-19 2010.

[6] D. J. Lee and Y. S. Park, "Sliding-mode-based parameter identification with application to tire pressure and tire-road friction," *International Journal of Automotive Technology,* vol. 12, pp. 571-577, 2011.

[7] N. Persson, F. Gustafsson, and M. Drevo, "Indirect Tire Pressure Monitoring Using Sensor Fusion," 2002.

[8] T. Umeno, K. Asano, H. Ohashi, M. Yonetani, T. Naitou, and T. Taguchi, "Observer based estimation of parameter variations and its application to tyre pressure diagnosis," *Control Engineering Practice,* vol. 9, pp. 639-645, 2001.

[9] P. W. A. Zegelaar, "The dynamic response of tyres to brake torque variations and road unevennesses," Dissertation, TU Delft, 1998.

[10] J. P. Pauwelussen, L. Gootjes, C. Schroder, K. U. Kohne, S. Jansen, and A. Schmeitz, "Full vehicle ABS braking using the SWIFT rigid ring tyre model," *Control Engineering Practice,* vol. 11, pp. 199-207, 2003.

[11] E. Bakker, L. Nyborg, and H. B. Pacejka, "Tyre modelling for use in vehicle dynamics studies," 1987.

[12] E. Bakker, H. Pacejka, and L. Lidner, "A New Tire Model with an Application in Vehicle Dynamics Studies," 1989.

[13] H. B. Pacejka and E. Bakker, "Magic formula tyre model," *Vehicle System Dynamics,* vol. 21, pp. 1-18, 1993.

[14] M. Burckhardt, "*Fahrwerktechnik: Radschlupfregelsysteme,*" ed. Vogel-Verlag, Germany, 1993.

[15] M. Burckhardt, "ABS und ASR, Sicherheitsrelevantes, Radschlupf-Regel System.," in *Lecture Scriptum* ed. Germany: University of Braunschweig, 1987.

[16] U. Kiencke and A. Daiss, "Estimation of Tyre Friction for Enhanced ABS-Systems," *Proceedings of the AVEC Congress in 1994,* vol. 1, pp. 15-18, 1994.

[17] C. L. Clover and J. E. Bernard, "Longitudinal tire dynamics," *Vehicle System Dynamics*, vol. 29, pp. 231-259, 1998.

[18] C. Canudas-de-Wit, P. Tsiotras, E. Velenis, M. Basset, and G. Gissinger, "Dynamic friction models for road/tire longitudinal interaction," *Vehicle System Dynamics,* vol. 39, pp. 189-226, 2003.

[19] K. Johanastrom and C. Canudas-de-Wit, "Revisiting the LuGre friction model," *IEEE Control Systems Magazine,* vol. 28, pp. 101-14, 2008.

[20] C. Canudas-de-Wit, H. Olsson, K. J. Astrom, and P. Lischinsky, "A new model for control of systems with friction," *IEEE Transactions on Automatic Control,* vol. 40, pp. 419-25, 03/ 1995.

[21] C. Canudas de Wit and P. Lischinsky, "Adaptive friction compensation with partially known dynamic friction model," *International Journal of Adaptive Control and Signal Processing,* vol. 11, pp. 65-80, 1997.

[22] L. Xu and B. Yao, "Adaptive robust control of mechanical systems with nonlinear dynamic friction compensation," Danvers, MA, USA, 2000, pp. 2595-9.

[23] L. Alvarez, J. Yi, R. Horowitz, and L. Olmos, "Dynamic friction model-based tire-road friction estimation and emergency braking control," *Transactions of the ASME. Journal of Dynamic Systems, Measurement and Control,* vol. 127, pp. 22-32, 2005.

[24] J. Yi, L. Alvarez, R. Horowitz, and C. Canudas-de-Wit, "Adaptive emergency braking control using a dynamic tire/road friction model," in *Proceedings of the 39th IEEE Conference on Decision and Control*, Piscataway, NJ, USA, 2000, pp. 456-61.

[25] L. Lu, B. Yao, Q. Wang, and Z. Chen, "Adaptive robust control of linear motors with dynamic friction compensation using modified LuGre model," *Automatica,* vol. 45, pp. 2890-2896, 2009.

[26] R. Bosch, *Bosch Automotive Handbook*: SAE, 2007.

[27] K. Z. Rangelov, "SIMULINK Model of a Quarter-Vehicle with an Anti-lock Braking System," Eindhoven University of Technology, 2004.

[28] Y. Tan and I. Kanellakopoulos, "Adaptive nonlinear friction compensation with parametric uncertainties," in *American Control Conference, 1999. Proceedings of the 1999*, 1999, pp. 2511-2515 vol.4.

[29] J. Yi, L. Alvarez, X. Claeys, and R. Horowitz, "Emergency braking control with an observer-based dynamic tire/road friction model and wheel angular velocity measurement," *Vehicle System Dynamics,* vol. 39, pp. 81-97, 2003.

[30] N. Patel, C. Edwards, and S. K. Spurgeon, "Tyre-road friction estimation - a comparative study," *Proceedings of the Institution of Mechanical Engineers, Part D (Journal of Automobile Engineering),* vol. 222, pp. 2337-51, 2008.

[31] H.-S. Tan and M. Tomizuka, "An Adaptive and Robust Vehicle Traction Controller Design," presented at the Proceedings of the 1989 American Control Conference, Pittsburgh, PA, June 1989.

[32] Y.-K. Chin, W. C. Lin, D. M. Sidlosky, D. S. Rule, and M. S. Sparschu, "Sliding-mode ABS wheel-slip control," Chicago, IL, USA, 1992, pp. 1-5.

[33] M. Schinkel and K. Hunt, "Anti-lock braking control using a sliding mode like approach," Anchorage, AK, United states, 2002, pp. 2386-2391.

[34] S. Drakunov, U. Ozguner, P. Dix, and B. Ashrafi, "ABS control using optimum search via sliding modes," *IEEE Transactions on Control Systems Technology,* vol. 3, pp. 79-85, 1995.

[35] M. Krstic and W. Hsin-Hsiung, "Design and stability analysis of extremum seeking feedback for general nonlinear systems," New York, NY, USA, 1997, pp. 1743-8.

[36] L. Kaijun, D. Kun, and X. Qunsheng, "Variable structure control for emergency braking systems using LuGre tire model," Shanghai, China, 2006, pp. 502-506.

[37] N. Patel, C. Edwards, and S. K. Spurgeon, "Optimal braking and estimation of tyre friction in automotive vehicles using sliding modes," *International Journal of Systems Science,* vol. 38, pp. 901-912, 2007.

[38] C. Unsal and P. Kachroo, "Sliding mode measurement feedback control for antilock braking systems," *Control Systems Technology, IEEE Transactions on,* vol. 7, pp. 271-281, 1999.

[39] G. A. Magallan, C. H. De Angelo, and G. O. Garcia, "Maximization of the Traction Forces in a 2WD Electric Vehicle," *IEEE Transactions on Vehicular Technology,* vol. 60, pp. 369-80, 2011.

[40] E. Kayacan, Y. Oniz, and O. Kaynak, "A grey system modeling approach for sliding-mode control of antilock braking system," *IEEE Transactions on Industrial Electronics,* vol. 56, pp. 3244-3252, 2009.

[41] W.-F. Xie and Z.-Y. Zhao, "Sliding-mode observer based adaptive control for servo actuator with friction," Harbin, China, 2007, pp. 1196-1201.

[42] B. Yao and C. Jiang, "Advanced motion control: From classical PID to nonlinear adaptive robust control," in *Advanced Motion Control, 2010 11th IEEE International Workshop on*, 2010, pp. 815-829.

[43] B. Yao, "Desired Compensation Adaptive Robust Control," *Journal of Dynamic Systems, Measurement, and Control,* vol. 131, pp. 061001-7, 2009.

[44] S. Chantranuwathana, "Adaptive robust force control for vehicle active suspensions," Ph.D. Dissertation, Mechanical Engineering: Automotive Materials, University of Michigan, 2001.

[45] S. Chantranuwathana and H. Peng, "Adaptive robust force control for vehicle active suspensions," *International Journal of Adaptive Control and Signal Processing,* vol. 18, pp. 83-102, 2004.

[46] F. Bu and H.-S. Tan, "Pneumatic brake control for precision stopping of heavy-duty vehicles," *IEEE Transactions on Control Systems Technology,* vol. 15, pp. 53-64, 2007.

[47] W. J. Palm, *System Dynamics*. New York: McGraw-Hill, 2005.

[48] M.-c. Wu and M.-c. Shih, "Simulated and experimental study of hydraulic anti-lock braking system using sliding-mode PWM control," *Mechatronics,* vol. 13, pp. 331-51, 2003.

[49] M. Hiller, "Correlation between Parameters of the Tribosystem and Automotive Disk Brake Squeal ", Universität Paderborn 2006.

[50] C. Canudas-de-Wit and P. Tsiotras, "Dynamic tire friction models for vehicle traction control," in *Proceedings of the 38th IEEE Conference on Decision and Control*, Piscataway, NJ, USA, 1999, pp. 3746-51.

[51] W. Wei-Yen, I. H. Li, C. Ming-Chang, S. Shun-Feng, and H. Shi-Boun, "Dynamic slip-ratio estimation and control of antilock braking systems using an observer-based direct adaptive fuzzy-neural controller," *IEEE Transactions on Industrial Electronics,* vol. 56, pp. 1746-56, 05/ 2009.

[52] Y. Chen and J. Wang, "Adaptive Vehicle Speed Control With Input Injections for Longitudinal Motion Independent Road Frictional Condition Estimation," *IEEE Transactions on Vehicular Technology,* vol. 60, pp. 839-48, 03/ 2011.

[53] T. J. Yeh, "Backstepping control in the physical domain," *Journal of the Franklin Institute,* vol. 338, pp. 455-479, 7// 2001.

[54] M. Krstic, I. Kanellakopoulos, and P. Kokotovic, *Nonlinear and Adaptive Control Design*: John Wiley and Sons, 1995.

[55] T.-J. Yeh, "Backstepping control in the physical domain," in *Proceedings of the 1999 American Control Conference, 2-4 June 1999,* Piscataway, NJ, USA, 1999, pp. 24-8.

[56] D. S. Bernstein, *Matrix Mathematics: Theory, Facts, And Formulas With Application To Linear Systems Theory*. Princeton, New Jersey: Princeton University Press, 2005.

[57] J.-J. E. Slotine and W. Li, *Applied Nonlinear Control*. Upper Saddle River, NJ: Prentice-Hall, Inc, 1991.

[58] H. J. Marquez and M. Riaz, "Robust state observer design with application to an industrial boiler system," *Control Engineering Practice,* vol. 13, pp. 713-728, 6// 2005.

[59] H. J. Marquez, "A frequency domain approach to state estimation," *Journal of the Franklin Institute,* vol. 340, pp. 147-157, 3// 2003.

[60] H. Ying-Jeh, K. Tzu-Chun, and C. Shin-Hung, "Adaptive Sliding-Mode Control for NonlinearSystems With Uncertain Parameters," *Systems, Man, and Cybernetics, Part B: Cybernetics, IEEE Transactions on,* vol. 38, pp. 534-539, 2008.